Plasmonic Phenomena in Multi-Dimensional Nanostructures Characterized Using Advanced Electron Microscopy

Dissertation submitted to the Department of Materials- and Geosciences at Technische Universität Darmstadt

in Fulfillment of the Requirements for the Degree of Doctor of Natural Science (Dr. rer. nat.)

by

Robin Lingstädt

born in Kirchheim/Teck, Germany

Max Planck Institute for Solid State Research

Date of Submission: July 20th, 2023

Date of Oral Examination: September 5th, 2023

Referee: Prof. Dr. Leopoldo Molina-Luna

Co-Referee: Prof. Dr. Peter A. van Aken

Darmstadt 2023

TECHNISCHE UNIVERSITÄT DARMSTADT

Robin Lingstädt: Plasmonic Phenomena in Multi-Dimensional Nanostructures Characterized Using Advanced Electron Microscopy

Darmstadt, Technische Universität Darmstadt
Publication Year of Dissertation at TUprints: 2023
URN: urn:nbn:de:tuda-tuprints-245666
URI: https://tuprints.ulb.tu-darmstadt.de/id/eprint/24566
Date of Oral Examination: September 5th, 2023

Thesis supervisors and thesis committee

Referee

Prof. Dr. Leopoldo Molina-Luna

Advanced Electron Microscopy, TU Darmstadt

Co-referee

Prof. Dr. Peter A. van Aken

Materials- and Geosciences, TU Darmstadt

Stuttgart Center for Electron Microscopy (StEM)

Max Planck Institute for Solid State Research (MPI-FKF), Stuttgart

Thesis committee

Examiner

Prof. Dr. Ralph Krupke

Molecular Nanostructures, TU Darmstadt

Examiner

Prof. Dr. Nahid Talebi

Nano-Optics

Christian-Albrechts-Universität zu Kiel

Declaration

I hereby confirm that this thesis entitled "Plasmonic Phenomena in Multi-Dimensional Nanostructures Characterized Using Advanced Electron Microscopy" has been independently carried out by me at the Stuttgart Center for Electron Microscopy (StEM), located at the Max Planck Institute (MPI) for Solide State Research ("Festkörperforschung") (FKF), fulfilling the requirements for the degree of Doctor of Natural Science (Dr. rer. nat.) in the department of Materials- and Geosciences at the Technical University of Darmstadt. I certify that the presented work is, to the best of my knowledge and belief, original and contains no material previously published or written by another person, except where due reference and permission is made.

Place and date

Signature

Plasmonic Phenomena in Multi-Dimensional Nanostructures Characterized Using Advanced Electron Microscopy

by

Robin Lingstädt

Abstract

Submitted to the Department of Materials- and Geosciences at the Technical University of Darmstadt on July 20th, 2023 in partial Fulfillment of the Requirements for the Degree of Doctor of Natural Science in Materials Science

Plasmonic phenomena have been used unknowingly of their scientific origin for more than thousand years for the production of colored glass by adding metallic salts during the melting process. Since investigations of electromagnetic properties at metal-dielectric interfaces over the last century have revealed that localized surface plasmon resonances on subwavelength-sized nanoparticles lead to optical absorption in the visible spectral range, the research field of "plasmonics" has evolved. As interconnect for light-matter interactions at the nanoscale, it has attracted significant attention due to its great potential for scientific and technological applications, such as guiding and focusing of light beyond the diffraction limit, realization of nanoantennas for optical probes in near-field imaging or surface-sensitive spectroscopic measurements.

To achieve a fundamental understanding of macroscopic phenomena, it is essential to study the underlying mechanism for individual nanoscopic objects. This has become possible through the development of advanced fabrication methods such as atomic evaporation, ion beam milling and lithography procedures,

as well as the availability of suitable characterization tools that provide the necessary spatial resolution and stability.

In this dissertation, the plasmonic properties of two-dimensional, three-dimensional and true chiral nanostructures were explored, mainly by using advanced analytical electron microscopy techniques, including electron energy-loss measurements, cathodoluminescence spectroscopy and angle-resolved polarimetry. Numerical calculations were performed to confirm the experimental findings and enhance the comprehension of the underlying physics.

Regarding the mentioned guiding capabilities, the propagation of plasmonic modes along clean and artificially structured edges of Bi_2Se_3 nanopatelets revealed the capability to cope with the presence of defects, which is highly beneficial for the realization of nanooptical circuits.

Plasmonic gold tapers enable the nanoscale concentration of electromagnetic energy. Excitation mechanisms through fast electrons were reviewed and the "phase-matching" interaction experimentally confirmed via measurements for different kinetic energies of the incident electrons.

Left- and right-handed gold nanohelices were fabricated and optically characterized to reveal their chiroptical response. Upon electron irradiation, longitudinal plamonic modes of multiple orders are excited along the helical windings. Their decay in combination with the chiral geometry leads to directional emission of circularly polarized light, that is strongly correlated both with the handedness of the investigated structure and the excitation position by the electron beam.

Charakterisierung plasmonischer Phänomene in mehrdimensionalen Nanostrukturen mit Hilfe von spezialisierter Elektronenmikroskopie

Robin Lingstädt

Zusammenfassung

Plasmonische Phänomene wurden bereits vor über 1000 Jahren ungeachtet der zu Grunde liegenden naturwissenschaftlichen Ursache genutzt, wie zum Beispiel für die Herstellung farbigen Glases durch Beimischung metallischer Salze während des Schmelzvorgangs. Erst seit der Erforschung elektromagnetischer Eigenschaften an metallisch-dielektrischen Grenzflächen im Laufe des letzten Jahrhunderts ist bekannt, dass Resonanzeffekte lokalisierter Oberflächenplasmonen an Nanopartikeln mit Abmessungen unterhalb der Wellenlänge des sichtbaren Lichts für die Farbgebung verantwortlich sind. Dieses sich entwickelnde Forschungsgebiet der "Plasmonik" stellt eine Schnittstelle dar für die Wechselwirkung von elektromagnetischer Strahlung mit Materie beziehungsweise nanoskopischen Strukturen und hat einen großen Stellenwert erlangt auf Grund vielfacher naturwissenschaftlicher oder technologischer Anwendungsmöglichkeiten. Dazu zählt die Möglichkeit, Licht unterhalb der Beugungsgrenze zu fokussieren und seine Ausbreitung zu leiten, Nanoantennen als sensitives Element im Bereich der optischen Rasternahfeldmikroskopie zu realisieren oder die Verwendung bei Oberflächen-sensitiven Spektroskopieverfahren. Für ein grundlegendes Verständnis der makroskopischen plasmonischen Phänomene ist eine Untersuchung der zu Grunde liegenden Vorgänge für individuelle Nanoobjekte unerlässlich. Dies wurde möglich durch die Entwicklung moderner Fabrikations- und Präparationsmethoden, wie beispielsweise Wachstum durch atomares Verdampfen, mechanische Bearbeitung mit fokussierten

Ionenstrahlen oder diversen Lithografieverfahren. Für die experimentelle Untersuchung bedarf es Analysemethoden, welche über die benötigte hohe örtliche Auflösung und Stabilität verfügen.

In dieser Dissertation wurden zweidimensionale, dreidimensionale und chirale Nanostrukturen hinsichtlich ihrer plasmonischen Eigenschaften untersucht, hauptsächlich durch die Verwendung analytischer Techniken der Elektronenmikroskopie, wie Elektronenenergieverlustspektroskopie und Kathodolumineszenzspektroskopie und -polarimetrie. Numerische Simulationen wurden durchgeführt, um die experimentellen Messungen zu validieren und ein tieferes Verständnis der zu Grunde liegenden Physik zu ermöglichen.

Die Ausbreitung plasmonischer Moden entlang künstlich strukturierter Kanten von Bi_2Se_3 Nanoplättchen zeigte ein hohes Maß an Resistenz gegenüber diesen Defekten, was für die Realisierung von nano-optischen Schaltkreisen sehr vorteilhaft ist.

Feine Goldspitzen ermöglichen die Fokussierung von elektromagnetischer Energie auf der Nanoebene. Die Wechselwirkung mit relativistischen Elektronen wurde erläutert und ein experimenteller Nachweis für den Mechanismus der "Phasen-Überlagerung" präsentiert.

Die elektronenoptische Anregung einzelner chiraler Gold-Helices initiierte plasmonischen Resonanzen entlang der Windungen, deren Dämpfung zur Abstrahlung von gerichtetem zirkular polarisiertem Licht führte. Die Richtung der zirkularen Polarisation hing dabei sowohl von der untersuchten Struktur als auch von der Anregungsposition durch den Elektronenstrahl ab.

Acknowledgments

From the bottom of my heart and seoul, I would like to express my sincere gratitude to all people who knowingly or unknowingly, directly or indirectly contributed to the completion of this work.

Scientific supervisors and collaborators I would like to thank all professors of the examination board (*Leopoldo Molina-Luna*, *Ralph Krupke*) and in particular *Nahid Talebi*, as my PhD-supervisor for her help and important contributions to our projects and publications, and *Peter van Aken* as the "research-captain" of our group for his support throughout my PhD-time, professional scientific coaching and the possibilities to attend national and international conferences and workshops. Furthermore, I appreciate the fruitful discussions with *Wilfried Sigle*, which are preferably held on a picturable level. I would like to thank *Masoud Taleb* for his support during the CL measurements in Kiel and inspiration to start 3D-rendering in Blender, *Fatemeh Davoodi* and *Kenan Elibol* for their simulations regarding nanohelices and especially *Kenan* for the productive and pleasant collaboration during this project.

StEM-group In the naval picture, as utilized already before, every crew needs a professional first officer. Far beyond dealing with administrative matters,

Carolin/e Heer really takes care of the group like a mother, which is the best compliment I can think of as a family father. To "keep electrons running", skilled technical staff is essential, both regarding sample preparation and microscope operation/maintenance. In particular, I would like to thank *Marion Kelsch* for my first-ever TEM-session, motivating conversations and being the biggest fan of my home-made carrot cake, *Birgit Bussmann* for teaching me how to perform ultramicrotomy cutting, *Ute Salzberger* for sample preparation and IT support, *Peter Kopold* for the introduction to ARM-operation and a nice office-sharing experience and *Kersten Hahn* for taking care of SESAM. PhD-students and Post-Docs, who join as "passengers" for a limited time, and also permanent researchers certainly contribute to the good working atmosphere as well and I really enjoyed meeting so many nice people with different national and social backgrounds in an open-minded international environment. Sharing moments and memories with all former and current colleagues, either at Ringberg Castle, other workshops and conferences, works outings or cake-events in "our" coffee-corner, I would like to thank in particular *Ekin Simsek Sanli*, *Umut Tunca Sanli* and *Nilesh Vats* for their friendship that has developed over the years, resulting in tasty "Dinnertimes".

Institute collaborations Including the preceding Master studies, I have spent a reasonable fraction of my academic career at the Max Planck campus in Stuttgart-Büsnau, which is a wonderful place to work, both scientifically and socially. I gratefully remember to have met, talked to or collaborated with so many nice people from different institute-facilities, such as the *supply store*, *glas workshop*, *mechanical workshops*, *IT-Helpdesk*, *administration*, *medical office*, *cleanroom* and *graphical office*. I wish my colleagues of the parametics-team no serious cases of medical emergencies.

Physics collective including terms of higher order "Remember the faces of your neighbors, because only one of you will finish his Master in physics!" This empirical truth, proclaimed during the first lecture, was disproved by our study-group. We all made it and I am so grateful to have met *Trish*, *Missa*, *Nico* and *Joni*. Going through challenging times together, we also accumulated valuable memories during study breaks, excursions, adventurous hiking trips and legendary birthday or wedding parties with very creative greeting cards.

Family I cincerely thank my brother *Timo* and my parents *Gaby* and *Udo Lingstädt*, in whom I see the origin of everything that I achieved and the person that I have become. With much love and trust, but no pressure, we were always encouraged and supported to develop our skills, believe in ourselves and accomplish our goals.

Children "One should never forget how to see the world through children's eyes." (free translation after Henri Matisse) We experience the wonder of life through our children *Cataleya* (6 years), *Ayana* (3 years) and *Luan Andres* (3 months) in different development stages, ranging from the fascination for small things to asking questions about how the world works, which we try to answer in an appropriate but correct way to keep the natural flame of scientific interest burning.

My Wife deserves the very last on the list, but (like in papers) one of the most important positions in my life. *Alexandra*, my Portuguese flame, shines at my side since 2011 and illuminates my way with love, support and encouragement when needed. Besides managing household-related work, as a super-mother, she also takes care of our children, the three most important publications of my life.

Academic biography

Education

Ph.D.	**Materials Science**	2017 – 2023
	Max Planck Institute for Solid State Research	
	Technical University of Darmstadt	supervised by:
		Prof. Dr. Leopoldo Molina-Luna
		Prof. Dr. Peter A. van Aken
M.Sc.	**Physics**	2014 – 2016
	Max Planck Institute for Solid State Research	
	University of Stuttgart	Thesis supervised by:
		Prof. Dr. Jörg Wrachtrup
		Prof. Dr. Peter A. van Aken
B.Sc.	**Physics**	2010 – 2014
	University of Stuttgart	
		Thesis supervised by:
		Prof. Dr. Martin Dressel

Publications

(A) Robin Lingstädt, Nahid Talebi, Surong Guo, Wilfried Sigle, Alfredo Campos, Mathieu Kociak, Martin Esmann, Simon F. Becker, Eiji Okunishi, Masaki Mukai, Christoph Lienau, Peter A. van Aken, "Probing plasmonic excitation mechanisms and far-field radiation of single-crystalline gold tapers with electrons", *Phil. Trans. R. Soc. A* **378**, 20190599 (2020).[1]

(B) Robin Lingstädt, Nahid Talebi, Mario Hentschel, Soudabeh Mashhadi, Bruno Gompf, Marko Burghard, Harald Giessen, Peter A. van Aken, "Interaction of edge exciton polaritons with engineered defects in the hyperbolic material Bi_2Se_3", *Commun. Mater.* **2**, 5 (2021).[2]

(C) Michael Geiger, Robin Lingstädt, Tobias Wollandt, Julia Deuschle, Ute Zschieschang, Florian Letzkus, Joachim N. Burghartz, Peter A. van Aken, Thomas Weitz, Hagen Klauk, "Subthreshold Swing of 59 mV decade^{-1} in Nanoscale Flexible Ultralow-Voltage Organic Transistors", *Adv. Electron. Mater.* **8**, 5, 2101215 (2022).[3]

(D) Robin Lingstädt, Fatemeh Davoodi, Kenan Elibol, Masoud Taleb, Hyunah Kwon, Peer Fischer, Nahid Talebi, Peter A. van Aken, "Electron Beam Induced Circularly Polarized Light Emission of Chiral Gold Nanohelices", *ACS Nano (under review)* (2023)

Publications (A), (B) and (D) are implemented and discussed in this dissertation.

Conference contributions

(a) Nahid Talebi, Mario Hentschel, Harald Giessen, Robin Lingstädt, "Hyperbolic and dirac plasmons in topological Insulators", (presentation) *SPIE Photonics Europe*, Strasbourg, France (2018)

(b) Robin Lingstädt, Mario Hentschel, Soudabeh Mashhadi, Marko Burghard, Peter A. van Aken, Harald Giessen, Nahid Talebi, "Interaction of hyperbolic wedge polaritons with structured defects in Bi_2Se_3", (poster) *JEELS conference*, Porquerolles Island, France (2018)

(c) Robin Lingstädt, Mario Hentschel, Soudabeh Mashhadi, Marko Burghard, Peter A. van Aken, Harald Giessen, Nahid Talebi, "EELS investigations of Bi_2Se_3 – Surface plasmons in topological insulators", (presentation and poster) *International Ringberg-Castle workshop*, Tegernsee, Germany (2018)

(d) Robin Lingstädt, Mario Hentschel, Soudabeh Mashhadi, Marko Burghard, Peter A. van Aken, Harald Giessen, Nahid Talebi, "Interaction of hyperbolic wedge polaritons with structured defects in Bi_2Se_3", (poster) *SuperSTEM summer school (advanced topics in C_S-corrected STEM & Spectroscopy)*, Manchester, UK (2018)

(e) Robin Lingstädt, Nahid Talebi, Mario Hentschel, Soudabeh Mashhadi, Marko Burghard, Harald Giessen, Peter A. van Aken, "Wedge polaritons interacting with engineered defects in the hyperbolic material Bi_2Se_3", (presentation) *AMOLF International Nanophotonics Summerschool*, Amsterdam, the Netherlands (2019)

(f) Robin Lingstädt, Birgit Bussmann, Ute Salzberger, Soudabeh Mashhadi, Nahid Talebi, Peter A. van Aken, “Permittivity determination of the hyperbolic material Bi_2Se_3 by low-loss EELS”, (presentation) *International Ringberg-Castle workshop*, Tegernsee, Germany (2019)

(g) Robin Lingstädt, Nahid Talebi, Mario Hentschel, Soudabeh Mashhadi, Marko Burghard, Harald Giessen, Peter A. van Aken, “Propagating Wedge Polaritons Interacting With Patterned Defect Structures in Bi_2Se_3 Nanoplatelets”, (poster) *Microscopy Conference*, Berlin, Germany (2019)

(h) Masoud Taleb, Robin Lingstädt, Mario Hentschel, Soudabeh Mashhadi, Marko Burghard, Harald Giessen, Peter A. van Aken, Nahid Talebi, "Strong Exciton-Photon Interactions in the van der Waals Materials Probed by Electron Beams", (abstract) *CLEO: Conference on Lasers and Electro-Optics*, San Jose, California, USA (2021)

(i) Robin Lingstädt, Fatemeh Davoodi, Kenan Elibol, Masoud Taleb, Hyunah Kwon, Peer Fischer, Nahid Talebi, Peter A. van Aken, “Near- and Far-field characterization of 3D-nanoparticles by EELS and CL”, (poster) *eBEAM - nano-optics with free electrons*, Porquerolles Island, France (2022)

Contents

Acronyms

2D two-dimensional

3D three-dimensional

AFM atomic force microscope

BCML block copolymer micellar nanolithgraphy

BEM boundary element method

BF bright-field

BFP back focal plane

BSE backscattered electron

CCD charge-coupled device

CD circular dichroism

CL cathodoluminescence

CMOS complementary metal oxide semiconductor

CPL circularly polarized light

DF dark-field

DM Digital Micrograph

DNA deoxyribonucleic acid

EDX energy-dispersive X-ray

EELS electron energy-loss spectroscopy

EFTEM energy-filtered transmission electron microscopy

ELNES energy-loss near-edge structure

EMLDOS electromagnetic local density of states

ET electron tomography

EXELFS extended energy-loss fine-structure

FDFD finite-difference frequency-domain

FDTD finite-difference time-domain

FEG field emission gun

FIB focused ion beam

FKF Solide State Research ("Festkörperforschung")

FWHM full width at half maximum

GLAD glancing-angle deposition

h-BN hexagonal boron nitride

HAADF high-angle annular dark-field

HCl hydrochloric acid

HEEP hyperbolic edge exciton polariton

JFCC Japan Fine Ceramics Center

LCP left circularly polarized

LDOS local density of states

LP linearly polarized

LSPR localized surface plasmon resonance

MCR monochromator

MFP mean free path

MPI Max Planck Institute

NA numerical aperture

OA objective aperture

OR optical rotation

ORD optical rotatory dispersion

PCA principle component analysis

PVD physical vapour deposition

QL quintuple layer

QWP quarter wave plate

RCP right circularly polarized

ROI region of interest

SAD selected-area diffraction

SE secondary electron

SEM scanning electron microscope

SESAM sub-electronvolt sub-angstrom microscope

SI spectrum image

SIRT simultaneous iterative reconstruction technique

SNOM scanning near-field optical microscopy

SNR signal-to-noise ratio

SP surface plasmon

SPP surface plasmon polariton

SPR surface plasmon resonance

STEM scanning transmission electron microscopy

StEM Stuttgart Center for Electron Microscopy

STM scanning tunneling microscope

TE transverse electric

TEM transmission electron microscope

TM transverse magnetic

UV ultraviolet

vdW van der Waals

WBP weighted back projection

ZLP zero-loss peak

List of Figures

1 Introduction

This chapter is dedicated to introduce the research field of plasmonics and suitable nanoscopic characterization tools. After introducing the fundamental principles of plasmonic excitations, their scientific investigation via analytical electron microscopy techniques is motivated. This includes a discussion of the technical setup and different imaging modes in an electron microscope, followed by the introduction of key analytical capabilities: electron energy-loss spectroscopy (EELS) and the study of emitted cathodoluminescence (CL) radiation. These two techniques were mainly used in this work. After a theoretical description of fast moving electrons and their interaction with excited plasmons, an outline of the dissertation is provided.

1.1 Motivation

Optical phenomena that are related to light-matter interactions are part of everyday life and have been used also technologically for more than thousand years. The fabrication process of colored glass is a suitable example in this regard. However, underlying physical principles could only be explained through scientific investigations of optical and electronic material properties.

The research field of plasmonics in particular deals with the generation, detection and manipulation of signals at metal-dielectric interfaces on nanoscopic scales.[4] It has also attracted significant attention, owing to the general trend towards miniaturization. The macroscopic response of a sample may be influenced by processes that occur on a length scale far below the diffraction limit and are therefore unaccessible by traditional light-based spectroscopic techniques. Besides being one of the pioneering methods to unravel the existence of plasmon oscillations at metal surfaces,[5–11] electron microscopy allows for a spatial resolution down to the atomic level due to ultra-short equivalent deBroglie-wavelengths.[12] The ability to map localized surface plasmon resonances (LSPRs) for individual nanoparticles was achieved in the year 2007 via energy-loss measurements.[13–15] As spatial and energy-resolution have been improved since then, EELS is still one of the best methods to map plasmon resonances of metallic nanostructures.[16–18]

1.2 Plasmonic excitations

For an intuitive explanation, a neutral metal can be considered as a three-dimensional (3D) arrangement of positively charged atomic nuclei, that are surrounded by a reservoir of delocalized negatively charged electrons. Unlike for phonons, which describe lattice vibrations, the comparably heavy atomic cores are assumed to be stationary. When electrons are locally displaced, the field of electric dipoles induces a restoring force that results in a collective oscillation. The term *plasmon* refers to its quantized energy E_P (similar to a photon for electromagnetic radiation) and is defined via the plasma-frequency

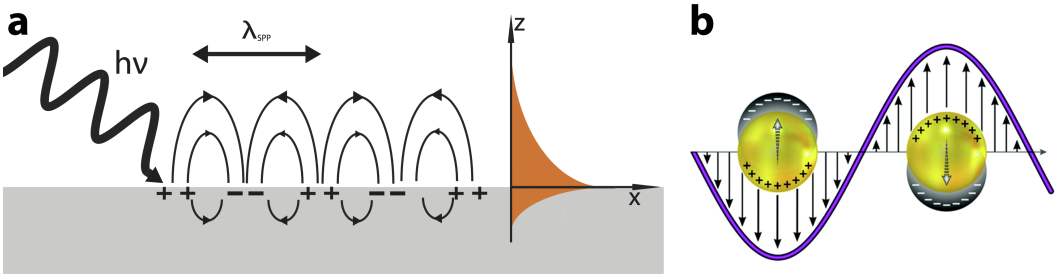

Fig. 1.1: (a) SPPs can be excited at a metal-dielectric interface. Longitudinal charge oscillations occur along the propagation direction with an evanescent electric field in the out-of-plane direction. (b) LSPRs are excited for small nanoparticles by an applied electric field. Figures (a) and (b) are adapted from Wikipedia (public domain) and the original publication, respectively.[19]

ω_P, that depends on the free-electron density n, following

$$E_P = \hbar\omega_P = \hbar\sqrt{\frac{ne^2}{\epsilon_0 m}}, \tag{1.1}$$

where $\hbar$ is the reduced Planck constant, ϵ_0 the vacuum permittivity, e the elementary charge and m the electron mass. Besides these bulk plasmons, charge oscillations can be confined to only two dimensions, for example by considering a metal-dielectric interface. Such surface plasmon polaritons (SPPs) can couple to external electric fields and propagate evanescently bound to the interface with a decaying electric field in the perpendicular direction (figure 1.1 a). For particle sizes with similar or smaller dimensions than the SPP wavelength, LSPRs occur in the form of local charge displacements (figure 1.1 b) that strongly depend on the sample size and geometry and its dielectric environment.[20] Secondary effects include an enhancement of electric fields near the surface and optical absorption at the resonance energy. Specifically in the case of gold nanoparticles, this resonance energy falls within the visible spectral range, contributing to the vibrant colors observed in stained glass, such as those commonly found in church

windows. Analytically, the excitation of SPPs is used for surface plasmon resonance (SPR) measurements and experimentally realized via a glass prism either in the Otto[21] or Kretschmann-configuration[22], which both generate an evanescent wave through total reflection to fulfill the momentum-conservation criterion. Another possibility to generate the necessary in-plane momentum can be achieved by coupling light to a grating with a suitable reciprocal lattice vector. In addition to these conventional techniques using electromagnetic radiation, plasmons can be efficiently excited by fast electrons due to their inherent momentum. In addition, the excitation can occur locally and studied with a high spatial resolution, as provided by electron microscopy.

1.3 Electron microscopy

The achievable resolution of optical microscopes has been continuously improved and transformed the first simple instruments of the 16^{th} century into complex optical systems. However, the maximum resolution for conventional microscopy is theoretically limited, as described by Ernst Abbe for a condensor-based illumination with the formula

$$d_{\min} = \frac{\lambda}{2 \cdot n \cdot \sin(\alpha)}, \tag{1.2}$$

where the smallest detectable separation $d_{\min}$ of two features is calculated by the wavelength λ and the numerical aperture (NA) with $NA = n \cdot \sin(\alpha)$ of the optical system. Here, n is the refractive index of the immersive medium and α the semi-collection angle of the objective lens. When operated in air with $n = 1$, features as small as half of the wavelength could be in principle resolved. With visible light, this is in the range of several hundred nanometers.

According to formula 1.2, the resolution limit is improved by either increasing the refractive index n or using a shorter wavelength λ. The former is achieved for example by oil immersion microscopy, where a transparent medium is used between the sample and the objective lens, which is in turn accompanied by shortcomings in terms of sample preparation and ease of use. On the other hand, instruments using ultraviolet (UV) light were developed in the early 20^{th} century and could push the resolution limit even further. However, direct observation by the human eye was not possible anymore and because of other experimental disadvantages, this technique did not prevail.

In electron microscopy, a totally different technique is used to dramatically decrease the wavelength. Its functionality is based on the physical principle, known as the wave-particle duality, according to which fast moving particles can be described as a wave. For electrons, this effect was postulated by Louis de Broglie in his PhD thesis in the year 1924.[23] He described the correlated wavelength λ_{dB} by the formula

$$\lambda_{\text{dB}} = \frac{h}{p}, \tag{1.3}$$

where h is the Planck constant and p the mechanical momentum of the moving particle. For his discovery, he was awarded the Nobel prize for physics in the year 1929 after its experimental prove.[24] Although the raypath of a conventional electron microscope is in principle similar to optical systems, the use of accelerated particles instead of electromagnetic waves implies different requirements and techniques ranging from the electron source, deflective optics, imaging systems and an entirely evacuated beampath. The first transmission electron microscope (TEM) was built by Ernst Ruska (Nobel prize for physics in the year 1986) and his colleague Max Knoll in the early 1930s.[25] The

instrument outperformed optical light microscopes of their time in terms of magnification and the potential to reach atomic resolution with this new technique was discussed. For an assumed acceleration voltage of 200 kV the electrons reach a velocity of approximately

$$v = c\sqrt{1 - \frac{1}{(1 + \frac{E_{\mathrm{kin}}}{m_e c^2})^2}} \approx 2.08 \times 10^8 \,\mathrm{m\,s^{-1}},$$

where c is the speed of light, m_e the electron rest mass and $E_{\mathrm{kin}} = 200\,\mathrm{keV}$ the kinetic energy. For this high speed of $v \approx 0.7\,\mathrm{c}$, the momentum in equation (1.3) as well has to be considered relativistically as

$$p_{\mathrm{rel}} = \frac{m_e v}{\sqrt{1 - (\frac{v}{c})^2}}.$$

The resulting de Broglie wavelength is in the range of a few picometers and can reach values even below 1 pm for dedicated ultra-high voltage electron microscopes as shown in figure 1.2 b. However, atomic resolution is not as easily achievable as implied by these calculations. The major limiting factor is the quality of round magnetic lenses, that are used to deflect the electrons and form a beam path. Otto Scherzer identified geometrical aberrations, that reduce the image quality as electrons with different trajectories are not focussed in the same focal plane. He realized that the unavoidable and most relevant spherical aberration (i.e. electrons further away from the optical axis are deflected more strongly) is a practicle but not fundamental limitation.[26] His experiments with compensating elements marked the beginning of aberration-corrected electron microscopy.[27] This idea was continued by his student Harald Rose[28] and finally realized in the year 1998.[29,30] Even though atomic resolution below 1 Å had been demonstrated shortly before with an uncorrected 1.25 MeV instrument (its accelerator is shown in figure 1.2 c),[12] modern corrected machines do not

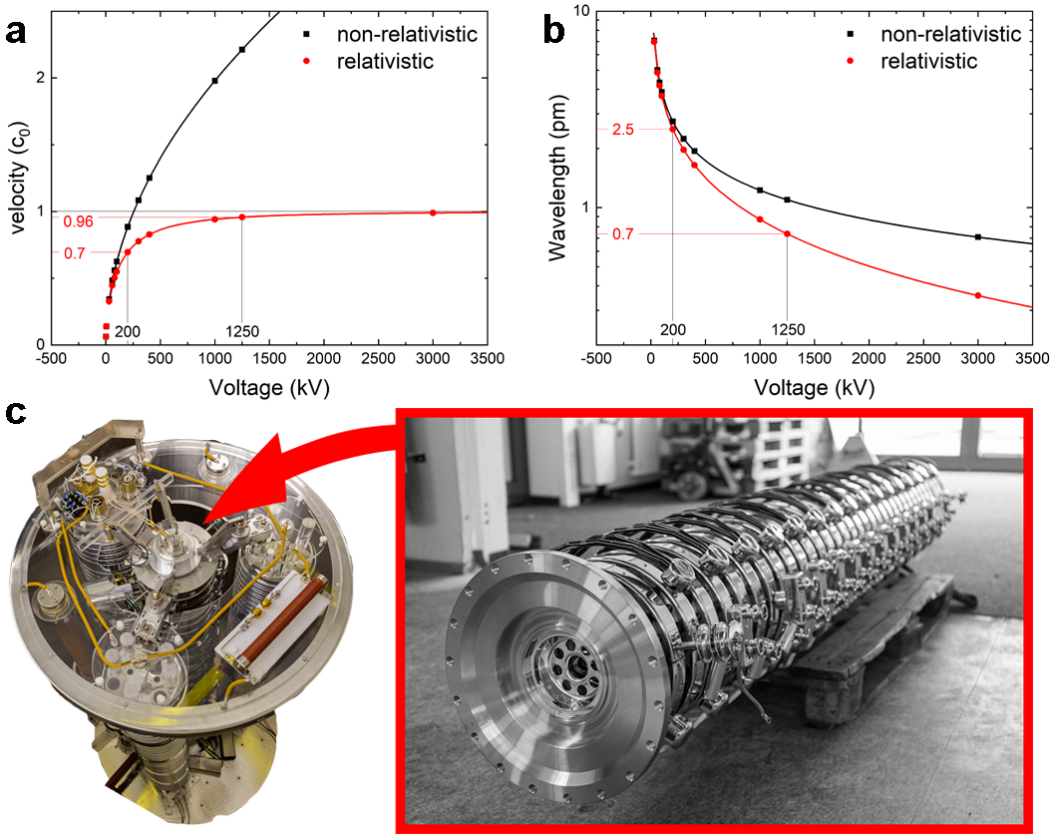

Fig. 1.2: Relativistic effects on velocity (a) and correlated de Broglie wavelength (b) of an electron in dependence of the acceleration voltage. (c) The accelerator of the *JEOL JEM-ARM1250* electron microscope provided a voltage of 1.25 MeV.

require ultra-high acceleration voltages above 1 MV to reach the required resolution.

The implemented technology and consequently performence has improved over time. However, the basic principle and constructional parts of modern machines are still the same. In close similarity to light microscopes, a TEM consists of five main components, namely the electron source, the illumination system, the imaging system, followed by the magnifying part and terminated by means for visualization.

A beam of electrons is provided by the electron gun, where they are extracted from a sharp cathode electrode and accelerated by high electric fields. Depending on the filament design, the extraction occurs either thermally or via tunneling out of the material. The subsequent condenser system shapes the beam to either provide an almost parallel illumination of various sizes and intensities in the (conventional) TEM mode or to form a convergent electron probe for scanning transmission electron microscopy (STEM), as it will be explained later. The electron-transparent sample is positioned between the pole pieces of the objective lens and is precisely adjustable in all directions. Two operational modes are possible for the imaging system and are shown in figure 1.3. The objective lens deflects parallel rays to a crossover in the back focal plane (BFP) and forms an image of the specimen. An adjustable intermediate lens is used to either project the image plane or the BFP to the subsequent cascade of magnifying lenses and therefore determines, whether the microscope is operated in imaging mode or in diffraction mode. The latter is especially useful for the investigation of crystalline samples, where the periodic arrangement of atoms results in a diffraction pattern. Considering the electron beam as a wave, constructive interference, following Braggs law, leads to this arrangement of spots with high intensities that in turn contains information

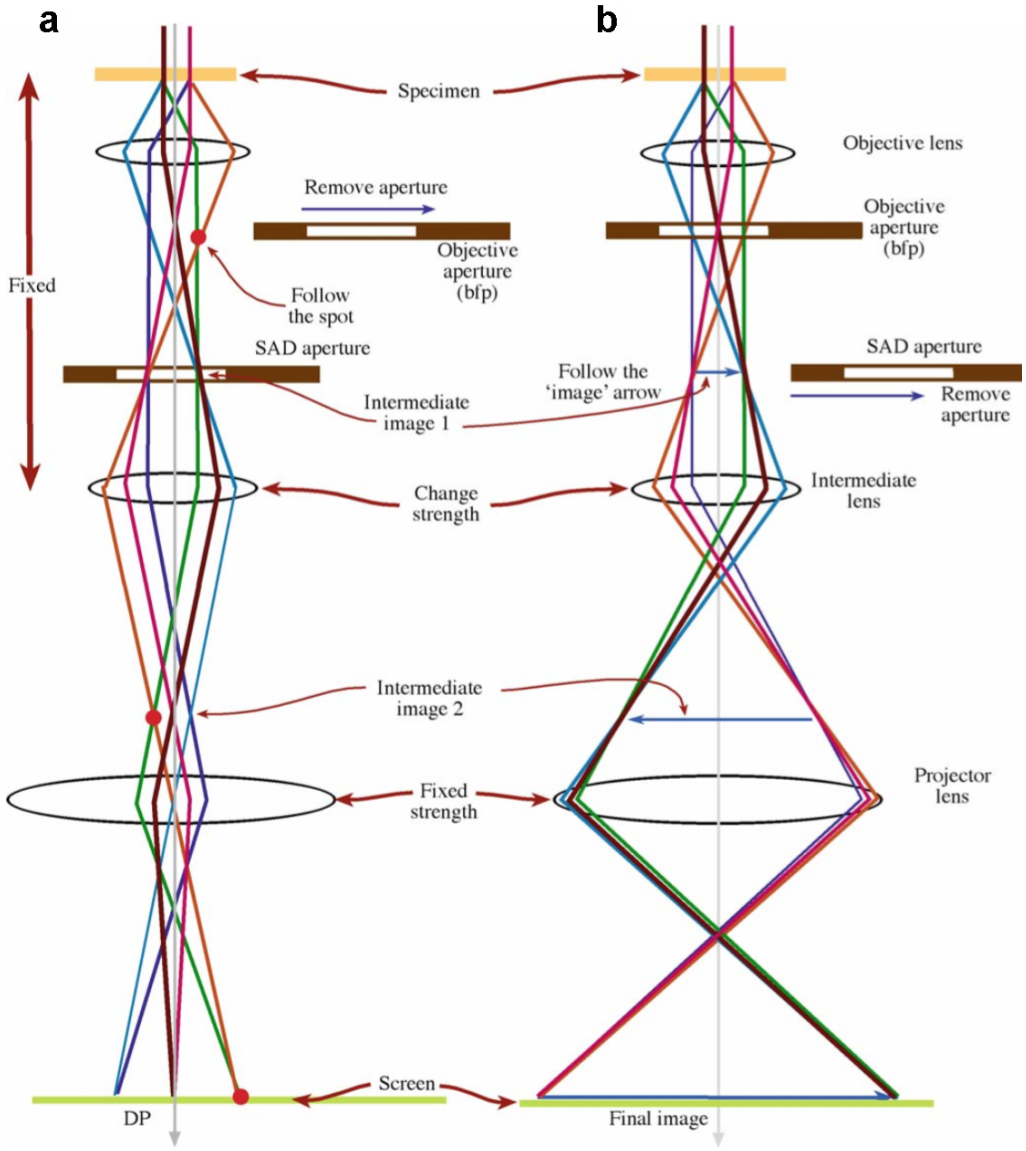

Fig. 1.3: In the TEM image forming system, the intermediate lens projects either the BFP (a) or the image plane (b) of the objective lens to the magnifying system and hence switches between diffraction and image mode, respectively. In the former, a selected-area diffraction (SAD) aperture can be used to artificially mask the region of interest (ROI) that contributes to the signal. In the latter, an objective aperture (OA) selects axial rays and hence increases the contrast. Image adapted from a textbook. [31]

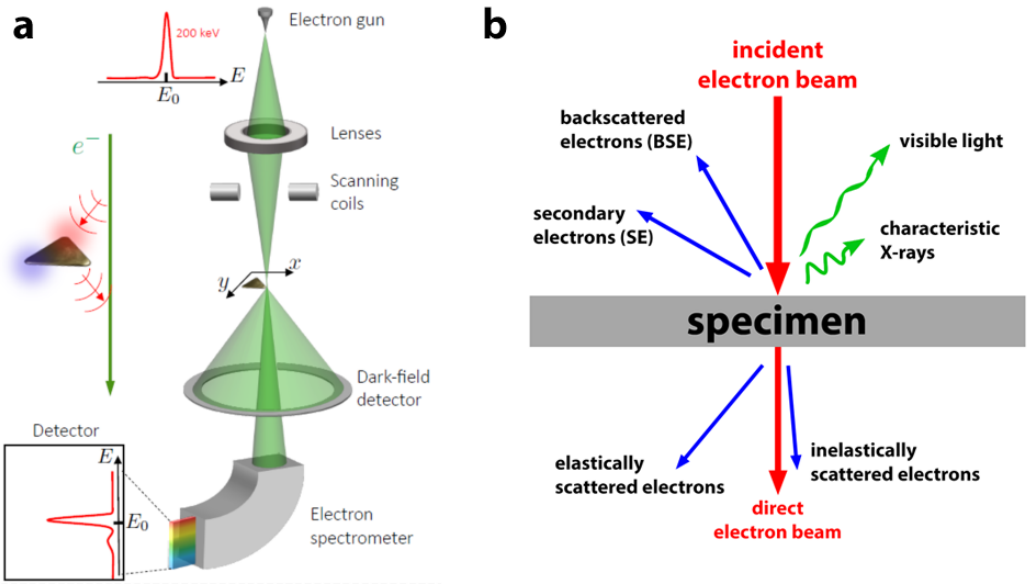

Fig. 1.4: (a) Images in a STEM are generated by correlating the dark-field signal of elastically scattered electrons with the electron beam position. Through inelastic interactions with the specimen, some electrons lose energy, which can be spectroscopically analyzed. Graphic adapted from Hugo Lourenco Martins (b) Upon electron irradiation, both elastic and inelastic interactions with the specimen generate signals, that can be used for imaging and analytical measurements.

about the underlying crystal structure. Irrespective of the operation mode, electrons are visualized through a fluorescent screen for visual observation, a scintillator in front of a charge-coupled device (CCD) or complementary metal oxide semiconductor (CMOS) camera and recently also via direct electron detectors.

As mentioned before, a different approach in electron microscopical imaging utilizes a convergent beam that is raster-scanned over the sample (figure 1.4 a). In contrast to conventional imaging, the resolution is determined by the quality of the focused electron probe and can nowadays reach spot sizes below 1 Å in modern STEMs and hence atomic resolution. Spatial contrast is generated by

correlating the intensity of elastically scattered electrons with the electron beam position. For high-angle annular dark-field (HAADF) imaging, the detected signal is based on incoherent Rutherford scattering at the atomic nuclei of the investigated material with the atomic number Z. Because of its proportionality to roughly Z^2 it is termed "Z-contrast imaging".[32] Inelastic interactions with the specimen (as sketched on the left side in figure 1.4 a) lead to an energy-loss of the incident electrons, which can be spectroscopically analysed in an energy-dispersive detection system (as introduced in section 1.3.1). Other primary and secondary signals, including emitted electromagnetic radiation, are generated upon electron irradiation and can be used either for imaging or analytical purposes (figure 1.4 b). While characteristic X-rays allow for elemental mapping via energy-dispersive X-ray (EDX) measurements, light emitted in the visible spectral range is analysed in the scope of CL investigations. Secondary electrons (SEs) and backscattered electrons (BSEs) are both emitted from surface regions and do not require an electron-transparent specimen. They are used in scanning electron microscopes (SEMs) for topographic imaging. BSEs originate from a deeper interaction volume and provide additional Z-contrast.

1.3.1 Electron energy-loss spectroscopy (EELS)

Although the technique was already developed in 1944,[33] its popularity started to increase in the 1990s with the technical improvement of electron microscopes. Until today, EELS has become a widely used and highly capable analytical tool for scientific investigations in materials sciences. Electrons that interact inelastically with the specimen lose a small amount of their initial energy and are detected in an energy-dispersive spectrum (figure 1.5). The measured energy-loss is related to the scattering event and can be assigned to

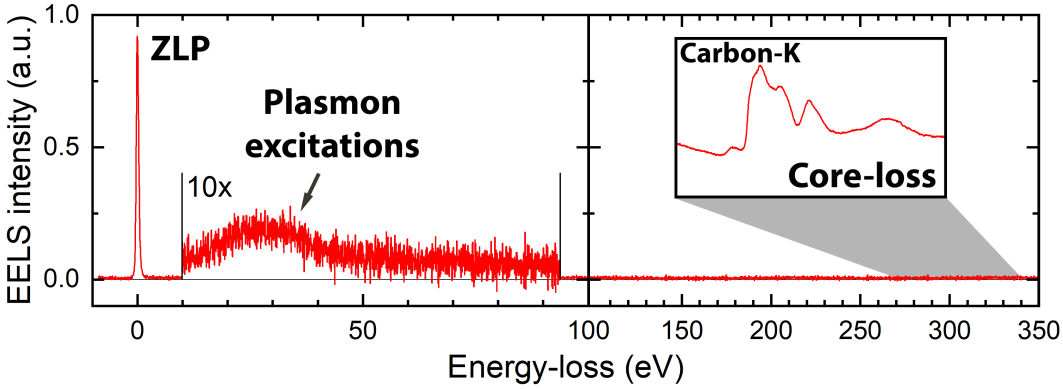

Fig. 1.5: The energy-loss spectrum can be devided into the low-loss regime (<50 eV) which contains the very intense ZLP and plasmonic excitations and the core-loss region with element-specific ionization-edges and additional spectroscopic information. The experimental data shown was acquired on a diamond nanoparticle.

corresponding energy ranges. Energy-loss spectra can be phenomenologically devided into three parts, namely the zero-loss peak (ZLP), the low-loss and core-loss regions.

The ZLP contains most of the incident electrons and consequently exhibits an intensity that is orders of magnitude higher than the rest of the spectrum. Its full width at half maximum (FWHM) also influences the achievable energy-resolution, which can be increased by using a monochromator (MCR).

The low-loss regime covers energies up to 50 eV, including plasmonic excitations of outer-shell electrons, and contains information about excitons, inter- and intra-band transitions, bandgaps and phonons.[34–36] Practically, low-loss spectra can be used to determine the thickness t of a specimen via the log-ratio technique according to

$$\frac{t}{\lambda_{\mathrm{MFP}}} = \ln\left(\frac{I}{I_0}\right), \tag{1.4}$$

where λ_{MFP} is the inelastic mean free path (MFP) of a material and I_0 and I

denote the integrated intensity of the ZLP and the complete spectrum.[37]

Energy-losses higher than 50 eV are part of the core-loss regime. As implied by the name, it contains information about element-specific ionization energies that are required to remove inner-shell electrons from the atoms and hence can be utilized for elemental mapping, nowadays at the atomic level. These energies appear as edges in the spectrum with subsequent energy-loss near-edge structure (ELNES) and extended energy-loss fine-structure (EXELFS). Their spectral features allow for further characterization regarding chemical, physical and structural properties.

1.3.2 Cathodoluminescence (CL)

CL describes the optical phenomenon that electromagnetic radiation is emitted by a luminescent material upon electron irradiation. Therefore, it is the inverse to the photoelectric effect, which was first discovered by Heinrich Hertz in the year 1887[38] and later theoretically described by Albert Einstein (Nobel prize in physics 1921).[39] The name originates from cathode ray tubes that were technically used to realize the first monitors via raster-scanning accelerated electrons over a phosphor screen. Meanwhile, technologies for CL detection have been implemented in electron microscopes, enabling the local excitation of specimens with high spatial resolution, while analyzing the emitted light spectroscopically, directionally or regarding its polarimetric properties. While EELS probes the primary excitation of a specimen, luminescence results from a subsequent relaxation process, for example, when an excited electron of the conduction band recombines with a hole in the valence band in a semiconductor.[40–42] The difference in energy is emitted in the form of electromagnetic radiation at the corresponding wavelength. Especially the combined study

of an object by EELS and CL gives complementary insight into its physical properties.[43–47] However, it is important to note that only the radiative decay of excitations contributes to the measured far-field signal. In the scope of plasmonic excitations, these "bright modes" are detectable in the CL measurements,[48,49] while "dark modes" can only be probed via their excitation signature in EELS.[50–53]

1.4 Plasmons excited by fast electrons

Beam electrons inside a TEM are considered to propagate along a straight trajectory with constant velocity. The electric field accompanying these fast moving point charges in vacuum decays exponentially away from the trajectory and does not radiate to the far-field. For an imaginary observer, the passing electron appears as an ultra-short pulse on the time scale of only a few femtoseconds. In return, its broadband spectral characteristic allows for excitations in the energy range from meV to keV.[54] As the electric field strength of the electron's evanescent field in radial direction decays more slowly for lower frequencies, low-loss excitations occur more delocalized. In the case of SPPs or LSPRs, the interaction with the plasmonic specimen happens via long-range Coulomb fields and can be achieved even without penetrating the material in an aloof configuration. During the excitation process, the induced local polarization causes a scattered electromagnetic field, which acts back on the electron. The accumulated energy-loss, as experienced by the incident electron, is directly related to the photonic local density of states (LDOS) projected along the electron trajectory[40,55,56] and enables mapping the spectral and spatial distribution of surface and localized plasmon polaritons.[40,42] For gold, this spectral information is accessible up to the interband transition threshold

of about 2.38 eV,[57–59] beyond which interband absorption results in a uniform intensity distribution.[60]

1.5 Dissertation outline

After introducing the basic concepts of plasmonic excitations and electron microscopy with its analytical capabilities in the form of EELS and CL measurements, the following chapter 2 covers the performed experimental work on a practical level. In the scope of this thesis, three different systems were investigated regarding their plasmonic properties and phenomena. The fabrication and sample preparation processes of these three nanostructures are described, followed by an introduction of the utilized equipment and applied measurement techniques in the field of analytical electron microscopy and optical spectrometry. Digital processing procedures and simulations were used to improve the data quality and to confirm experimental findings, respectively. The scientific outcome of all three projects is presented in chapter 3 in close relation to the original publications, starting with the investigation of plasmonic edge modes and their interaction with defect structures in Bi_2Se_3 nanoplatelets. In section 3.2, the two interaction mechanisms "reflection" and "phase-matching" of fast electrons with plasmonic modes on gold tapers and their dependence on the opening angle are reviewed. New measurements that directly prove the "phase-matching" mechanism through the use of variable acceleration voltages are presented. The investigation of true chiral plasmonic structures in the form of left- and right-handed gold nanohelices is summarized in section 3.3. In this comprehensive study, both excitation and radiative decay of longitudinal plasmonic modes are investigated via EELS and CL in combination with optical measurements and simulations. Special attention is payed to the

polarimetric characterization of the emitted far-field radiation regarding its circular polarization state. Finally, a conclusion of the thesis is provided in the last chapter 4.

2 Experimental methodology

The scientific investigation of nanomaterials and 3D structures on the nanoscale is an interesting and promising research area. Especially electron microscopy provides highly capable analytical tools in this regard. However, experimental investigations on such small scales require specialized techniques, instruments and processes. This involves the sample fabrication and subsequent preparation for experiments, as described in the following section 2.1 for Bi_2Se_3 nanoplatelets, plasmonic gold tapers and chiral nanohelices, and the actual measurements. Foremost, section 2.2 on page 31 covers all techniques related to analytical electron microscopy, that were utilized in this work. This includes EELS measurements in the form of energy-filtered transmission electron microscopy (EFTEM) series and STEM-EELS spectrum image (SI) acquisition with the ZEISS sub-electronvolt sub-angstrom microscope (SESAM), as well as spectral and angle-resolved CL measurements including polarimetric investigations, that were performed on a ZEISS SEM. The 3D shapes of nanostructures were reconstructed via electron tomography (ET), as described in section 2.2.5 on page 39. For the same reason, but in two dimensions, atomic force microscope (AFM) was used to investigate the structural quality of defect structures in Bi_2Se_3 nanoplatelets. Optical measurements in the form of generalized spectroscopic ellipsometry to determine the dielectric tensor of grown Bi_2Se_3 thin films and circular dichroism (CD) spectroscopy to measure the chiroptical

response of left- and right-handed nanohelices were performed to link nanoscopic phenomena to observable macroscopic material properties. The acquired raw data need to be processed to some degree, either for calibration purposes or to improve the spectral quality. Finally, simulations were performed as described in the last section of this chapter on page 45, to confirm the experimental measurements and give further insight into the underling physical processes.

2.1 Sample fabrication and preparation

2.1.1 Bi_2Se_3 nanoplatelets

The synthesis of thin Bi_2Se_3 platelets was accomplished through a catalyst-free vapor transport method.[61–63] The process is sketched in figure 2.1. Ultra-pure Bi_2Se_3 is placed inside a quartz tube and positioned in the hot zone of a tube furnace. The glass cylinder is iteratively evacuated and purged with pure argon (Ar) gas prior to the growth process to remove residual oxygen. While being heated to 590 °C for several minutes, the constant Ar-flow of 50 sccm transports the evaporated (semi-)metal atoms around 10 cm down the gas-stream, where they are deposited on a Si/SiO_2 wafer-plate. As they preferably attach to the dangling bonds at the side walls of already grown crystals, nanoplatelets are formed, consisting of a single or only a few quintuple layers (QLs).

The 2D crystals were transferred onto a TEM sample grid by an all-dry technique to minimize contamination due to solvents.[64] After positioning the wafer upside down on the amorphous carbon support film, a small amount of applied downward pressure is sufficient for the transfer of nanoplatelets to occur

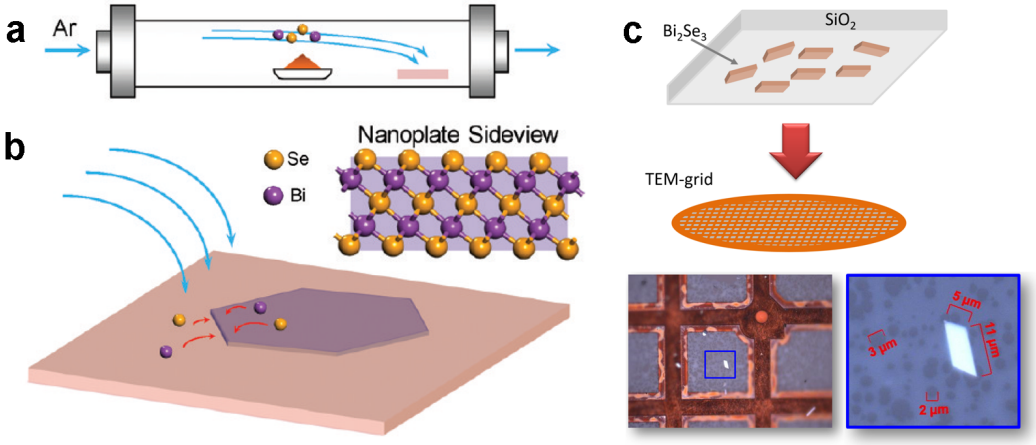

Fig. 2.1: Nanoplatelets of Bi_2Se_3 are grown through a catalyst-free vapor transport method. (a) Pure Bi_2Se_3 is placed in the hot zone of a quartz tube furnace. Under vacuum conditions and a constant flow of pure Ar gas, material is deposited on a Si/SiO_2 substrate approximately 12 cm away (b), where two-dimensional (2D) crystals form. (c) Nanoplatelets are transferred onto TEM sample grids via solvent-free stamping. Images a) and b) are adapted from the original publication.[62]

through adhesive van der Waals (vdW) forces. On the other hand, lateral movement has to be avoided in order not to damage the support film.

Creating defect structures at clean edges of large nanoplatelets was performed by milling with the focused ion beam (FIB) *Raith ionLine Plus* system in the nanostructuring lab at the 4$^{\text{th}}$ Physics Institute at the University of Stuttgart. In this instrument, dedicated for high-resolution structuring, double-charged gold ions (Au^{++}) are accelerated by an applied voltage of 35 kV. Ion implantation was unproblematic, as milling was performed through the entire material of very thin nanoplatelets and the amorphous carbon support film, rather than into bulk material. However, milling doses needed to be adjusted very carefully and were in the range of 0.05 nC µm^{-2} with a beam current of 11.3 pA. Larger doses than required for milling through a nanoplatelet result in damage of the

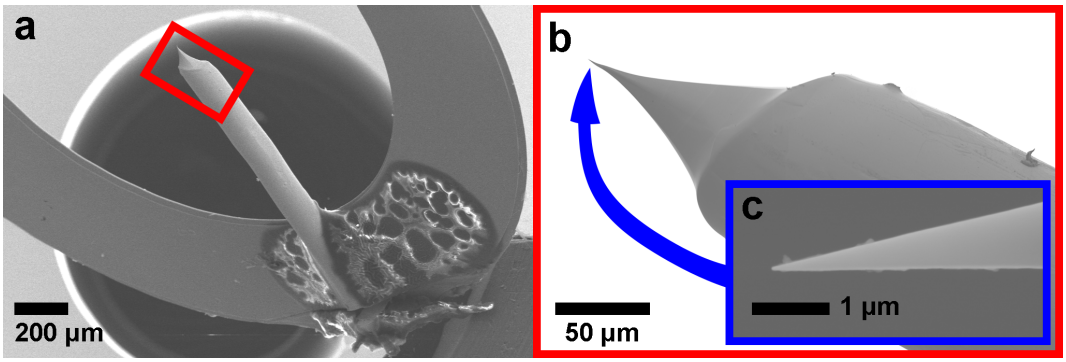

Fig. 2.2: (a) A fabricated gold taper is installed on a copper ring for further SEM and TEM investigations. (b) The sharp tip has an opening angle of 13° and a radius of curvature at the apex of 30 nm, as determined from the the magnified image (c).

support film. Especially, when holes are in close proximity to the particle to be structured, the film folds away, leaving behind an unsupported and consequently unstable Bi_2Se_3 nanoplatelet.

2.1.2 Single-crystalline gold tapers

Nanoscopic gold tapers were produced and provided by collaborators,[65] following the production process as described earlier.[66–68] The initial material in the form of pure poly-crystalline gold wires with a diameter of 125 µm is annealed at 800 °C for 8 h and slowly cooled down to room temperature. The transformation to the conical shape is achieved by electrochemical etching in hydrochloric acid (HCl) with an aqueous solution of 37 %, through the application of rectangular voltage pulses between the wire and a concentrical platinum ring, serving as cathode. The resulting tapers with apex curvature-radii down to 25 nm terminating the gold wires were centrally mounted on TEM copper rings with an electrically conductive epoxy (figure 2.2).[69,70]

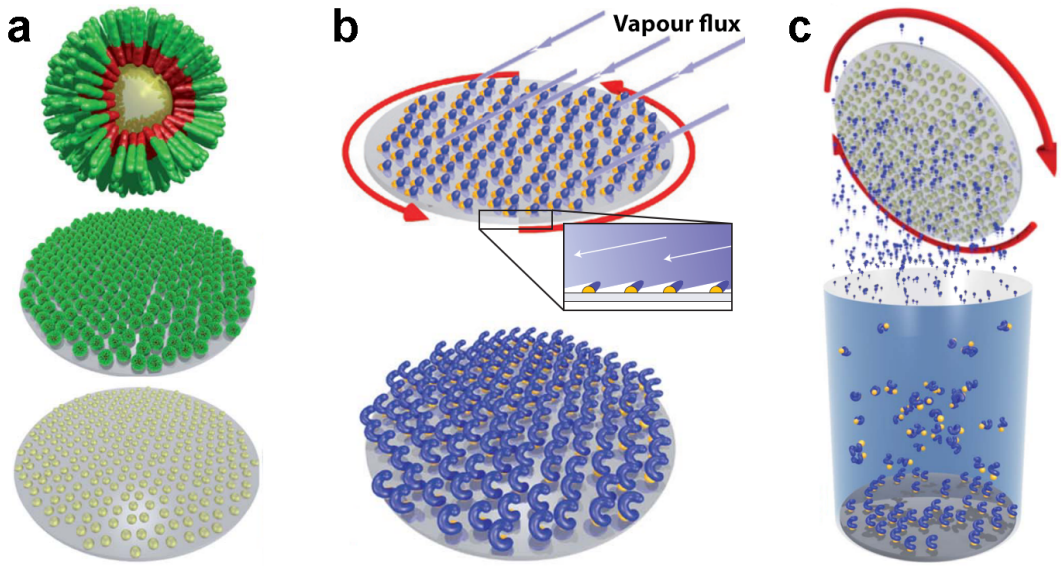

Fig. 2.3: The production of gold nanohelices is achieved in three main steps. After patterning the seed array of gold dots via BCML (a), helices are grown by shadow-growth GLAD while rotating the sample stage (b). The fabricated structures are immersed into aqueous solution by ultrasonic treatment (c). Graphics taken from the original publications.[75,76]

2.1.3 Chiral gold nanohelices

A combination of block copolymer micellar nanolithgraphy (BCML)[71,72] and glancing-angle deposition (GLAD)[73] in a shadow-growth technique,[74] where the physical vapour deposition (PVD) of the material occurs under a dynamic oblique angle of incidence, was utilized to grow the nanoscopic gold helices.[75,76] The three main production steps are shown in figure 2.3. In an initial step, a solution of self-assembled spherical inverse block copolymer micelles, containing gold salts in their centers, is spin-coated on a silicon wafer, where a monolayer with a quasi-hexagonal pattern is formed. Subsequent plasma etching removes the polymer and reduces the metal salt cores. The resulting gold dots with 17 nm size are arranged in an array with 90 nm distance to each other and act

as seeds for the following growth process. Both parameters are adjustable by varying the experimental conditions.

The material of choice, in this case gold, is vaporized by electron beam heating and deposited onto the seeded substrate, which is tilted to the oblique angle of incidence of 85° and slowly rotated around its normal axis during the growth process. Geometrical parameters such as length, thickness, pitch or handedness of the helices are further controlled through the combination of evaporation rate, deposition time and rotation speed and direction.

The diffusion of deposited gold adatoms negatively influences the structural morphology and is effectively suppressed by cooling the substrate to a temperature of $-10\,°\mathrm{C}$ by an Peltier element.

Both left- and right-handed gold helices were fabricated on wafers under equal conditions and immersed into pure water by ultrasonic treatment.

Helix samples were supplied in a concentration of $1.85 \times 10^9\,\mathrm{ml}^{-1}$ and further diluted by a factor of 5, yielding an appropriate solution for TEM sample preparation on mesh-200 copper grids with an amorphous holey-carbon film (Plano GmbH, Item S147-2), following the procedure as shown in figure 2.4. After ultrasonic treatment for 30 s, the sample-containing solution is applied on the hydrophobic surface of a paraffin film, resulting in a round droplet due to surface tension effects. The TEM grid is brought into contact and consequently retracts a small amount of the liquid. Single particles are distributed over the membrane and remaining solvent is soaked off by a tissue. These steps can be repeated iteratively to increase the concentration.

The prepared TEM sample grid is dried in vacuum and subsequently mounted on a sample holder with temperature control. Being inserted into the microscope,

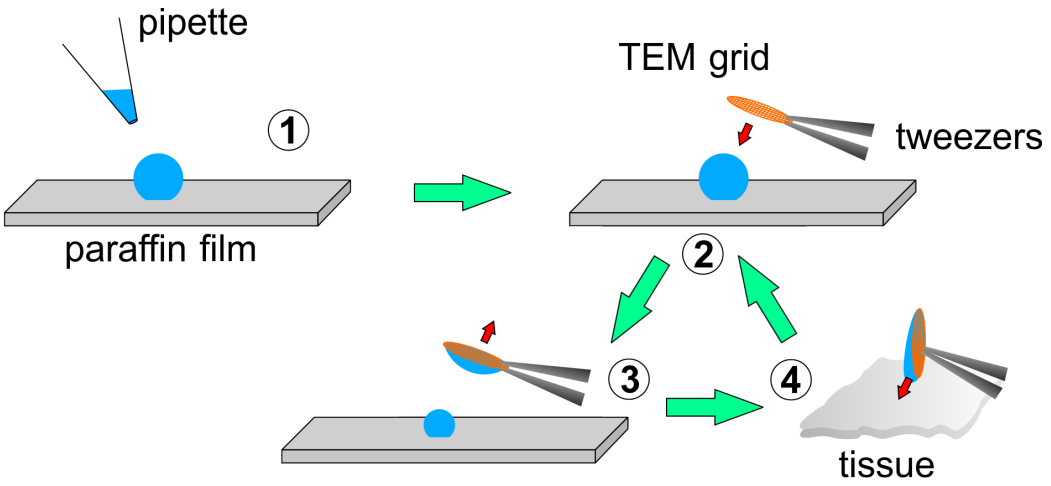

Fig. 2.4: Drop-and-soak procedure to prepare a TEM sample grid with nanoparticles supplied in aqueous solution. A droplet of the liquid is applied to a paraffin film (1) and partly exposed to the membrane of a TEM grid (2) and (3). Remaining solvent is retracted with a tissue (4). Steps (2), (3) and (4) can be repeated iteratively to increase the overall density of particles.

it is slowly heated to 400 °C to remove any residual mobile hydrocarbons and thereby prevent critical contamination problems during the measurements. After returning to room temperature, the system needs time to reach thermal equilibrium for mechanical drift to decay.

2.2 Analytical electron microscopy measurements

Modern electron microscopes enable imaging on a nanoscopic or even atomic level through their high resolving capabilities either in the conventional mode with a close-to-parallel beam illumination or by scanning the ROI with a focused electron probe at high spatial sampling. As described in section 1.4 on page 22, the inelastic interaction of the fast electrons with the specimen

generate many different kinds of signals, that can be detected (in most cases) simultaneously to the imaging process. As a result, their analysis not only provides scientific information about intrinsic material properties, but in addition this information is linked to the spatial excitation position, which is highly beneficial for phenomena that are related to geometrical properties of nanostructures, as investigated in the scope of this thesis.

The following sections provide descriptions of how these analytical measurements are performed with the dedicated instruments. In general, all techniques have in common to store the acquired signals in a multi-dimensional dataset.

2.2.1 ZEISS SESAM electron microscope

EELS measurements were performed using the ZEISS SESAM (figure 2.5 a).[77] This instrument is ideally suited for low-loss investigations because of its high energy dispersion at good stability. Electrons are extracted from a Schottky field emission gun (FEG) and pass through an electrostatic Ω-type MCR, before they are accelerated via a stabilized high-tension of 200 kV. After interacting with the sample, which is located between the two pole pieces of the objective lens, the trajectories of inelastically scattered electrons are dispersed by multipole magnets within the unique in-column MANDOLINE energy filter (figure 2.5 b). In combination with the MCR, an energy resolution of slightly below 70 meV can be achieved, measured as FWHM of the ZLP (figure 2.5 c). This performance is still impressive, especially for a comparably old instrument. Only recently, investigations with an energy resolution below 10 meV have become accessible by state-of-the-art electron microscopes, which corresponds to the energy range used in THz spectroscopy and enables the study of lattice-vibrations (phonons) by analytical electron microscopy.[79]

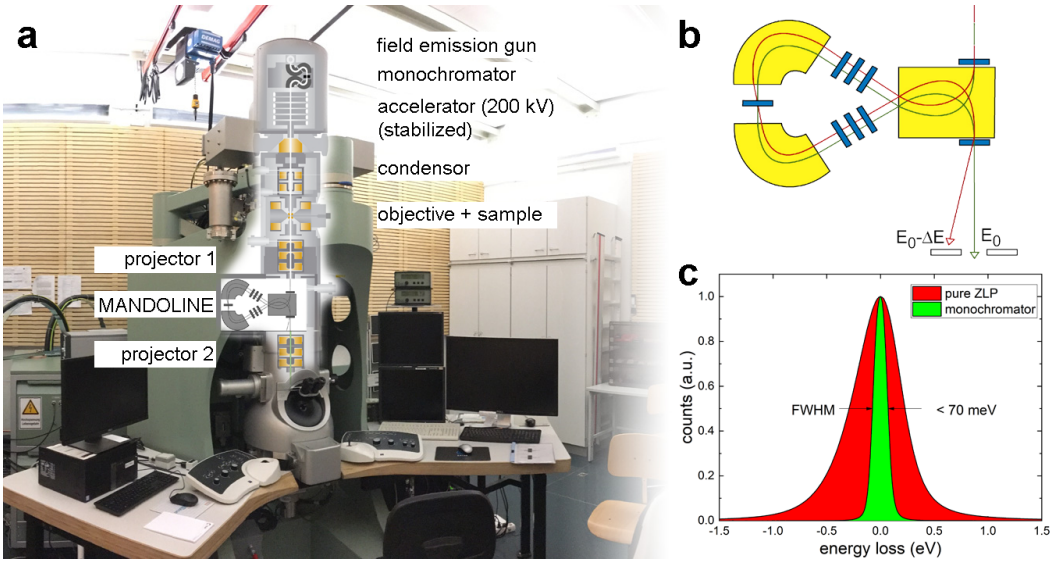

Fig. 2.5: (a) ZEISS SESAM microscope with implemented sketch of the column. (b) MANDOLINE in-column energy filter. (c) Possible energy-resolution, measured for an unaffected electron beam. The technical sketches are adapted from the original publication.[78]

Energy-loss measurements are possible in two significantly different configurations that are linked to the operation modes TEM and STEM of the electron microscope and are described in the following sections. Both methods result in a 3D data cube with two spatial dimensions and one energy-dispersive axis.

2.2.2 Energy-filtered transmission electron microscopy

For EFTEM measurements, the electron microscope is operated in conventional TEM mode, where the area of interest is irradiated with a close-to-parallel electron beam (figure 2.6 a). Energy filtering is achieved through a combination of suitable slit apertures that are inserted into the beam path at the position of the MCR and the exit plane of the MANDOLINE energy filter. As defined by their widths, only electrons within a limited kinetic energy range are transmitted

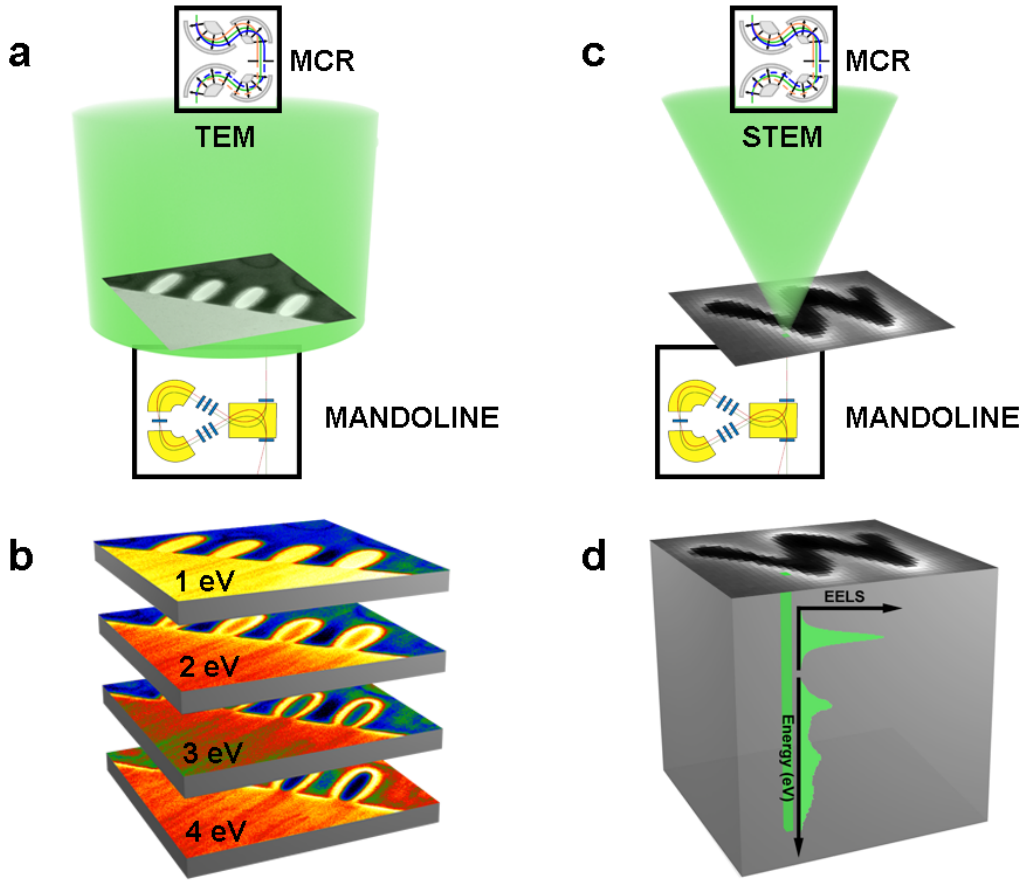

Fig. 2.6: (a) For EFTEM imaging, the ROI is irradiated with a monochromated close-to-parallel electron beam. Only electrons that have experienced an energy-loss within a certain range are transmitted by the filter and contribute to the image. (b) The 3D data cube is formed via offsets to the initial kinetic energies. (c) For STEM-EELS measurements, the ROI is raster scanned by a monochromated convergent electron beam. (d) Electrons are energetically dispersed by the energy filter and detected as spectrum per spatial pixel. The technical sketches are adapted from the original publication.[78]

and contribute to the captured image (figure 2.6 b). For experimental reasons, the beam path and the apertures are optimized for the zero-loss electrons. To acquire EFTEM images at certain energy-loss ranges, this amount is added to the initial kinetic energy at the acceleration stage. The 3D data cube with two spatial axes and one energy-loss axis is formed, by capturing images filtered for different energy-loss ranges with a step width of 200 meV. With this method, comparably large areas up to several micrometers can be investigated at good spatial sampling, however, with the drawback of limited energy resolution. Within this work, EFTEM imaging was performed to investigate clean and artificially structured edges of Bi_2Se_3 nanoplatelets (section 3.1 on page 49) and plasmonic modes on gold tapers (section 3.2 on page 72).

2.2.3 Electron energy-loss spectroscopic imaging

SIs are acquired in STEM mode, where the ROI is raster scanned with a convergent electron beam (figure 2.6 c) and energy-loss spectra are measured for each spatial pixel in the 3D data cube (figure 2.6 d). Similar to EFTEM images, slices with adjustable energy-loss ranges can be extracted in post to generate spatially resolved intensity distributions. This technique is mostly used today in modern analytical TEMs and the only possible implementation in dedicated scanning instruments. As technology has improved over time and the efficiency of electron detection has increased, for example through the use of modern direct electron detetors, also large areas can now be investigated with good spatial sampling in a reasonable time. In addition, different signals and detectors are simultaneously used for imaging and analytical measurements, so that drift-correction algorithms can be applied to keep the ROI centered.

For the ZEISS SESAM, the implementation of STEM-EELS measurements

is less advanced and comes with several drawbacks. The detector for HAADF imaging is located after the energy filter in the microscope column and partly covers the CCD, on which the energetically dispersed electrons are projected and hence must be retracted for energy-loss measurements. In addition, a different operation mode of the filter itself and an entrance aperture is required for spectral acquisitions. For the given reasons it is not possible to measure spatial and spectral data simultaneously and an in-situ drift-correction is not applicable. The accumulated drift can only be determined after a measurement by comparison with an initial image. In contrast to the aforementioned EFTEM measurements, the much higher energy-resolution for STEM-EELS around 70 meV is achieved by using the smallest MCR slit aperture and a spectral dispersion of 5 meV per channel on the CCD.

2.2.4 Cathodoluminescence measurements

The original CL measurements on plasmonic gold tapers[70] were conducted with a STEM *Vacuum Generator HB501*, which is equipped with a cold field emission electron gun and operated at an acceleration voltage of 100 kV. For spatial mapping, a few-nanometer-sized electron probe with a beam current of around 1 nA was used and the emitted far-field radiation was analyzed with the *Attolight Mönch* STEM-CL setup.

All other CL measurements were performed using a ZEISS SIGMA field emission SEM (figure 2.7 a). Optical spectroscopy capabilities are achieved by the implementation of a parabolic mirror that is positioned below the pole piece (figure 2.7 b). The specimen in its focal point is excited by the electron beam that passes through a hole in the mirror with a diameter of 0.6 mm. Emitted far-field radiation is collected and guided outside the microscope chamber, where it

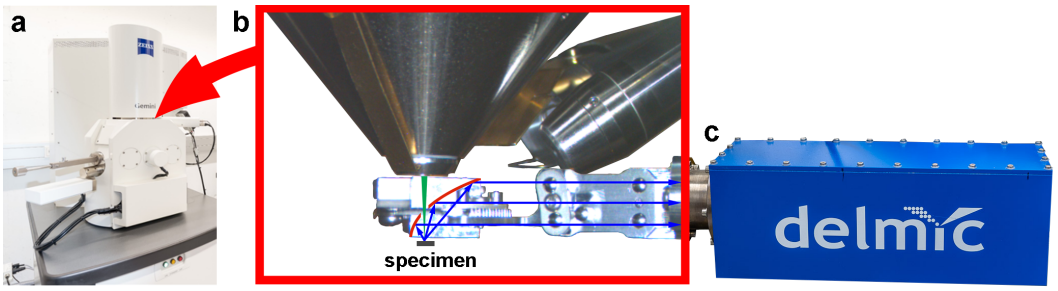

Fig. 2.7: (a) ZEISS SIGMA scanning electron microscope. (b) The parabolic mirror is placed directly below the polepiece. The specimen in its focal point is excited by the electron beam and the emitted CL radiation guided towards the external spectrometer (c).

is analyzed in the attached *delmic SPARC* system (figure 2.7 c). Measurements can be performed in several experimental configurations. Two of them were used in the scope of this work and are described in the following sections.

2.2.4.1 Cathodoluminescence spectroscopy

In the spectroscopic mode, the emission is detected per spatial pixel of the scanned ROI either as a dispersed spectrum or filtered for certain wavelength windows with a high signal-to-noise ratio (SNR). The resulting dataset contains also spatial information as provided by the SE detector. It is very important to note that the intensity, mapped to a certain spatial pixel, is not emitted at this position but rather from the entire structure or specimen. What can be investigated is the relation between the spatial excitation position by the electron beam and the amount of light that is generated and can be interpreted as spatial excitation efficiency.

In this work, CL spectroscopy was used for all three projects to characterize the emission of Bi_2Se_3 thin films (section 3.1 on page 49), plasmonic gold

tapers (section 3.2 on page 72) and nanohelices (section 3.3 on page 89). The microscope was operated at an acceleration voltage of 20 kV and a resulting probe current of 10.4 nA. Spectra were acquired with an exposure time of 200 ms, a 220 µm entrance slit aperture and a grating with a line density of 150 mm^{-1}.

2.2.4.2 Angle-resolved polarimetry

In a second configuration, the detected signal is related to its emission direction for a fixed excitation position and wavelength window with a bandwidth of 50 nm. These angle-resolved measurements[80,81] can be complemented by inserting a quarter wave plate (QWP) and a linear polarizer into the beam path,[82] which allows for a full characterization of the polarization state via Stokes parameters (figure 2.8). Especially important regarding the characterization of chiral nanostructures, as performed in this work, is the different behavior concerning left circularly polarized (LCP) and right circularly polarized (RCP) light. Their normalized differential intensity defines the Stokes parameter S3 according to

$$\mathrm{S3} = \frac{I_{\mathrm{LCP}} - I_{\mathrm{RCP}}}{I_{\mathrm{LCP}} + I_{\mathrm{RCP}}}. \tag{2.1}$$

The characteristics of circularly polarized light (CPL) and its interaction with a QWP and linear polarizer are described in more detail in section 2.4.2 on page 44.

As the directional information is linked to different ray paths, the intensity can not be accumulated over the entire accessable angular range, which results in a significantly reduced SNR of the detected signal. Therefore, measurements were performed with an exposure time of 30 s for each filter configuration.

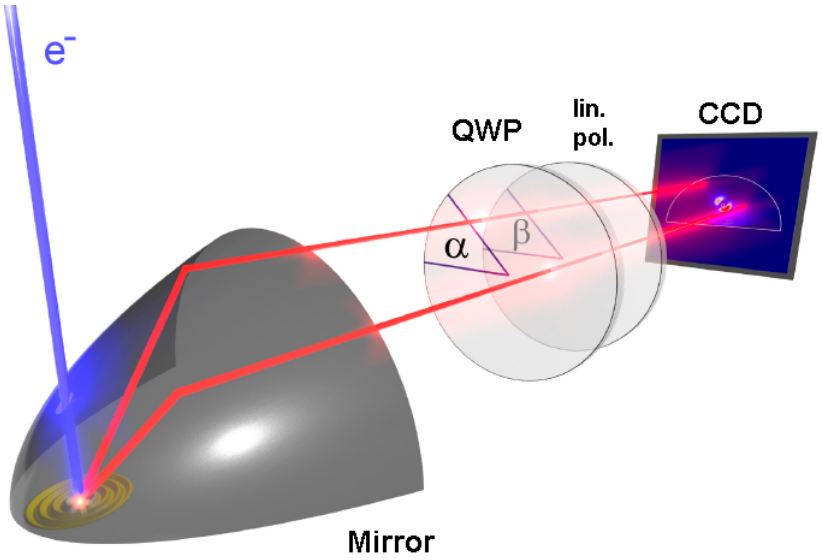

Fig. 2.8: The emitted light is reflected by the mirror and subsequently analyzed through a combination of a QWP and a linear polarizer. The resulting signals are detected separately with spatial resolution and allow for the reconstruction of emission directions. Image adapted from the delmic technical note about "Polarization-Filtered Cathodoluminescence Imaging".[83]

Leaving the electron beam stationary over such a long time may lead to a contamination of the investigated ROI by accumulated mobile hydrocarbons. For the given reasons, measurements of left- and right-handed chiral nanohelices were limited to a promising wavelength range around 800 nm and only a few efficient excitation positions, as determined by preceding spectroscopic CL measurements.

2.2.5 Electron tomography

In the usual imaging processes of a 3D object of interest, either in conventional light microscopy or by using fast electrons, the volumetric information is lost,

as only a 2D projection along the viewing direction is captured. Similar to the requirements for stereoscopic vision, additional perspectives are needed to reconstruct the 3D information. For ET, this is achieved by rotating the object of interest under electron-beam irradiation and acquiring images at various tilt angles.

In the scope of this thesis, ET was utilized to reconstruct the 3D shape of left- and right-handed nanohelices to experimentally confirm the different handedness of the chiral structures. Therefore, TEM grids containing the nanohelices were cut in an orientation to enable the maximum accessible tilt range before shadowing occurs (figure 2.9 a) and glued onto the grid support rod of the dedicated tomography holder *GATAN Model 912* (figure 2.9 b). Images of left- and right-handed nanohelices were acquired as tilt-series in 1° steps over the accessible angular range from 77° to −58° and 84° to −66°, respectively. Turning nanoscopic structures over high angular ranges while being viewed at high magnifications requires a good mechanical alignment of the sample stage inside the electron microscope. In order to avoid strong sample shifts, the nanoscopic object must be placed in the rotation axis of the goniometer. This is achieved by stage movements in z- and y-direction, when rotated around the x-axis. The alignment can be optimized iteratively for both directions by reducing relative sample shifts compared to the neutral position (figure 2.9 c). Most importantly, in case the object of interest needs to be brought back to the field of view, this compensation needs to be done by an artificial image shift, so that the mechanical alignment is not affected. Imaging was performed in conventional illumination mode with a *JEOL ARM-200F* electron microscope operated at 200 kV. The acquired image stacks were spatially aligned by cross-correlation filtering and used to reconstruct the 3D shape of the structure by applying the weighted back projection (WBP) algorithm. The subsequently

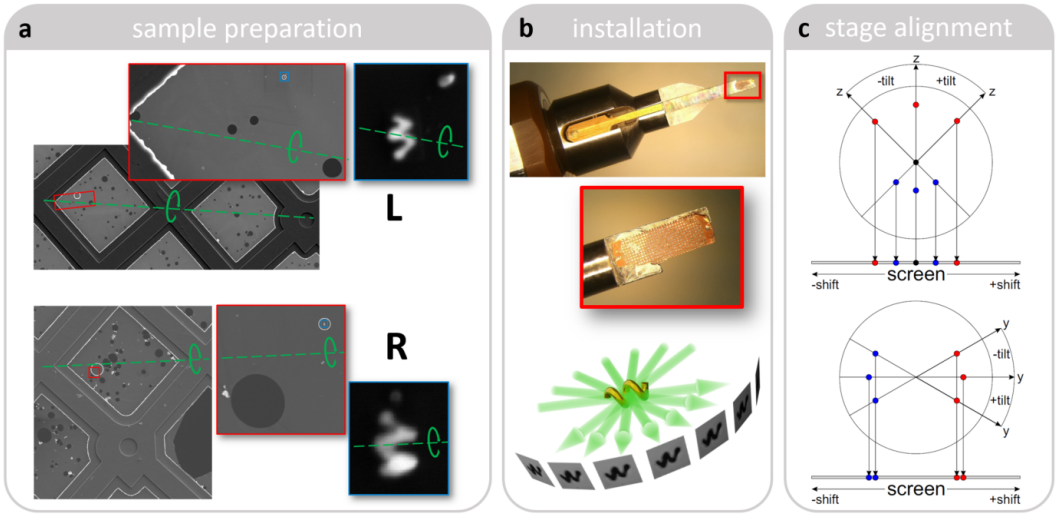

Fig. 2.9: (a) Sample grids containing the particles of interest for electron tomography are cut in a way that shadowing effects during the tilt series acquisition around the rotation axis (green dashed line) are minimized. (b) The prepared grid is mounted onto the tip of the tomography holder that allows for tilt angles between $\pm 70°$ inside the electron microscope. (c) Expected relative sample shifts when tilted away from the neutral position for assumed positive (red) and negative (red) misalignments along the z- and y-axis as shown in the upper lower graphics, respectively.

applied simultaneous iterative reconstruction technique (SIRT) optimized this initial model further by continuously comparing slices of the reconstructed volume with the original images of the tilt series.[84]

2.3 Atomic force microscopy

The AFM was invented by Gerd Binnig[85] and realized together with colleagues at IBM in the year 1986[86]. Interestingly, the Nobel prize for physics was awarded to him and Heinrich Rohrer in the same year for their earlier invention of the scanning tunneling microscope (STM)[87,88] that was also implemented

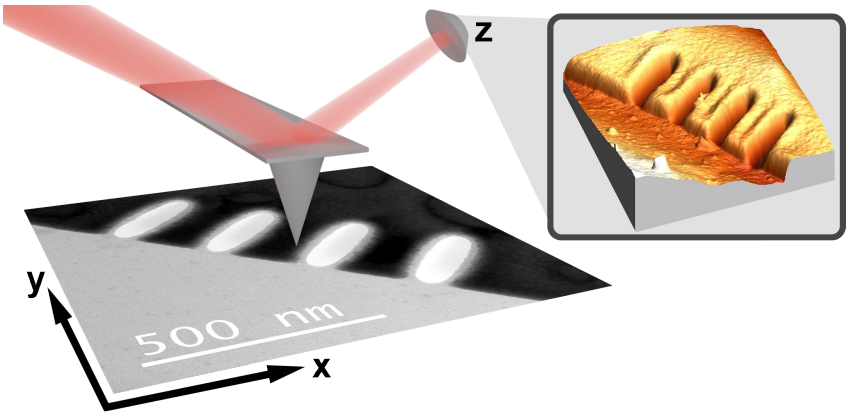

Fig. 2.10: In an AFM, the ROI is raster scanned with a sharp tip located at the end of a cantilever. Interatomic interactions between the surface and the tip lead to small perturbations in the z-height, which are measured optically and transformed into a height-profile via feedback-electronics.

in the first version of this new type of scanning probe microscope. A sketch of the very basic priciple of an AFM is shown in figure 2.10. A sharp tip at the end of a cantilever is lowered and brought in contact with the sample surface. Strong short-range repulsive forces between atoms at the tip and the sample surface slightly deflect the cantilever, which is detected optically, for instance by a reflected laser and a photodiode. One way to extract the height information of the surface while spatially scanning the ROI is to restore the original signal by adjusting the physical z-height via feedback electronics.

In the scope of this work, atomic force microscopy was used to characterize the structural quality of engineered defects, that were created at clean edges of Bi_2Se_3 nanoplatelets via FIB milling.

2.4 Optical measurements

Electron microscopy with its high spatial resolution and analytical possibilities is a very powerful technique for investigations on the nanoscale. It enables further insight and deeper understanding of phenomena that on the one hand occur on a nanoscopic level, but on the other hand do have an influence on macroscopic material properties, which are accessible by well-established optical characterization techniques.

2.4.1 Generalized spectroscopic ellipsometry

Ellipsometry in general is an optical technique to investigate the dielectric properties of materials and is based on the change of polarization states when interacting with a sample thin film or surface. In the typical experimental realization of specular reflection, the incident and reflected light beams span a plane of incidence. The light can be decomposed into p-components (polarization parallel to the plane of incidence) and s-components (polarization perpendicular to the plane of incidence and parallel to the interface) and their reflection at the surface treated separately following the Fresnel formalism.[89] Experimentally, the amplitudes of both polarization states are measured after reflection and subsequently used to indirectly determine material properties such as the dielectric tensor via a model-based interpretation.

In this work, the technique of generalized spectroscopic ellipsometry was utilized to determine the dielectric functions for the in-plane and out-of-plane directions of grown Bi_2Se_3 thin films and identify spectral regions with hyperbolic behavior as described in section 3.1 on page 49.

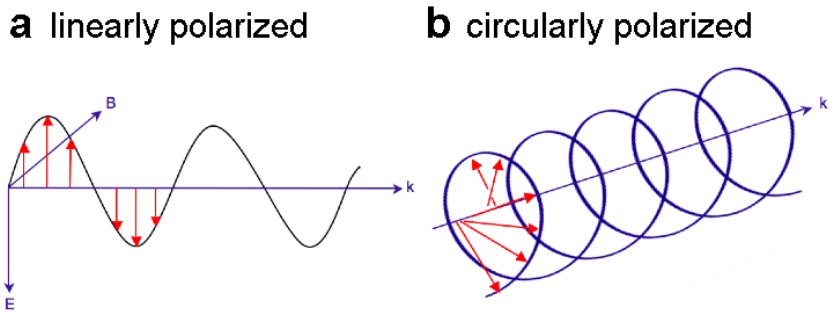

Fig. 2.11: (a) For linearly polarized light, the electric field (red arrows) oscillates in a plane perpendicular to the propagation direction. (b) For circularly polarized light, the electric field vectors rotate at full amplitude in a plane perpendicular to the propagation direction. Images adapted from Wikipedia (public domain).

2.4.2 Circular dichroism spectroscopy

The principle of CD measurements is based on the different amount of absorption of left and right CPL. In contrast to linearly polarized (LP) light, where the electric field vector oscillates in one plane, it rotates in the plane perpendicular to the propagation direction with full amplitude (figure 2.11 a and b). For a wave propagating towards the observer, this circular motion occurs clockwise or anticlockwise for RCP or LCP light, respectively.

Experimentally, CPL can be realized by sending LP light through a QWP with an angle of 45° between the plane of polarization an the optical axis of this optical element. Other angles result in elliptically polarized light. The required thickness of the QWP can be optimized for one "color" only, as the effect is wavelength-dependent.

While passing through optically active media, such as solutions of chiral molecules or nanostructures, both propagation speed, wavelength and absorption coefficients differ for LCP and RCP light, resulting in the measureable

differential CD signal according to

$$\mathrm{CD} = \frac{Ext_{\mathrm{LCP}} - Ext_{\mathrm{RCP}}}{Ext_{\mathrm{LCP}} + Ext_{\mathrm{RCP}}}, \tag{2.2}$$

where Ext_{LCP} and Ext_{RCP} denote the extinction cross sections for LCP and RCP light, respectively.[90,91] A related effect concerns the rotating plane of polarization of LP light passing through a chiral medium, which is known as optical rotation (OR), and its wavelength-dependence as optical rotatory dispersion (ORD).[92] These techniques are widely used as powerful characterization tools in biological, medical, chemical or physical applications.[93]

In the scope of this work, CD measurements were performed to obtain the chiroptical response of left- and right-handed gold nanohelices, which were sonicated off a cut substrate into 1 ml of purified *Milli-Q®* water. Assuming a hexagonal array of nanoparticles, the colloidal concentration is around $1.85 \times 10^9\,\mathrm{ml}^{-1}$. Left- and right-handed helices were measured separately with a *Jasco J-810 CD* spectrometer as reported in previous work.[75]

2.5 Data processing

Some of the acquired raw data need to be processed, either to correct for measurement-related issues, to improve the quality via noise reduction techniques or extract hidden spectral details.

EELS For energy-loss measurements performed at the SESAM, the spectral data must be calibrated after the acquisition with the ZLP and the correct dispersion. For experimental reasons as described in section 2.2.2 on page 33,

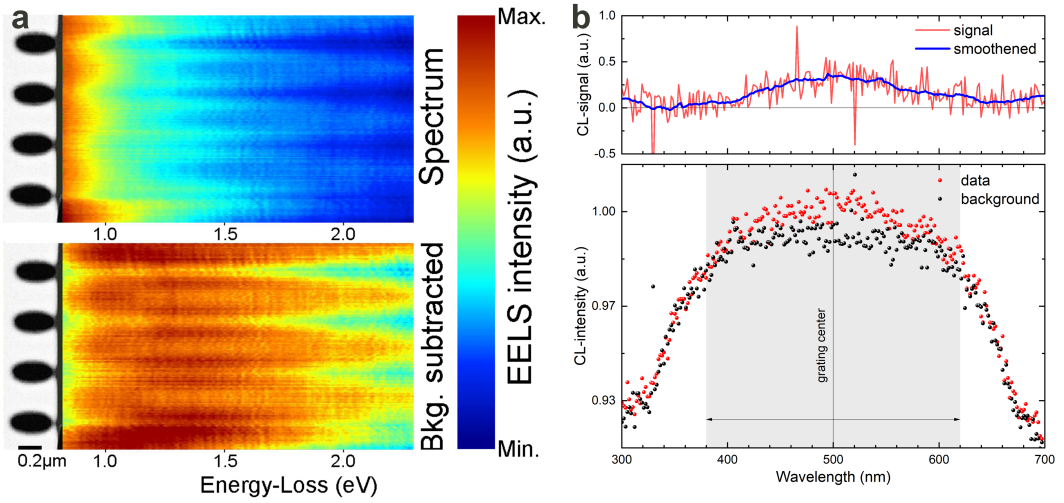

Fig. 2.12: (a) EELS linescans displayed as energy-distance maps before (upper graphic) and after background subtraction (lower graphic). (b) for CL

slices of an EFTEM series are separated by 0.2 eV. Because of instabilities during the measurements, all spectra contained in a SI must be calibrated individually. This is done via a plugin script in the Digital Micrograph (DM) microscopy software that identifies and centers each of the zero-loss peaks at 0 eV and needs to be applied three times to yield good results. Consequently, the very intense ZLP must be measured together with the spectral data and limits the possible exposure time to prevent damaging the CCD camera. An option to acquire both spectral parts separately with different exposure times (dual-EELS) is not available at this microscope.

Plasmonic spectral features at low energy losses might be overshadowed by the bright ZLP (figure 2.12 a). Their visibility can be increased by subtracting the background signal which is related to its tail, in this case by fitting a power-law function. However, many other approaches are discussed in the literature, including mirroring the spectrum in the case of symmetric monochromated

ZLPs and machine learning algorithms.[94]

CL The emitted far-field radiation of an excited nanostructure is measured at a comparably large distance with intensities that are only a few percent above the dark signal of the detector (figure 2.12 b, lower graph). Reference measurements with a blanked beam are required for each experimental setting to extract the signal of interest (upper graph).

Noise reduction Data with a low SNR were treated with a combination of principle component analysis (PCA)[95,96] and subsequent smoothing via the application of a Savitzky-Golay algorithm (blue line in the upper graph of figure 2.12 b).

2.6 Simulations

In the scope of this work, different kinds of numerical simulations were performed to complement the experimental results. They are all based on solving Maxwell's equations under boundary conditions as given by the experimentally determined geometries of the structures. Besides confirming the experimental measurements, simulations contribute to a deeper understanding, for example through visualizations, that are experimentally either difficult or even impossible to realize, such as movies of propagating plasmonic modes via finite-difference time-domain (FDTD) simulations[97] or dispersion diagrams by using the finite-difference frequency-domain (FDFD) approach.[98] For numerical EELS calculations, the anisotropic permittivity of Bi_2Se_3 was described by the Drude model in combination with a function to implement interband transitions.[60]

For gold nanohelices, a tabulated dielectric function in the energy range from 0.1 eV to 6 eV was used.[99] To account for substrate effects, the structures were embedded in an effective medium with a dielectric constant of 2.8. Electron energy-loss spectra were simulated by the boundary element method (BEM) using the *MNPBEM toolbox*.[100] For CL simulations, the *COMSOL Multiphysics* software package with its radiofrequency (RF) toolbox was used.

3 Results

This chapter is dedicated to present the scientific results that were acquired in the scope of this thesis. The three projects are summarized in sections 3.1, 3.2 and 3.3 and are based on my own first-author publications (B), (A) and (D), respectively, as listed on page xiv. Therefore, large parts are implemented without rephrasing or rewording.

3.1 Interaction of hyperbolic edge exciton polaritons with defects

Hyperbolic materials exhibit unique properties that enable intriguing applications in nanophotonics. The topological insulator Bi_2Se_3 represents a natural hyperbolic optical medium, both in the terahertz and visible range. Here, using CL spectroscopy and EELS, we demonstrate that Bi_2Se_3 supports room-temperature exciton polaritons and explore the behavior of hyperbolic edge exciton polaritons (HEEPs), which are hybrid modes resulting from the coupling of the polaritons bound to the upper and lower edges of Bi_2Se_3 nanoplatelets. Although polaritons in Bi_2Se_3 and Bi_2Te_3 have been demonstrated before,[101–103] the origin of the observed polaritonic behavior had not

been revealed. Similar direct and indirect band gap excitonic excitations with strong oscillator strengths up to room temperature exist in either engineered heterostructures[104,105] or natural layered materials with vdW bindings.[106–110] We compare Fabry-Pérot-like resonances emerging in edge polariton propagation along pristine and artificially structured edges and experimentally demonstrate the possibility to steer edge polaritons by means of grooves and nanocavities. The observed scattering of edge polaritons by defect structures and their interaction with localized polaritons is found to be in good agreement with FDTD simulations.[111] Our findings reveal the extraordinary capability of hyperbolic polariton propagation to cope with the presence of defects, providing an excellent basis for applications such as nanooptical circuitry, nanoscale cloaking and nanoscopic quantum technology.

3.1.1 Hyperbolicity in Bi_2Se_3

In the past few years, anisotropic media with a hyperbolic dispersion have attracted significant attention due to their unique electromagnetic and optical properties.[112] A material is called hyperbolic, when its isofrequency surface given by

$$\frac{k_{\parallel}^2}{\epsilon_{\perp}} + \frac{k_{\perp}^2}{\epsilon_{\parallel}} = \left(\frac{\omega}{c}\right)^2 \tag{3.1}$$

forms a hyperboloid. Here, c is the speed of light and $k_{\parallel}$ and $k_{\perp}$ are the in-plane (x-y-plane) and out-of-plane (z-direction) components of the wave vector, respectively, describing the planewave propagation in the material at frequency ω. This hyperbolic condition is fulfilled, when at least one principle component of the dielectric tensor ϵ is negative.[113] A material with a negative real part of the dielectric function in the isotropic plane parallel to the surface ($\epsilon_{\parallel}$) is referred to as hyperbolic type-2 (HB_2), whereas a material

displaying a negative value in the out-of-plane direction ($\epsilon_\perp$) is of hyperbolic type-1 (HB_1) character. In contrast to closed isofrequency sheets, in hyperbolic materials propagation can occur at arbitrarily large wave vectors, resulting in a number of peculiar nanophotonic properties and applications such as negative refraction[114] or subdiffraction super-resolution imaging[115–118] right at the transition to the hyperbolic dispersion.[113] The main criterion for hyperbolicity is the motion of free electrons being constrained in one or two spatial dimensions, which can be experimentally realized by the construction of artificial metamaterials such as layered metal-dielectric structures[119–122] or based on silicon carbide particles.[123] Besides such artificial engineering, and even more intriguing, natural hyperbolic behavior has also been predicted and experimentally demonstrated, for example in graphite for UV frequencies,[124] in layered VDW materials in the visible range[125] and hexagonal boron nitride (H-BN) in the terahertz regime.[126–129] Tetradymites like Bi_2Se_3 structures are another class of hyperbolic materials in the visible range, as confirmed by spectroscopic ellipsometry measurements (figure 3.1).[130,131] Due to the anisotropic dielectric properties of the material, it becomes hyperbolic within distinct energy ranges between 1.06 eV and 1.74 eV and above 1.9 eV with type-1 and type-2 character, respectively.

3.1.2 Far-field radiation

We first investigate Bi_2Se_3 nanoplatelets using CL spectroscopy. Electrons traversing semiconducting materials undergo a series of inelastic events. Particularly, a number of electron–hole pairs is generated per electron excitation, which strongly depends on the energy of the incident electron and the band gap of the material. Therefore, CL spectroscopy is a deterministic tool for detecting

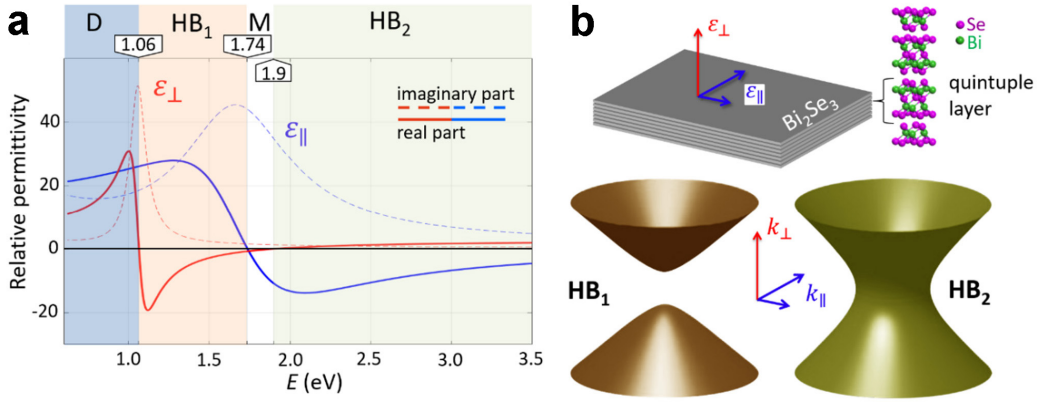

Fig. 3.1: (a) Relative permittivity of bulk Bi_2Se_3, acquired by ellipsometry measurements. Anisotropic guided waves (D), hyperbolic type-1 (HB_1) and hyperbolic type-2 (HB_2) waves are supported at the energies highlighted by blue, orange and green colors, respectively. (b) In-plane and out-of-plane directions within the layered vdW crystal and isofrequency sheets related to hyperbolic type-1 and type-2 behavior are shown in addition.

exciton-mediated radiation of the material. The CL intensity, emitted by an excited Bi_2Se_3 nanoplatelet was measured and spectroscopically analyzed in the visible range. The spectrum in figure 3.2 particularly shows two exciton peaks at the energies of 1.5 eV and 1.95 eV. These peaks are associated with the exciton transitions around the Q and F points of the Brillouin zone.[132] Exciton excitation between the quintuple layers (located at the Γ point of the Brillouin zone) happens at energies below 0.5 eV and is affected by the spin–orbit interactions, similar to the exciton peaks in MoS_2.[133] However, this energy range is out of reach of the used CL spectrometer.

The combination of excitonic excitations together with the hyperbolic nature of this material, thus leads to the emergence of hyperbolic exciton polaritons and in particular HEEPs. In the following, the properties of HEEPs and their interaction with anomalies will be discussed.

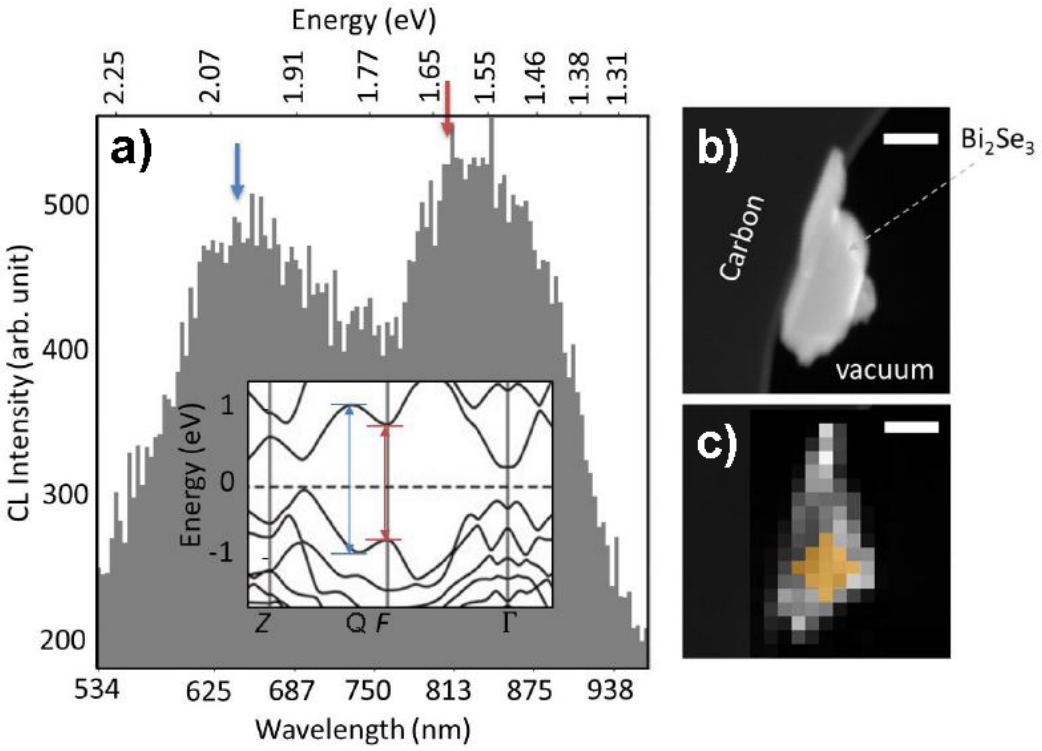

Fig. 3.2: CL spectrum (a) of a Bi_2Se_3 nanoplatelet (b), summed over the spatial points marked in yellow color (c). Two peaks are observed, which are associated with direct exciton transitions at the F and Q points of the Brillouin zone, that are related with in plane (within quintuple layers) bound exciton excitations. Interplanar exciton transitions (between quintuple layers) occur at the Γ point as well, however, their energy is out of range of the used spectroscopic instrumentation. Scale bars are 200 nm. Inset of panel (a) is adapted from the original publication.[132]

3.1.3 Edge exciton polaritons

Thin Bi_2Se_3 nanoplatelets were investigated further experimentally by means of analytical transmission electron microscopy. For that purpose, the area of interest was both irradiated with a parallel beam of fast electrons and spatially scanned by a focused electron probe. The energy-loss experienced by the electrons through their inelastic interaction with the specimen were analyzed with an energy-dispersive detection system (figure 3.3 a). Electron beams interacting with nanoplatelets in an aloof trajectory,[134] i.e., traversing the mode volume surrounding the side planes without passing through the material, can launch both surface waves and HEEPs. As will be discussed here, we observe a stronger coupling of the electron beam to HEEPs rather than surface waves. HEEPs in nanoplatelets propagate along the edges with their mode volume being sharply confined (figure 3.3 b).[135] In addition, those propagating at the upper and lower edges hybridize, very similar to surface polaritons in thin films, and form symmetric and antisymmetric modes. It should be mentioned though, that in contrast to directional zigzag-like propagation and scattering of surface phonon polaritons along the side surfaces of h-BN nanoparticles,[136] the investigated edge polaritons here are hybrid modes that are tightly bound to the edges of the material, rather than 2D surfaces.

Partial reflections of propagating modes at corners to adjacent side planes result in the formation of standing-wave patterns with a finite standing-wave ratio. This modulation of the photonic LDOS is visible in the EELS signal.[13,56] Fabry–Pérot-like resonances of several orders were observed along edges at distinct energy values, depending on their length (figure 3.4). From the distance between the maxima, the wavelengths and corresponding propagation constants of the excited modes were extracted, which show very good agreement with the

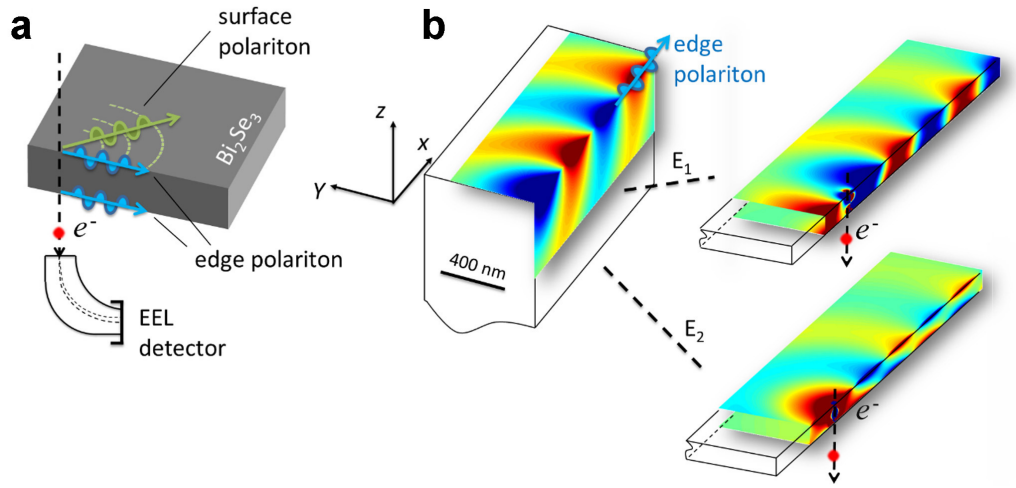

Fig. 3.3: (a) Excitation of polaritons in Bi_2Se_3 by an electron beam. During the inelastic interaction of fast electrons with the specimen, both surface polaritons and edge polaritons are excited and consequently the electrons experience energy loss. The electron energy-loss spectrum is then acquired by the energy-dispersive detection system. (b) Simulated z-component of the electric field associated with edge polaritons propagating along the edges of a Bi_2Se_3 large cube, at the energy of 4.0 eV. In thin films the edge modes are hybridized and form symmetric and antisymmetric modes, here at $E_1 = 4.3$ eV and $E_2 = 3.8$ eV for a thickness of 60 nm. Red and blue colors represent positive and negative values, respectively.

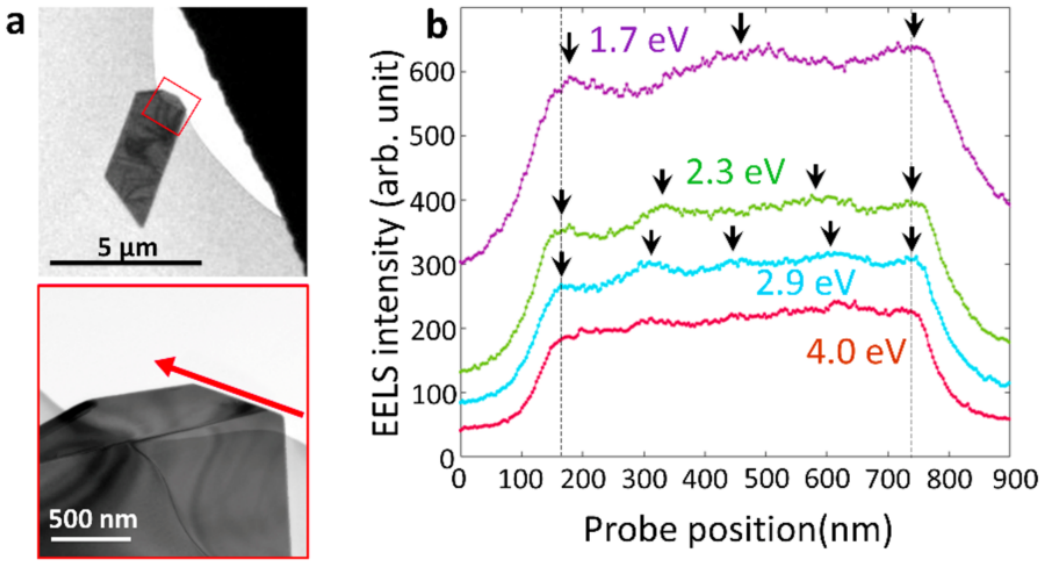

Fig. 3.4: (a) TEM images of a Bi_2Se_3 nanoplatelet at different magnifications and (b) EELS intensity acquired along its edge, as marked with a red arrow in (a). The intensity profiles were extracted from slices of an EFTEM series, which was acquired with a step width and energy-window of 200 meV. Spatial averaging was applied over 10 pixels as it is represented by the thickness of the red arrow in (a). Fabry-Pérot-like resonances are observed at specific energies, due to reflections from the corners. These resonances are used to calculate the effective wavelength and hence the phase constant of the excited mode.

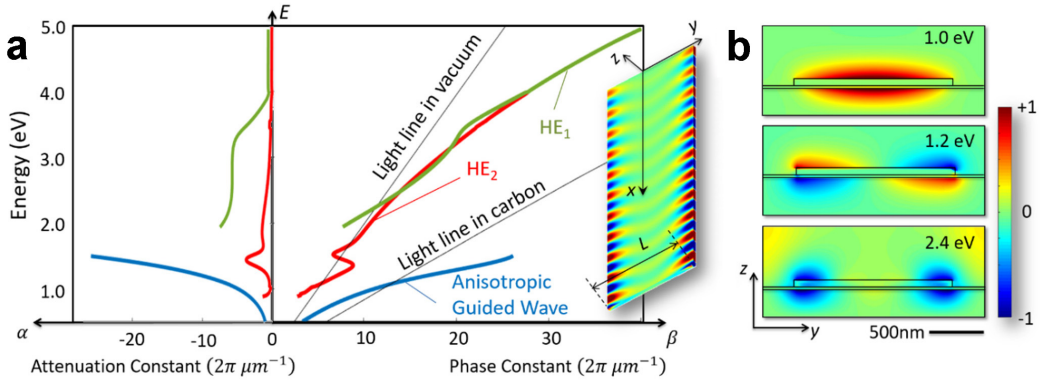

Fig. 3.5: (a) Dispersion diagram of the different optical modes, supported by a Bi_2Se_3 nanoplatelet in the form of a channel waveguide (only lower order modes are shown. HE_1 and HE_2 indicate hybrid magnetic-like modes. The inset graphic shows the simulated spatial distribution of the z-component of the electric field associated with the HE_1 mode, which propagates in the x-direction along an infinitely long waveguide. (b) The z-component of the electric field at the cross-sections associated with the anisotropic guided wave, hyperbolic type-1 HE_2 and hyperbolic type-2 HE_1 channel modes, are shown at the depicted energies from top to bottom, respectively.

computed dispersion (figure 3.5 a). For energies below 1.06 eV, channel modes are excited that have field profiles confined to the upper and lower surfaces. At higher energies, when the material becomes hyperbolic, HEEPs are excited with longer propagation lengths (inset of figure 3.5 a) and therefore reduced attenuation constants, particularly at energies above 3.0 eV.

Two coexisting HEEP modes with symmetric and antisymmetric field distributions are supported (3.5 b). Both modes are hybrid in nature, meaning that they have both electric and magnetic field components in the longitudinal direction and cannot be described by either transverse magnetic (TM) or transverse electric (TE) mode profiles, but rather a superposition of both solutions is required. Intriguingly, they can be described by HE mode profiles, which have

a dominating TE characteristic. HE_1 and HE_2 modes are associated with symmetric and antisymmetric HEEPs, respectively, where by symmetry, we refer to the spatial distribution of the induced charges.

3.1.4 Interaction with engineered defects

Launched optical modes that propagate along the edges of a nanoplatelet are partially reflected at corners, partially guided around them or couple to far-field radiation (figure 3.6 a). The realization of nanocircuitry devices for applications such as polaritonic cloaking[137] in the general field of transformational flat optics[138,139] requires tunable steering of the propagating modes to desired locations under the possible influence of interactions with local topological anomalies.

Here, we aim at understanding the interaction of HEEPs with such anomalies. For this purpose, different defect structures were created at clean edges of Bi_2Se_3 nanoplatelets using FIB milling. In the following, two examples are discussed, which are sketched in figure 3.6 a. The real structures are located on two different nanoplatelets, as displayed in SEM images in figure 3.6 b. Binary images have been extracted as a topological basis for FDTD simulations.

Finite grating structure The structure with round-shaped grooves (figure 3.6 b, left panel) was experimentally analyzed by EFTEM, which yields better spatial sampling over this large investigated area and reduces the risk of contamination and beam damage compared to scanning the ROI with a focused electron beam. While there is no spatial intensity modulation present at 1.0 eV, a high intensity is observed along the structured side planes with

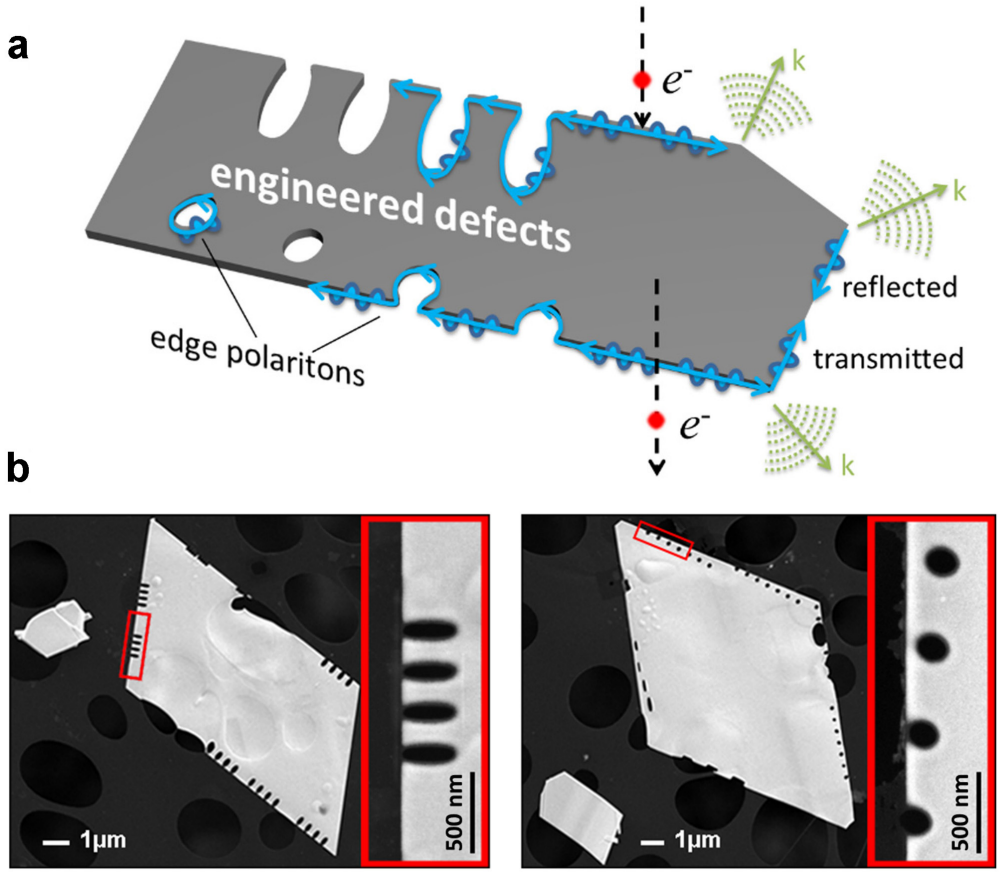

Fig. 3.6: (a) The interaction of HEEPs at corners and with precisely engineered scatterers of different topology causes reflection, transmission and radiation of partial waves. (b) SEM images of the investigated structures "finite grating structure" and "circular nanocavities", that are located on two different nanoplatelets.

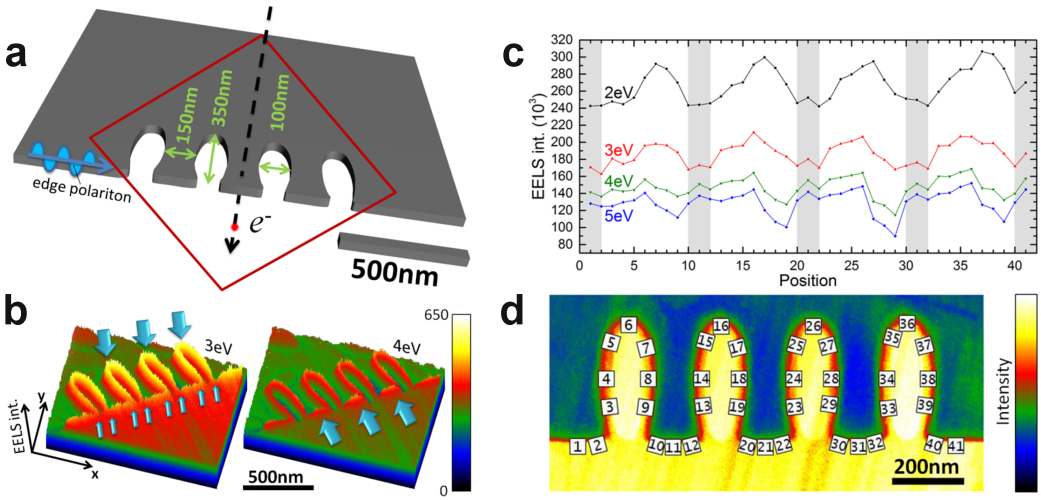

Fig. 3.7: (a) Schematic of the finite grating structure, consisting of round-shaped grooves. The investigated area is marked by a red frame. (b) EFTEM images at different energy-losses (3.0 eV and 4.0 eV) acquired with an energy window of 0.2 eV width. The intensity variation indicates the relative local absorption probability. Big and small blue arrows point towards intensity maxima and minima, respectively. (c) Intensity modulation along the structured edge for different energy-loss values. The analyzed spectra were extracted from positions marked in (d) and averaged spatially over an area of 10 by 10 pixels. Grey shaded areas in (c) emphasize the positions of the bridges between grooves.

maxima inside the grooves and minima at the corners at 3.0 eV, which are marked with big and small blue arrows in the EFTEM image (figure 3.7 b, left panel). These intensity modulations are caused by the interaction of HE_1 and HE_2 modes with discontinuities like sharp corners and partial reflections from them. Missing intensity modulations at 1.0 eV is understood from the fact that at this energy, the dispersion of the HEEPs is located inside the light cone (figure 3.5 a); therefore, electron-induced excitations strongly couple to radiation. The perimeter of each groove structure is approximately 700 nm, that is equal to $2\,\lambda_{\text{eff}}$ at this energy, where $\lambda_{\text{eff}} = 2\pi/\beta\,(\omega)$ is the effective HEEP wavelength and $\beta\,(\omega)$ the phase constant. Interestingly, despite the relatively large size of the groove, only one single maximum is observed. We associate this behavior to the coexistence of two HE_1 and HE_2 modes at this energy with slightly different propagation constants, in such a way that interference between these two optical modes leads to a beating frequency observed as a low-frequency spatial modulation. At 4.0 eV, absorption maxima are measured at the narrow bridges between the grooves (big blue arrows in figure 3.7 b, right panel). At this energy, HE_1 and HE_2 modes become degenerate and the effective wavelength associated with both modes is approximately 350 nm, that is two times the length of the narrow bridges. At energies higher than 4.0 eV, the EELS signal for electrons traversing the Bi_2Se_3 film becomes more prominent, highlighting the existence of surface plasmons (SPs).

Additional measurements were performed on a second finite grating structure, with grooves separated by 300 nm gaps from the edge, (figure 3.8). EELS data were acquired in STEM mode in an aloof configuration, where the electron probe is positioned in close vicinity to the specimen. Indeed, in a modal description, electron beams can couple both to the surface and edge polaritons. In addition, also scattering of surface waves at the edges excites polaritons

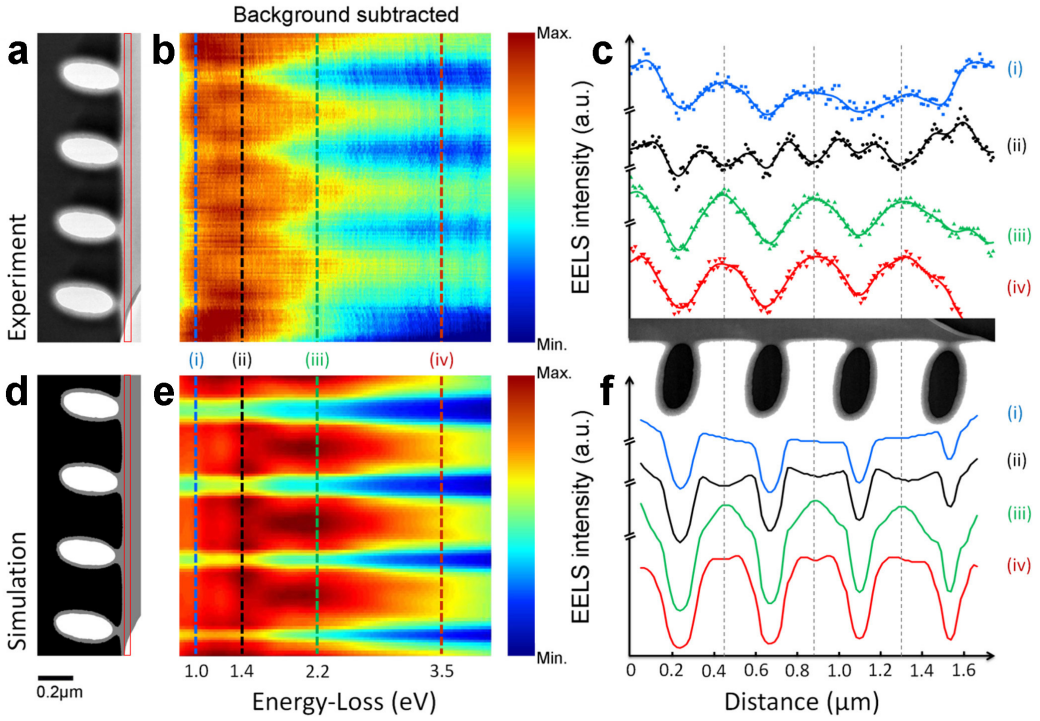

Fig. 3.8: (a) Bright-field (BF) TEM image of the nanostructure. It is composed of an edge with elliptical grooves. The form of the boundaries was extracted as a binary image (d) and used for simulations. (b,e) Experimental and simulated energy-distance maps, showing absorption probabilities depending on the energy-loss value and probe position, were extracted from the area marked with red boxes in the survey images. (c,f) Line profiles at selected energies (1.0 eV blue, 1.4 eV black, 2.2 eV green, 3.5 eV red) are shifted vertically for clarity. The experimental profiles (c) were processed by applying a Fourier transform smoothing algorithm in the plotting software, using a 5-point window (solid lines).

propagating along the edges. In an aloof experiment, like the EELS scan data in figure 3.8, electrons can only couple to edge polaritons. A spectral line scan along the structured edge was obtained from a spectrum image by averaging over four pixel rows to increase the SNR. Subtracting a first-order log-polynomial background, fitted to the tail of the monochromated ZLP within the DM software, resulted in the EELS intensity distribution of figure 3.8 b,c. The color-coded absorption probabilities versus the probe position show intensity maxima at 1.0 eV and 2.2 eV at the centers and at 1.4 eV at the corners of the bridges. The spatial modulation of distinct energy-loss values along the edge was extracted as line profiles (figure 3.8 c) that are in good agreement with the simulations (figure 3.8 f). For the simulations, we have directly used the TEM dark-field (DF) image to extract the structural topology with high accuracy (figure 3.8 d). Additionally, at energy-loss ranges $\Delta E < 1.0\,\mathrm{eV}$ and $1.1\,\mathrm{eV} < \Delta E < 1.7\,\mathrm{eV}$, we observe the first-order and second-order Fabry–Pérot-like resonances with one and two intensity maxima along the bridges, respectively (figure 3.8 b,c and e,f for experimental data and simulations). At energies $1.7\,\mathrm{eV} < \Delta E < 2.2\,\mathrm{eV}$, however, we observe again a first-order mode. This is particularly due to the change in the material dispersion from HB_1 to HB_2 and also corresponding changes in the phase constant and effective wavelength of the hyperbolic polaritons.

Circular nanocavities To investigate the propagation around defects in detail, open and closed circular nanocavity structures were created at the edges of nanoplatelets to study the interference of localized polaritons with propagating modes. Holes with a diameter of 200 nm and a side-to-side distance of 350 nm were milled at different distances from the edge, resulting in two open cavities with opening gaps of 150 nm and 100 nm and edge distances of 50 nm, 100 nm

and 150 nm. A 3D sketch of the structure is shown in figure 3.9 a. The red frame marks the area containing the first three holes, which has been investigated via STEM-EELS spectral imaging, where the electron probe is scanned over the specimen, while detecting a complete electron energy-loss spectrum for each pixel. Color-coded energy-filtered images have been extracted from the 3D data cube at selected energy-loss values in the range between 1 eV and 4 eV. As for the finite grating of the grooves discussed before, the measured EELS signal is mainly confined to the shaped edge of the nanoplatelet and the intensity exhibits maxima within the holes and minima at the corners. Interestingly, this is also the case for the isolated hole, which is located at a distance of 50 nm away from the edge. As discussed before, Fabry–Pérot-like resonances that occur at finite edges are detectable via spatial intensity modulations in the EELS signal. This intensity modulation is observed along the edge between the two open holes with a maximum in the center for 1.0 eV, two maxima at the corners for 1.5 eV and three maxima (one in the center and two at the corners) for 2.0 eV. Interestingly, the same modulations, though with less visibility, are detected along the edge between the second and the third hole, which clearly reveals an influence of the latter isolated resonator on the propagating edge polaritons.

Simulated spectral line scans confirm these experimental findings (figure 3.9 b–e). Nevertheless, the contrast of the EELS signal along the edge relative to the signal from the open cavities is more pronounced in the FDTD simulations. At higher energies, this contrast is significantly altered, which is due to an enhanced coupling between the edge polaritons and localized SPs within the nanocavities, as will be discussed later. Moreover, at energies above 4 eV, there is no significant intensity modulation observable along the edges at the location of the 3$^{\text{rd}}$ and 4$^{\text{th}}$ isolated nanocavity. Nevertheless, even at energies below 4 eV,

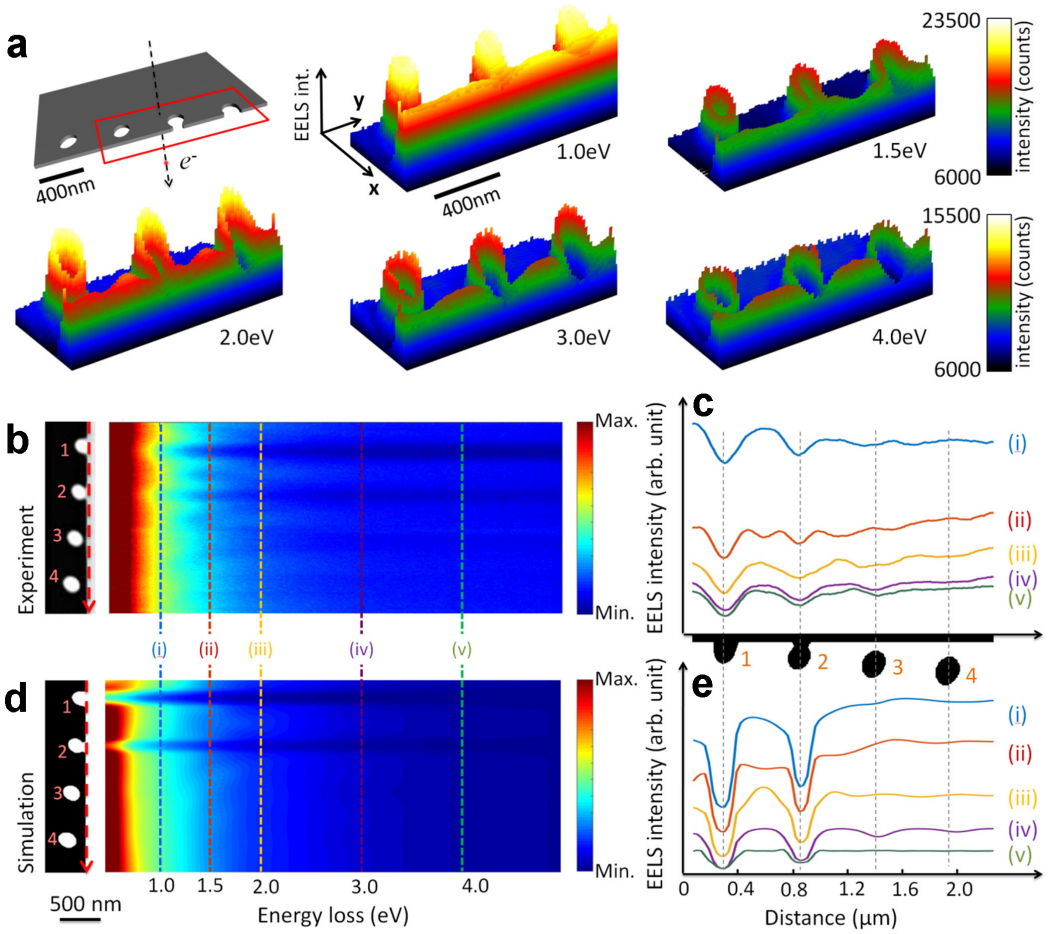

Fig. 3.9: (a) Schematic of the defect structure with the investigated area being marked by a red frame and slices of the 3D data cube at the indicated energy-loss values (1.0 eV, 1.5 eV, 3.0 eV and 4.0 eV). The color scale indicates the relative local absorption probability for the displayed energy-loss. (b,c) Experimental and (d,e) simulated EELS intensities acquired along a Bi_2Se_3 nanoplatelet having holes at different distances from the edge. The exact shape of the structure was extracted from the BF TEM image and used for the simulations. Line profiles at selected energies (i) 1.0 eV, (ii) 1.5 eV, (iii) 2.0 eV (iv) 3.0 eV and (v) 4.0 eV are shown in (c) and (e).

the influence of the third hole on the intensity modulations is more pronouncedly observed in the experimental results when compared to the simulations. This discrepancy can have several reasons: (i) Due to the weak VDW forces between layers, the material forms a layered structure; therefore, reaching a perfectly aligned edge by milling is not possible. However in simulations, a vertical hole configuration is assumed. (ii) In contrast to the experimental results, simulations show more pronounced influences of the first and second nanocavity. This results in more contrast in the intensity and as such, the rather faint effect of the first and second hole is not as pronouncedly observed as in the experiment. (iii) The exact topology of the holes, formed by ion milling, is not cylindrical with vertical walls as considered in the simulations, but rather has some small inclined angles leading to a truncated conical topology, which has not been considered in the simulations. Additionally, other reasons might also slightly alter the simulation results compared to the experiments, such as the existence of pollutant and dopants inside the material that could slightly change its optical response compared to the expected perfect Bi_2Se_3 single-crystalline structure.

Discussion Fast electrons interact with uniaxial crystals of Bi_2Se_3, resulting in a variety of collective modes being excited within the bulk, at the interfaces and along the edges of the nanoplatelets. Because of electromagnetic interactions between the electrons and launched polaritons, the electrons lose energy, which is detected by an electron energy-loss spectrometer. Electrons propagating in the bulk along the z-axis launch longitudinally oscillating charge density waves, resulting in an absorption peak at the bulk plasmon energy of 2 eV, as well as Cherenkov radiation at energies below 1 eV, where the material is still dielectric. At the interfaces to a dielectric medium, surface modes, ranging

from channel waveguide waves[140] in the dielectric to hyperbolic polaritons[112] in the hyperbolic energy regime, transfer electromagnetic energy in lateral directions. Within the context of SPPs, the hybridized even and odd modes of thin metallic films are well known and extensively discussed in the literature.

The dynamics of edge polaritons and the phase distribution of optical near fields could convey more insight into the time-varying propagation mechanisms to understand for instance the multipole distributions of localized resonances in our cavities. In contrast to EELS experiments that show time-averaged photonic LDOS, simulations using the FDTD approach are a powerful tool to give insight into the dynamics and propagation mechanism of the polaritons and their interactions with structured defects. By exciting the specimen at certain energies with an electron at a defined impact position (marked with a white dot in figure 3.10), the propagating modes can be visualized by calculating the z-component of the electric and magnetic field strength in finite time intervals. When the moving electron interacts with the Bi_2Se_3 nanoplatelet at its edge, various energy-loss channels become possible, ranging from diffraction radiation to surface and edge polariton excitations. The dominant mechanism is the transition radiation, whereas only less than 10 % of the generated photons are converted to the propagating polaritons.

We start our analysis with the structure shown in figure 3.7. While propagating modes are observed along the edges of the grooves for higher energies, this is not the case at 1 eV. Instead, dipolar excitations are visible inside defects that couple to the edge polaritons. The magnetic field is confined inside the defect with asymmetric orientation related to the position of the excitation, pointing inside and outside the plane, respectively (figure 3.10 a, right panel). As such, the defect structure behaves similarly to a split ring resonator at low energies. Hence, the mechanism of the propagation of the polaritons at

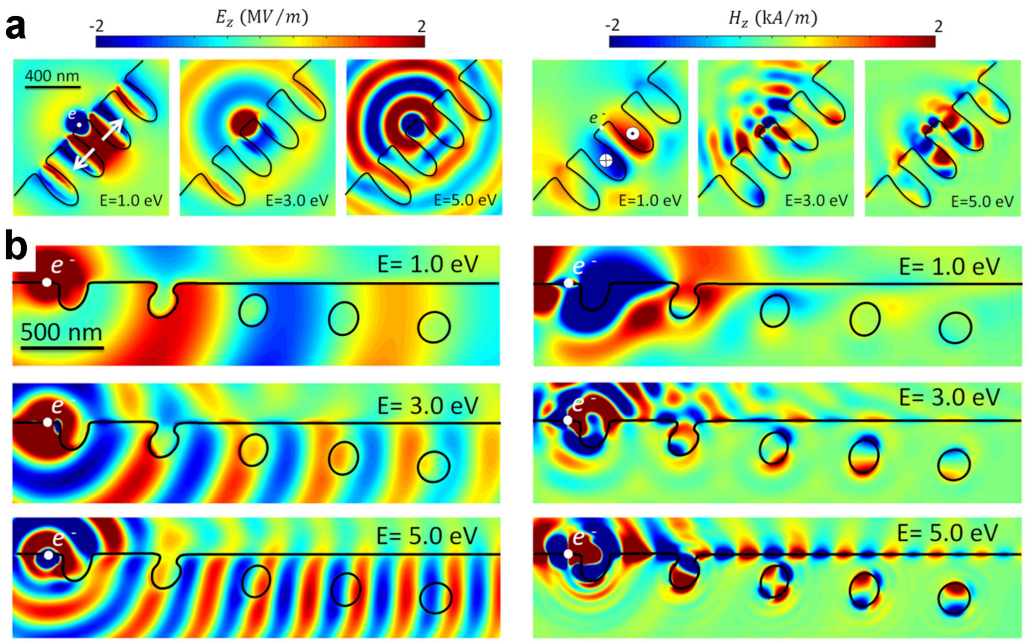

Fig. 3.10: FDTD simulations for the investigated "finite grating structure" (a) and structure with "circular nanocavities" (b) being excited by fast electrons at the positions marked in white color. The color-coded images show the z-component of the electric (left panels) and magnetic (right panels) field strength for different excitation energies. The images depict temporal snapshots. Movies are available online.[2]

this energy is via dipole-dipole interactions. At energies higher than 3 eV, the effective wavelengths of the edge polaritons are smaller than the size of the grooves. Edge polaritons are therefore partially transmitted around the corners into the grooves and are partially coupled to the next defect via radiation transfer. However, the latter mechanism contributes more strongly to the coupling between the defects at higher energies. Particularly at energies greater than 4 eV, edge polaritons can penetrate into the grooves around bending edges as sharp as 90° and couple to the next gap as well.

For the structure with embedded circular nanocavities at varying distances from

the edge, we observe the surprising ability of the edge polaritons to cope with the presence of smaller defects. Even for the case of open nanocavities touching the edge, edge polaritons can efficiently couple to the next bridge at low-loss. At energies greater than 4 eV, the attenuation constant of the HE_1 edge mode is significantly reduced (compare figure 3.10 b with figure 3.5 a). Hyperbolic SPPs are purely transverse modes and do not sustain the z-component of the magnetic field (H_z). In contrast, edge polaritons demonstrate a strong localization along the edges (figure 3.10 b, right panels). Edge polaritons can also be localized inside isolated nanocavities in the form of dipolar and quadrupolar magnetic resonances, at the energies of 3 eV and 5 eV, respectively. In comparison with SPPs, the spatial distribution of edge polaritons is quite confined to the edges, which makes them suitable candidates for engineering localized nanoresonators made of Bi_2Se_3.

3.1.5 Conclusions

Our overall observations highlight unique features of optical excitations in tetradymites and in particular in Bi_2Se_3. Distinct from surface and edge plasmon polaritons, the visibility of the spatial interference fringes caused by the Fabry–Pérot-like resonances in Bi_2Se_3 nanoplatelets are much less pronounced. As discussed here, this is due to the coexistence of various optical modes and therefore low beating frequencies caused by the phase differences between the optical modes. Moreover, exactly this competition between the different optical modes helps for a higher transmission through discontinuities, simply by facilitating the modes couplings and various energy transfer mechanisms as discussed above. Moreover, we do not observe a zigzag-like propagation of the sort normally observed in h-BN and other materials supporting phonon

polaritons. In other words, the optical response of Bi_2Se_3 sustains a combination of plasmonic-like propagation concomitant by a large number of photonic states, supported along surfaces, edges, as well as in the bulk of the material.

Finally, we would like to point out that our observations regarding the behavior of edge polaritons support the ellipsometry model used in treating the material as a uniaxial anisotropic material, in a sense that the in-plane dispersion of the optical waves is completely isotropic. We did not observe any evidence that the behavior of edge polaritons along certain in-plane edges, regarding their orientation with respect to the in-plane crystallographic direction, is different. However, natural nanoplatelets do behave differently from long milled edges, highlighting the fact that due to the layered nature of the material, milling the structure to achieve a perpendicularly aligned edge is challenging.

Our results show that Bi_2Se_3 can host room-temperature polaritons, similar to other classes of VDW materials such as transition metal dichalcogenides. The excitonic optical response of Bi_2Se_3, in combination with its hyperbolic behavior, allows for the excitation of HEEPs. Their interaction with engineered defects of different topologies is revealed here in detail. We were able to directly visualize standing-wave patterns resulting from the reflection of hyperbolic polaritons from edges and corners and furthermore to experimentally demonstrate steering of the edge polaritons by means of grooves and nanocavities in the vicinity of edges. Supported by numerical simulations, we could show that at higher energies, edge polaritons can avoid defects and that unexpectedly the standing-wave ratio associated with the reflection from such defects is smaller than at lower energies. Remarkably, due to the large number of hybrid optical modes, which are excited at higher energies and also the low attenuation constant of edge polaritons excited above 4 eV, embedded discontinuities are overcome by coupling between various edge and radiation modes. This characteristic is

promising for the implementation of data transmission lines as interconnects between electronic counterparts and opens up possibilities for coherent and efficient transfer of optical energy similar to topological photonics, albeit within a natural material such as Bi_2Se_3. Moreover, the principal possibility to tune hyperbolic polaritons in vdW materials via doping and defect engineering renders Bi_2Se_3 and related tetradymites into promising platforms for future configurable optical waveguides, both in the reststrahlen bands as discussed elsewhere[136,141] and at visible frequencies as demonstrated here. Our concept provides an excellent basis for future applications such as nanooptical circuitry, cloaking at the nanometer scale, as well as quantum technology by steering emission of quantum emitters on the nanoscale.

Contributions to this project The underlying research article to this section was written by Robin Lingstädt together with Nahid Talebi, who performed the theoretical and numerical investigations and supervised the entire work together with Marko Burghard, Harald Giessen and Peter A. van Aken. Optical ellipsometry measurements were carried out by Bruno Gompf. Nanoplatelets were grown by Soudabeh Mashhadi, who also performed AFM measurements of the defect structures that were created by Mario Hentschel. Robin Lingstädt prepared the samples for TEM investigations and performed the EELS and CL measurements.

3.2 Plasmonic excitation and far-field radiation of gold tapers

In the field of nanophotonics, metallic nanostructures are well-known functional elements. In such structures, SPs can strongly interact with photons and therefore propagate and transport electromagnetic energy on the nanoscale, reaching confinements even substantially below the diffraction limit.[142–146] In the case of surface plasmon,[147–149] channel plasmon[150] and wedge plasmon[151,152] polaritons, long-range propagation has been found in planar geometries.[153]

One of the most established and widely used 3D nanostructures are conically shaped metallic tapers, as their plasmonic properties show interesting characteristics in strong correlation with their geometrical properties and favourable resonance behavior can be tailored by optimizing structural parameters like surface roughness or opening angle. Their practical application ranges from waveguides or nanoantennas in scanning near-field optical microscopy (SNOM)[154–163] to ultra-fast photoemission sources in point-projection microscopes.[164–173]

To investigate the underlying physical principles of these technologically important nanophotonic devices, several characterization techniques and numerical simulation methods have been employed to further understand excitation and propagation processes and the mechanism of focusing electromagnetic energy to the nanoscale.[65,154,159,166,174–177]

Interestingly, for mesoscopic rather than nanoscopic specimen dimensions, as will be discussed here, a dynamic exchange of momentum and energy is observed along the electron trajectory. Theoretical investigations revealed that the fundamental TM SPP mode with vanishing angular momentum $m = 0$ is able

to propagate along the taper shaft and concentrate the carried electromagnetic energy at the apex, while its radially symmetric electric field is evanescently bound to the surface.[155,174,178] This coupling to localized plasmons at the tip is termed as adiabatic nanofocusing.[65,143,154] By contrast, other plasmon modes with higher angular momentum order $|m| > 0$ do only propagate above certain critical radii (i.e. the local radius of the cross section normal to the taper axis), where they radiate off the taper and couple to the far-field.[174,176,177,179] For realistic taper geometries with a limited radius of curvature at the apex, both reflection and radiation of the $m = 0$ mode have been observed.[164,167] In general, the behavior of the different plasmonic modes, sustained by metallic tapers, is strongly affected by varying parameters like apex curvature, opening angle or surface quality, which was addressed by recent studies.[70,167,176,180,181]

3.2.1 Back-reflection and phase-matching mechanism

3D single-crystalline gold tapers with different opening angles were investigated experimentally by both EELS and CL, supported by numerical calculations. The proposed theoretical model reveals a dynamic interplay of the plasmonic modes with the exciting swift electron, which results in the observed interference pattern in the EELS signal. In general, two coexisting mechanisms are identified, that are more or less dominant, depending on the taper geometry. While the reflection of plasmonic modes from the apex plays the major role for tapers with small opening angles (below 10°), the phase-matching between the electric fields of plasmonic modes with higher-order angular momentum and the passing electron becomes dominant for large opening angles (above 20°), due to the longer interaction time.

Single-crystalline gold tapers[65,66] with a particularly smooth surface were used

for the experiments in order to minimize scattering losses and localization of SPPs.[182] EELS measurements were performed at an acceleration voltage of 200 kV with the ZEISS SESAM (see section 2.2.1 on page 32 for details). The spatially resolved intensity variations reveal resonance effects and give insight into the strong dependence of plasmonic modes on taper geometries. For gold, however, this spatial information is limited to energies below 2 eV, where interband absorptions set in and result in a homogeneous EELS intensity distribution.[60,183] Detecting the energy-loss spectrum continuously while scanning the electron probe over a certain distance L along the taper shaft results in an energy-distance map (figure 3.11 b). A very intense signal is detected at the apex, which is associated with highly confined localized SPs. Its spectral intensity is almost constant over a wide energy range, in contrast to results of earlier work on metallic nanoparticles and conical tapers, where this broadband characteristic has not been observed.[184]

Moving the electron probe further away from the apex, distinct maxima are observed in the spectra below 2 eV that shift towards lower energies. These resonances are related to higher-order angular momentum taper eigenmodes, as will be discussed below. The individual modes can be identified by tracing maxima in the spectra over L and fitting the data with hyperbolic functions $E = E_0 + \kappa/L$, with E_0 and κ being constants (figure 3.11 c). Moreover, the fitting parameters were found to linearly depend on the mode number m, resulting in the empirical relation

$$E = (0.105\,m - 0.098)\,\mathrm{eV} + \frac{(0.105\,m - 0.098)}{R}\,\mu\mathrm{m\,eV}, \tag{3.2}$$

with $R = L \cdot \sin(\alpha/2)$ as the local radius at a certain distance from the apex of a taper with the opening angle α. Numerical calculations revealed that the

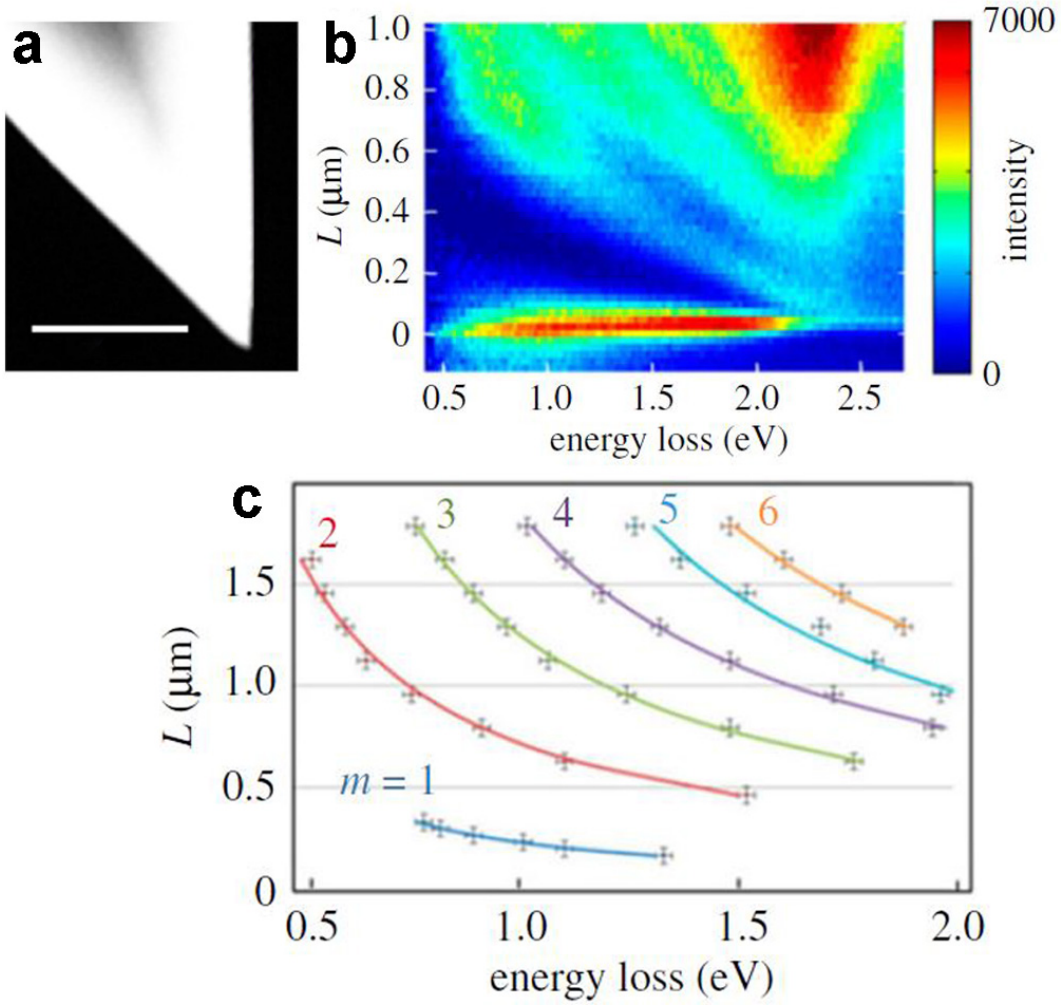

Fig. 3.11: (a) HAADF image of a taper with an opening angle of 49°. The scale bar is 500 nm. (b) Local EELS measurements along the taper shaft. The energy-distance map shows the EELS intensity over the scanning distance L. A very intense broadband signal is detected at the taper apex and higher-order angular momentum eigenmodes become apparent. (c) Taper eigenmodes with higher-order angular momentum numbers $m = 1, ..., 6$ are identified by least-squares fits of hyperbolic functions to the maxima in the energy-loss spectra and traced over the scanning distance L. Adapted and reused with permission from the original publication.[176]

observed resonances can be attributed to a phase-matching mechanism between the electric fields of taper modes and the exciting electron and will be discussed in the following.

Aiming for a more fundamental level of understanding the physical principles behind these experimental observations, conical structures have been extensively studied theoretically in the past. Although rather complex mathematical methods and novel approximation schemes have been applied, the determination of explicit solutions is still a matter of ongoing research.[185–187] Following the comparably intuitive approach of viewing the taper as a combination of infinitely thin slices of metallic fibers with continuously varying radii, the near-field properties of a conical structure can be effectively modelled by a superposition of fiber eigenmodes.[176] After solving the Helmholtz equation in cylindrical coordinates, they can be characterized by the complex wavenumber k_z along the fiber axis and the azimuthal angular momentum number $m = 0, \pm 1, \pm 2, \ldots$.[188,189] Interestingly, higher-order modes can only propagate evanescently bound to the metallic surface above a certain mode-dependent critical local radius, where they radiate off the taper and couple to the continuum of photonic modes. By contrast, it is only the rotationally symmetric $m = 0$ mode that is not restricted in this regard. This lowest-order angular momentum mode is therefore able to transport electromagnetic energy to the apex and focus it adiabatically.[143,190–192]

The conducted experiments were evaluated theoretically by FDTD simulations. The ability to calculate electric field distributions and their evolution with high temporal resolution gives insight into the very fast interaction processes of the passing electron with the investigated structure. Of course, it is essential to model the entire experimental setup very accurately, including the 3D taper itself and the relativistic electron source.[41,193] The results of a dynamic simu-

lation for a gold taper with an opening angle of $\alpha = 45°$ in the aforementioned local radius approximation are shown in figure 3.12 a,b. The structure is excited by a fast-moving electron, which passes the surface at a minimum distance of 1 nm. Its speed is set to roughly 70 % of the speed of light, which corresponds to an acceleration voltage of 200 kV in an electron microscope. A detailed analysis of the temporal and spatial evolution of the fields revealed that most of the transferred energy is radiated in the form of an ultra-short light pulse, whereas only a minor amount couples to evanescent surface modes. Although initially a wave packet with a broad energy distribution and wide range of mode numbers m and wavenumbers k_z is launched, only modes up to a certain mode order m can propagate towards the apex due to the limiting local radius at the impact position. Energy-loss spectra were simulated for infinitely long fibers with varying radii (figure 3.13 c,d,e). The calculated results clearly reveal a resonance characteristic in good agreement with the experimental findings (figure 3.11). The observed hyperbolic dispersion of energy-loss maxima depending on the local radius were analysed carefully with regard to the underlying model of infinitely long fibers.[176] The development of an analytical description revealed two different mechanisms as reasons for EELS resonances. Firstly, absorption maxima are expected, whenever the spatial profile of the scattered field of an excited fiber matches closely with the field of one of its eigenmodes that propagate along the taper (or fiber) axis.[188,189] Secondly, by evaluating overlap integrals along the electron trajectory, it was shown that the spatial phase pattern of the passing electron can resemble one of the rotating eigenmodes with higher angular momentum orders for certain energies. Whenever this phase-matching occurs, energy is resonantly transferred from the electron to the structure and an absorption maximum is observed in the energy-loss spectrum. This case is exemplarily shown for an assumed frequency $\omega = 1.6\,\mathrm{eV}\,\hbar^{-1}$, for which the electron field oscillates along its trajectory with a wavelength of 539 nm

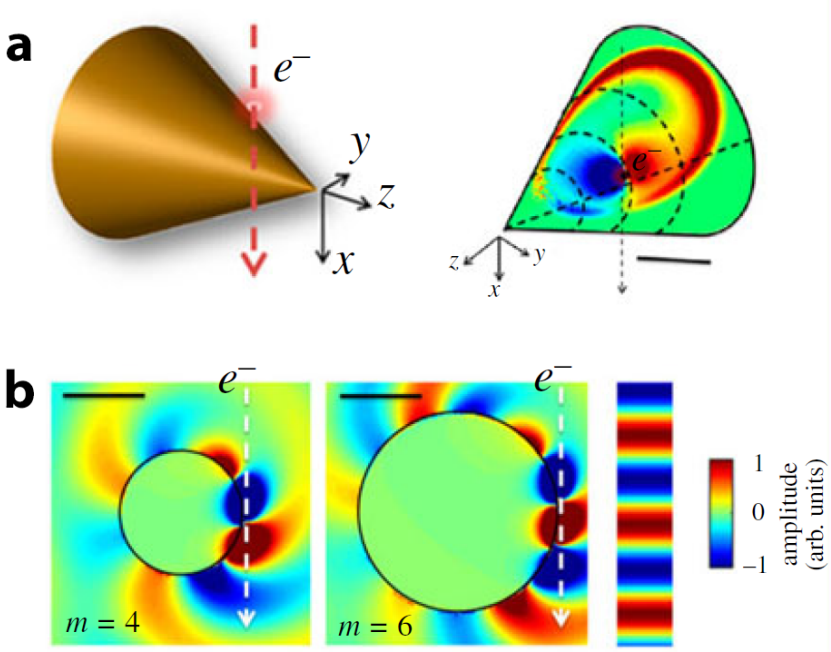

Fig. 3.12: (a) 3D sketch (left panel) and dynamic simulation for a taper with an opening angle of 45° (right panel), showing the E_z-field on its surface, while an electron passes the structure 900 nm away from the apex. The color code maps the field distribution 1 fs before the electron reaches its closest distance of 1 nm from the surface. (b) Scattered electric field component E_z, calculated for an energy-loss of 1.6 eV, induced by an electron that passes the taper at the local radii of 383 nm (left panel) and 612 nm (centre panel). The plane-wave component of the electric field, corresponding to the moving electron, is displayed on the right. Scale bars are 500 nm. Adapted and reused with permission from the original publication.[176]

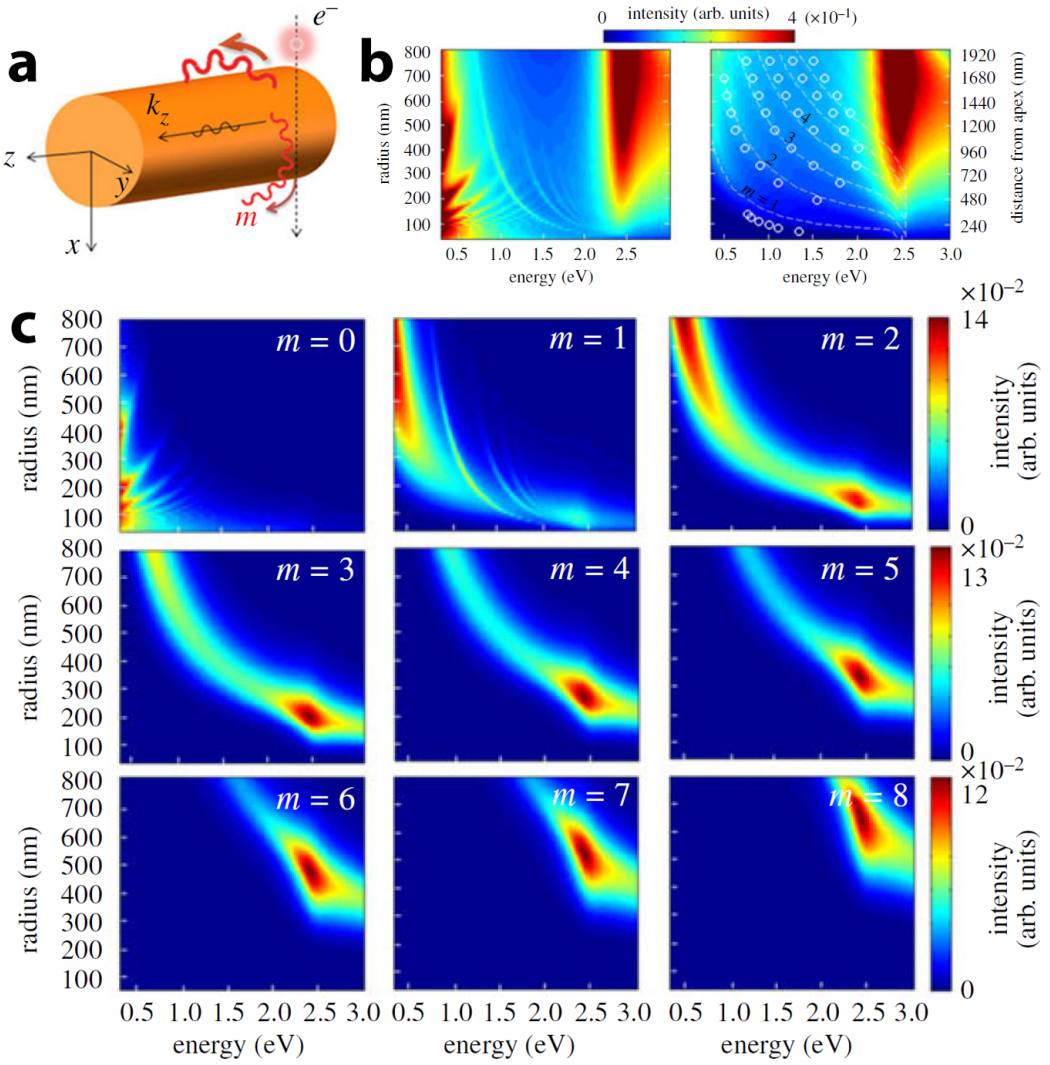

Fig. 3.13: (a) A fast electron passes an infinitely long metallic fiber at a close distance. Due to the interaction, evanescent SPP modes are excited that propagate along the fiber (k_z), as well as radiative modes with different angular momentum numbers m. (b) Energy-loss spectra simulated for different fiber radii including (left panel) and excluding (right panel) modes with $k_z > k_0$ for an electron that passes at a distance of 1 nm from the surface. Experimentally determined values (circles), measured along a taper with an opening angle of 49°, resemble the theoretically predicted EELS maxima very well (dashed lines). (c) Simulated contribution of the individual modes with angular momentum numbers $m = 0, ..., 8$. Adapted and reused with permission from the original publication.[176]

(figure 3.12 b). Fourier transformations of the FDTD simulations revealed a strongly scattered field for that particular frequency only, if the electron passes the taper at specific local radii. In addition, the field distributions closely resemble the field pattern of the fiber eigenmodes with $m = 4$ and $m = 6$, respectively. A rather rough approximation can be made by evaluating the aforementioned overlap integral only over a reduced interaction length, as the interaction is the strongest close to the surface. Phase-matching resonances are observed whenever the phase of the electron field matches with the phase of a fiber mode field over the interaction length. The obtained hyperbolic dependence of resonance energies on local radii $\hbar\omega \approx (m \pm 1)\,\hbar v_{el}/R$, where v_{el} is the electron velocity, resembles the empirically determined dispersion relation (equation 3.2) qualitatively quite well.

In addition to the EELS experiments, where the absorption probability is dispersed into energy spectra, the theoretical model allows for further analysis regarding the decomposition versus longitudinal and angular momenta along and around the fiber axis, respectively. The calculations show that for comparably thin fibers ($R = 50\,\mathrm{nm}$) the rotationally symmetric $m = 0$ eigenmode most dominantly contributes to the EELS signal and phase-matching resonances are not relevant. For larger radii, however, the situation is completely different. Due to the increased interaction length along the electron trajectory, the EELS signal is most strongly influenced by the phase-matching mechanism rather than the excitation of fiber eigenmodes. As it was shown for the fiber radius $R = 400\,\mathrm{nm}$, resonance energies, surprisingly, correspond to highly radiative modes with $k_z < k_0$, where $k_0 = E/\hbar c$ is the wavenumber of light in vacuum. For the interpretation of EELS data of conical tapers and finite structures in general, with dimensions that exceed multiples of the electron field oscillation wavelength along its trajectory, the phase-matching mechanism definitely has

to be taken into account. It should be noted, however, that the results depend on the electron velocity and that standing-wave patterns may arise due to the reflection of the propagating fundamental mode at the apex, especially for tapers with narrow opening angles.[167]

Analytical models for conical metal tapers confirmed the coexistence of the two mentioned mechanisms and their effect on the EELS signal.[177] To investigate their origin further, single-crystalline gold tapers with various opening angles ranging from 5° to 47° were studied both experimentally by EELS and theoretically by FDTD simulations.[69] The simulated results for the two extreme geometries 5° and 30° are shown in figure 3.14 a and b, respectively. The structures were excited by relativistic electrons with a kinetic energy of 200 keV that pass the tapers at a distance of $L = 1460\,\mathrm{nm}$ from the apex. In the chosen orientation of the coordinate system, the x-component of the scattered electric field exclusively contributes to the EELS signal, as it is oriented parallel to the electron trajectory. Its value is plotted on a logarithmic scale in dependence of the x-position along the electron trajectory and the evolved time. The time dependence of the reemitted fields of both structures shows similarities on the one hand, but also fundamentally different characteristics. In both cases, plasmonic modes with higher-order angular momentum are excited that result in the formation of a complex interference pattern. In addition, they radiate off the taper and launch electromagnetic fields that propagate through free space at the speed of light (yellow dashed lines in figure 3.14 a,b). For the narrow taper with an opening angle of 5°, only the fundamental mode with $m = 0$ is evanescently bound to the surface and can propagate to the apex, where it is partly reflected and results in an evanescent field burst, that arrives at the excitation location with a time delay of approximately 11 fs (figure 3.14 a).[194] At the position where the electron comes closest to the

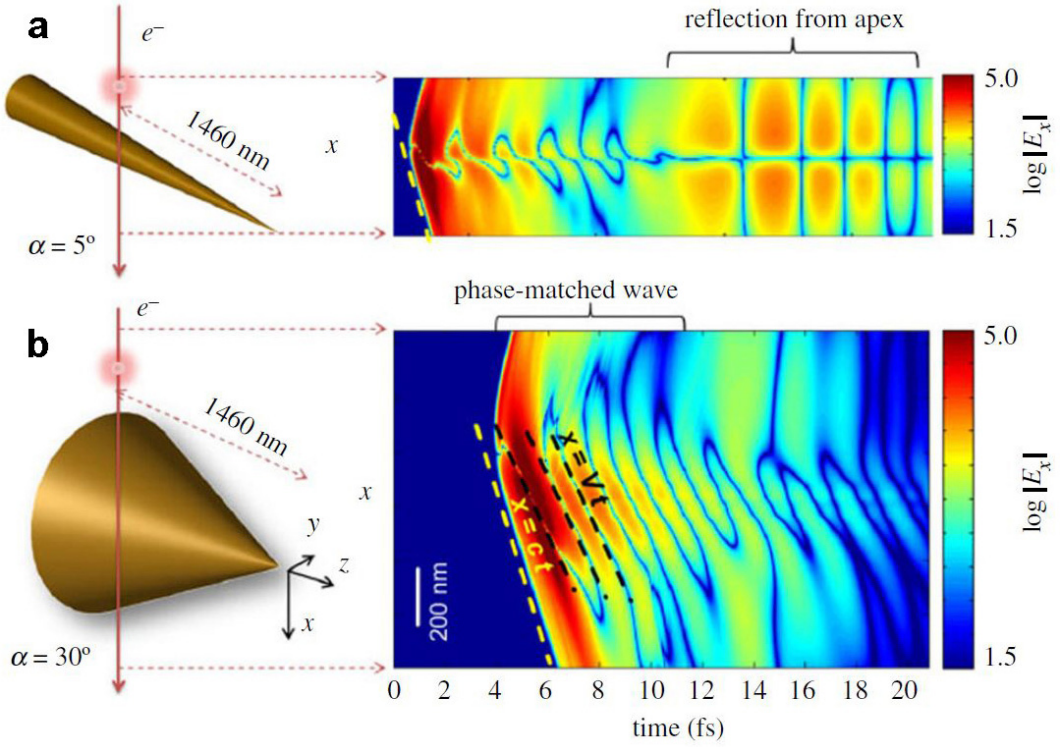

Fig. 3.14: FDTD simulations for gold tapers with 5° (a) and 30° (b) opening angles that are excited by a fast electron at a position 1460 nm away from the apex. The scattered electric field, projected along the electron trajectory $|E_x|$, is plotted against the x-position and time on a logarithmic scale. Plasmon oscillations lead to the emission of electric fields that propagate away from the structure at the speed of light (yellow dashed line). In addition, higher-order angular momentum modes result in a complex interference pattern. A clear time-delayed signature of the fundamental mode, being reflected at the apex, is observed for the taper with 5° opening angle (a). For the taper with large opening angle (b), also modes with higher-order angular momentum ($m = 1$ and $m = 2$) can propagate along the shaft. They are evanescently bound to the surface as a SPP wave packet, with spatio-temporal dynamics that depend on the electron velocity (black dashed line). Adapted and reused with permission from the original publication.[69]

surface, both longitudinal and radial components of the propagating mode vanish when projected onto the electron trajectory, resulting in a centred line of zero intensity. For the taper with 30° opening angle, also higher-order modes are evanescently bound and can propagate away from the impact position. As a result, their propagation occurs in the form of a wave packet. Due to the increased interaction length with the electron along its trajectory for larger local radii, the resulting interference pattern is inclined by a different angle (black dashed line in figure 3.14 b), which in turn depends on the electron velocity.

The gradual transition from phase-matching-dominated resonances to a reflection-based origin can be illustrated in a simplified picture, as tapered structures more and more resemble a semi-infinite whisker by decreasing the opening angle. For a gold whisker with a radius $R = 50\,\mathrm{nm}$, only the fundamental $m = 0$ order mode can propagate. Comparing the total scattered field projected along the electron trajectory $|E_\mathrm{x}|$ at a distance of $L = 1460\,\mathrm{nm}$ from the end, the purely reflection-based response of the whisker is gradually suppressed by the phase-matching mechanism for tapers with increasing opening angle, which finally evolves to be the dominant feature for the taper with 50° opening angle.

3.2.2 Phase-matching at variable electron speeds

The aforementioned hyperbolic equation for phase-matching resonances contains a scaling factor that in turn depends on the relativistic speed v_{el} of the swift electron. Lowering the acceleration voltage of the electron microscope therefore implies a redshift of the resonance dispersions. By contrast, effects caused by the reflection mechanism remain constant, as they explicitly depend on the taper

geometry. Spectral EELS line scans were performed, using a monochromated JEOL electron microscope, along a gold taper with an opening angle of 19° for both 200 and 60 keV electrons (figure 3.15). Tracing the maxima in the experimental spectral dispersions for the first two mode orders clearly reveals a redshift for the lower acceleration voltage (figure 3.15 c), as confirmed also by numerical calculations for various acceleration voltages (figure 3.15 e). These measurements therefore directly prove the existence of the phase-matching mechanism in plasmonic gold tapers.

3.2.3 Far-field radiation of plasmonic gold tapers

In addition to EELS experiments, where energy-loss probabilities due to local excitation processes are probed, the aforementioned far-field radiation of plasmonic tapers was spectroscopically analysed by CL measurements for two tapers with opening angles of 13° and 47°.[70] Highest CL intensities were measured for probe positions at certain distances to the apex, which result from a more efficient plasmonic excitation of the structure. This observation is confirmed by spectral line scans of the electron probe along the shaft of both tapers, as shown in figures 3.16 and 3.17, respectively. For the 13° taper (figure 3.16 a), strong CL intensities arise for wavelengths in the range between 500 and 700 nm, when the taper is excited at a distance of roughly 300 nm from the apex. Furthermore, a redshift is observed for larger apex distances up to 800 nm, beyond which the intensity decreases due to damping effects. In addition to the experimental results, CL spectra were simulated based on numerical solutions to Maxwell's equations for the specific taper geometry and show a good qualitative agreement (figure 3.16 b). Interestingly, although the local field enhancement is huge at the very apex,[195,196] no significant radiation

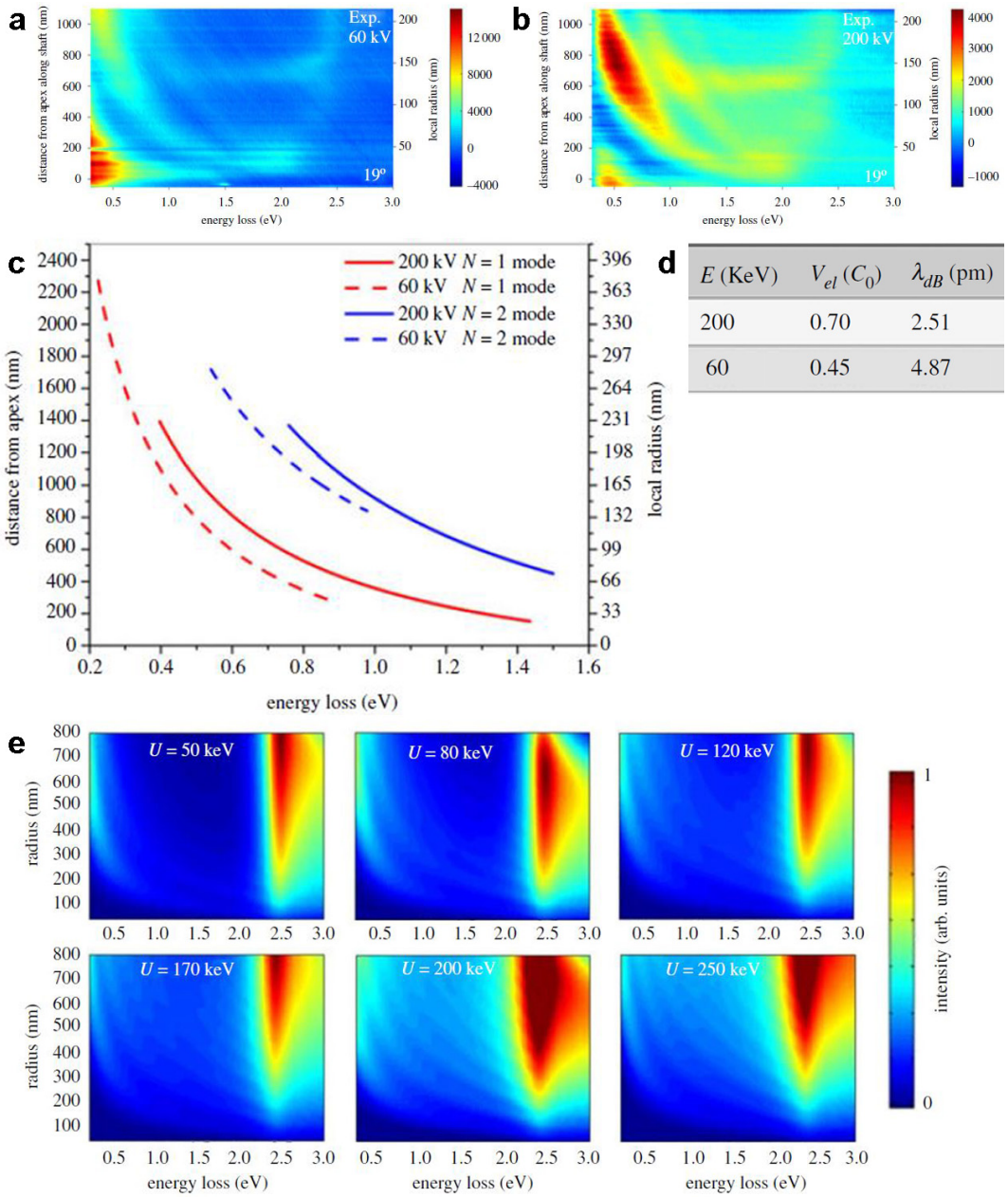

Fig. 3.15: Experimental EELS line scans along a taper with an opening angle of 19° for acceleration voltages of 200 kV (a) and 60 kV (b). The dispersions of extracted maxima (c) show a clear redshift for 60 keV electrons (dashed lines) for the first two mode orders (lower red curve and upper blue curve) compared with 200 keV electrons (solid lines). The associated relativistic electron velocities and correlated de Broglie wavelengths are shown in (d), where c_0 is the speed of light in vacuum. (e) Simulated EELS line scans for the depicted electron energies reveal a blue shift of the resonance dispersions with increasing electron velocity.

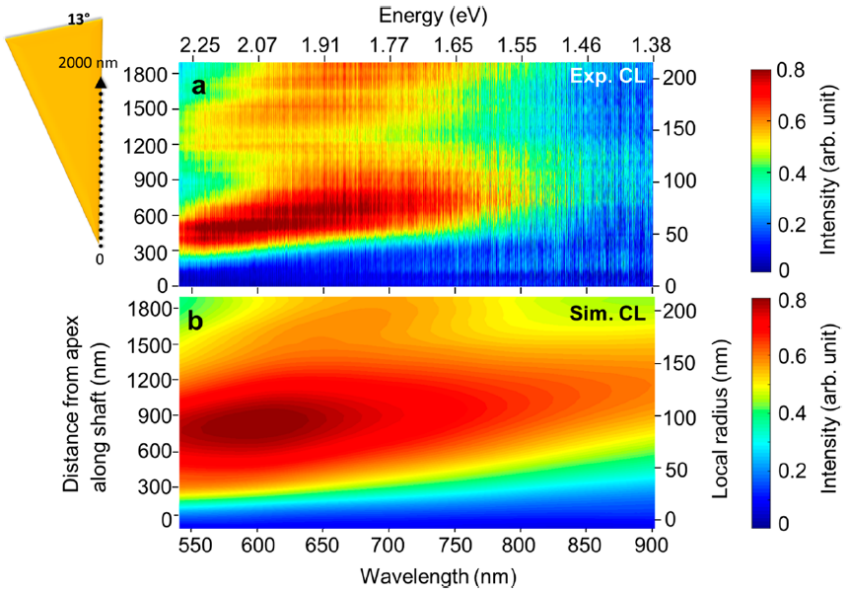

Fig. 3.16: (a) Experimental and (b) simulated CL spectra as a function of the probe distance to the apex for a taper with an opening angle of 13°. The corresponding local radii are shown on the second ordinate of the diagrams. The scale for the spectral domain is indexed for both wavelength (at the bottom) and energy (on the top). Adapted and reused with permission from the original publication. [70]

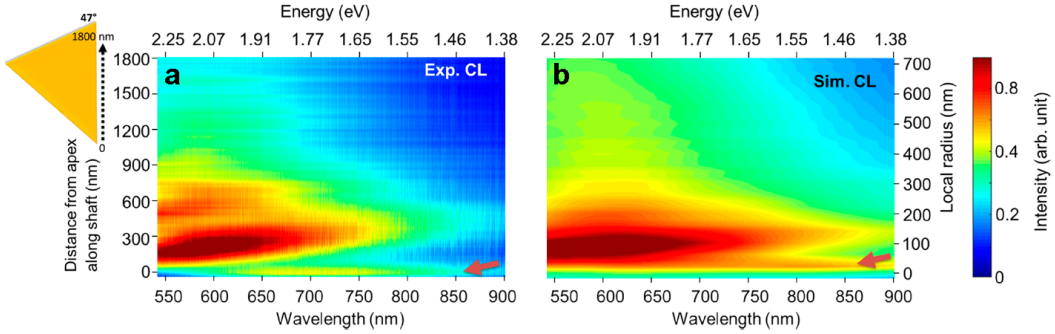

Fig. 3.17: (a) Experimental and (b) simulated CL spectra as a function of the probe distance to the apex for a taper with an opening angle of 47°. The corresponding local radii are shown on the second ordinate of the diagrams. The scale for the spectral domain is indexed for both wavelength (at the bottom) and energy (on the top). Adapted and reused with permission from the original publication. [70]

is observed for this particular excitation position. However, as only the $m = 0$ order mode can propagate for local radii below 50 nm, energy is being carried away from the apex through backpropagation. This mechanism can be seen as a reciprocal process to the principle of adiabatic nanofocusing. In the case of the 47° taper, a similar radiation pattern is observed above a certain critical local radius for both experimental and simulated results (figure 3.17 a,b). In addition, a broad spectral feature between 600 and 800 nm arises for an excitation position at the very apex. For the drastically changing local radius, the adiabaticity condition fails and the excited mode radiates to the far-field. For both taper geometries, the major radiation is observed for excitation positions above a certain distance from the apex and originates from the decay of higher-order angular momentum modes with $|m| > 0$.[154]

3.2.4 Conclusions

Conical metallic nanostructures in the form of single-crystalline gold tapers were investigated experimentally by means of EELS and CL spectroscopy inside electron microscopes. Supported by analytical and numerical FDTD simulations, it could be shown that resonances in the EELS signal originate from taper eigenmodes with higher-order angular momenta that interact with the exciting electron via a phase-matching mechanism. This effect was proven by measurements at different acceleration voltages, as it depends on the electron velocity. Modelling conical tapers in a local radius approach by infinitely long fibers along with measurements of tapers with various opening angles revealed that the back reflection of the fundamental mode at the apex becomes the dominant effect for narrow opening angles. The plasmonic excitation is most efficient at a certain distance to the apex and adiabatic nanofocusing fails

for large opening angles, as it could be shown by spatially resolved far-field measurements.

Contributions to this project This chapter is based on a review article that was originally published in the frame of the discussion meeting issue "dynamic in situ microscopy relating structure and function".[1] Robin Lingstädt drafted and wrote the manuscript, summarizing partly new experimental results, but mainly work that had been carried out and published previously by colleagues at the MPI-FKF and other institutes, who are listed as coauthors. The project was supervised by Peter A. van Aken and Nahid Talebi, who also performed the numerical calculations. EELS measurements were conducted by Wilfried Sigle and Surong Guo, who also performed the CL experiments together with Alfredo Campos and Mathieu Kociak. Fabrication and optical measurements on gold tapers were done by Martin Esmann, Simon F. Becker and Christoph Lienau. The new EELS measurements on gold tapers at variable acceleration voltages were done by Eiji Okunishi and Masaki Mukai at the Japan Fine Ceramics Center (JFCC) in Nagoya.

3.3 Directional far-field radiation of chiral gold nanohelices

Chiral plasmonic nanostructures possess a remarkable chiroptical response, orders of magnitude stronger than that of natural biomolecular systems, making them highly promising for a wide range of biochemical, medical, and physical applications. Despite extensive efforts to artificially create and tune the chiroptical properties of chiral nanostructures through compositional and geometrical modifications, fundamental understanding of their underlying mechanisms remains limited. In this study, we present a comprehensive investigation of individual gold nanohelices using advanced analytical electron microscopy techniques. Our results, as determined by angle-resolved CL polarimetry measurements, reveal a strong correlation between the circular polarization state of the emitted far-field radiation and the handedness of the chiral nanostructure both in terms of its dominant circularity and directional intensity distribution. Further analyses, including electron energy-loss measurements and numerical simulations, demonstrate that this correlation is driven by longitudinal plasmonic modes that oscillate along the helical windings, much like straight nanorods of equal strength and length. The underlying mechanism of the observed emission in the visible range is based on the radiative decay of transverse dipolar charge oscillations along the short axis of the helices that form for certain higher-order modes. Our findings provide new insight into the fundamental mechanisms of chiral plasmonic nanostructures and pave the way for their future development and application in a wide range of fields, such as nano optics, metamaterials, molecular physics, biochemistry and, most promising, chiral sensing via new plasmonically enhanced chiral optical spectroscopy techniques.

The concept of chirality is a fundamental property that refers to an object's lack of mirror or inversion symmetry. This results in an object and its mirror image being not transformable through rotational or translational symmetry operations. Despite its seemingly abstract definition, the distinction between these two enantiomorphs is fairly important and chiral objects are surprisingly present in everyday life. Besides staircases, screws, or human hands, chirality in nature plays an important role down to the nanoscale, as most important biomolecules exhibit exclusively one handedness, including essential amino acids and sugars in deoxyribonucleic acid (DNA) that form the basis of life.[197,198] In addition to these geometrical and biochemical considerations, also physical properties are affected and result for instance in chiroptical phenomena, e.g. LCP and RCP light interact differently with chiral nanoobjects. This effect can be spectroscopically analyzed via CD measurements. In contrast to most chiral biomolecules or natural media, which only show a comparably weak chiroptical response, this effect is increased by several orders of magnitude for chiral plasmonic nanostructures or metamaterials, where electrons can be collectively excited to perform harmonic oscillations at the surfaces.[199] As a consequence, major efforts have been made to create artificial chiral nanostructures via various methods[200–207] and characterize them through chiroptical measurements.[208] As an example for 3D and hence true chiral structures, gold nanohelices have been fabricated in a top-down approach to study the influence of structural variations such as pitch or helical radius on chiroptical effects.[209,210] A shift of the response in the dichroic signal from the infrared to the visible spectral range could be achieved for even smaller helices, produced via an alternative shadow-growth technique, following a bottom-up approach.[75,76] Optical CD measurements that revealed strong chiroptical effects were performed on ensembles but also on freely diffusing single nanohelices,[211] as well as on other single nanocrystals and fabricated nanostructures.[212] Consequently, the inves-

tigation of individual chiral plasmonic structures with high spatial resolution, as provided by electron microscopy, gives additional insight, especially as the aforementioned LSPRs can be excited by electron beams in a wide energy range and analyzed via EELS.[8–11,40,50–53,213–216] Furthermore, the generated CL radiation[48,217] carries valuable polarization information, also in relation to the chirality of the underlying structure.[82,218,219] In contrast to previous works, where these analytical techniques were mainly applied to arrays or individual chiral nanostructures with a planar geometry, in the present study, individual 3D chiral gold nanohelices are investigated with high spatial resolution inside transmission and scanning electron microscopes. The combination of CL polarimetry and EELS is used to measure angle-resolved far-field radiation patterns of left- and right-handed structures and unravel the underlying plasmonic modes. Numerical simulations reveal that the observed CL emission in the visible spectral range originates from the decay of transverse dipolar modes that arise due to the 3D helical shape. We show that excited nanohelices emit directional CPL and that its circular polarization state is correlated both with the handedness of the structure and the electron beam position.

3.3.1 Optical and structural characterization

The fabrication of chiral gold nanostructures was achieved through a combination of BCML and GLAD. This process is described in more detail in section 2.1.3 on page 29. It allowed for the creation of helical nanostructures with a height of approximately 240 nm and an outer diameter of 140 nm. The pitch between two windings is 110 nm, with a thickness ranging from 20 nm to 40 nm. Importantly, both left- and right-handed helices were successfully synthesized by selecting the corresponding rotation direction during the growth.

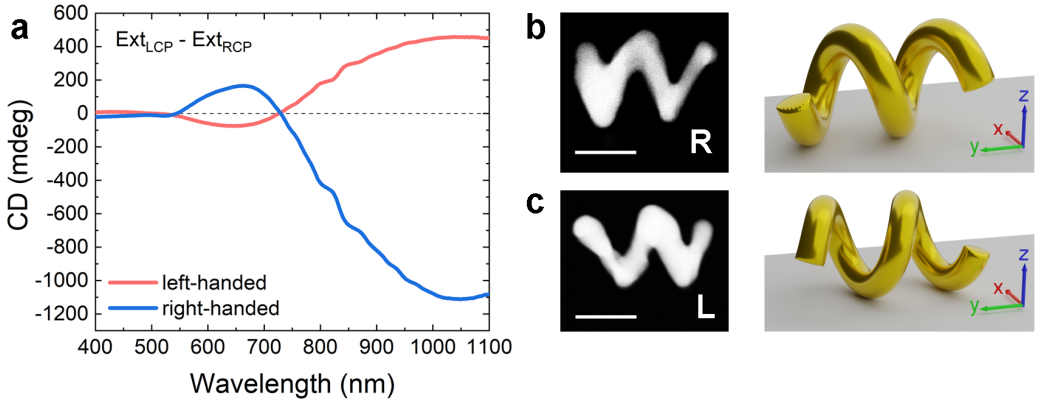

Fig. 3.18: (a) CD measurements in solution revealing the optical activity of the fabricated chiral nanostructures. The extinction of LCP and RCP light is related to the handedness of the measured structures. (b,c) Individual nanohelices were geometrically characterized by STEM techniques. HAADF images show 2D projections for a right-handed helix (R) at the top and a left-handed one (L) at the bottom. The corresponding models of the 3D structures and their orientation were determined by perspective mapping.

CD extinction measurements were conducted in metafluids containing the helices with different handedness, revealing their optical activity. As shown in figure 3.18 a, the relative extinction strength for LCP and RCP light correlates with the handedness of the chiral structure. The change in the sign of the CD signal, commonly referred to as the Cotton effect, has been reported for similar nanohelices[75] and other plasmonic chiral nanostructures.[204,220,221] In comparison to the aforementioned previous studies on gold nanohelices with smaller dimensions, the overall dichroic response of the helices produced in this study was found to be redshifted towards longer wavelengths in the spectrum. Individual chiral gold nanohelices were investigated further by means of analytical transmission electron microscopy, both regarding their geometrical and inherent material properties. HAADF images were acquired with a STEM for right- and left-handed structures (figures 3.18 b and c). From these 2D

Fig. 3.19: Reconstructed 3D nanohelices show the expected handedness of the chiral structures. Movies of the rotating 3D reconstructions are available online.

projections, some of the geometrical properties like helical radius, number of windings and their thickness can be measured directly. For a full geometrical characterization, however, the 3D shape of the structures and their orientation on the flat amorphous carbon substrate have to be considered. Perspective mapping of constructed model helices revealed a flat orientation with a rotation around the long axis as shown by the illustrations next to the STEM images. The created models resemble the real helices in an idealized and, hence, simplified form and are used as a basis for theoretical calculations and simulations. A qualitative confirmation that the experimentally grown helices indeed show the expected handedness was achieved by ET, where images of the structure of interest are acquired under various tilt angles over a wide angular range and spatially aligned by cross-correlation filtering. The 3D models of the underlying structures are then reconstructed via the application of different algorithms as described in section 2.2.5 on page 39. The results for both left- and right-handed helices are shown in figure 3.19, unavoidably again in a 2D projection. Movies of the rotating reconstructed volumes give a better impression of their 3D shape and will be available online after publication.

3.3.2 LSPRs investigated by EELS

The plasmonic properties of individual gold nanostructures were investigated via electron energy-loss measurements that were conducted using the ZEISS SESAM. To obtain spatio-spectral information about the localized plasmons, spectrum images were acquired with a spatial sampling of 7 nm, providing a 3D data cube, where each voxel contains a low-loss spectrum with an energy resolution of approximately 80 meV, as determined by the FWHM of the ZLP. The EELS findings are confirmed through simulations based on the BEM,[100,222] which solve Maxwell's equations with respect to the real 3D shape of the sample. The distinct architecture of the helix comprises two full windings with a consistent pitch of 105 nm and a clearly defined outer helical diameter of 135 nm. Its thickness was measured, with an averaged value of 36 nm in diameter. These dimensions were crucial in further BEM simulations of the helix's material properties and plasmonic resonance effects. The experimentally acquired and simulated electron energy-loss spectra for the left-handed helix are depicted in figures 3.20 a and b, respectively. The similar spectroscopic data for a right-handed structure is shown in figure 3.24 at the end of this section on page 100 for comparison. Spectra were extracted at the most significant excitation positions at the end of the helix (position 1, black line) and at the center winding (position 2, red line), both in an aloof configuration, i.e. the electron passing by the specimen in close proximity, as marked in the inset graphics. The experimental SNR was improved by averaging over four neighboring pixels. Overall, experimental and simulated results agree very well with only slight deviations, that can be attributed to experimental conditions and an idealized and hence simplified sample geometry assumed in BEM simulations.

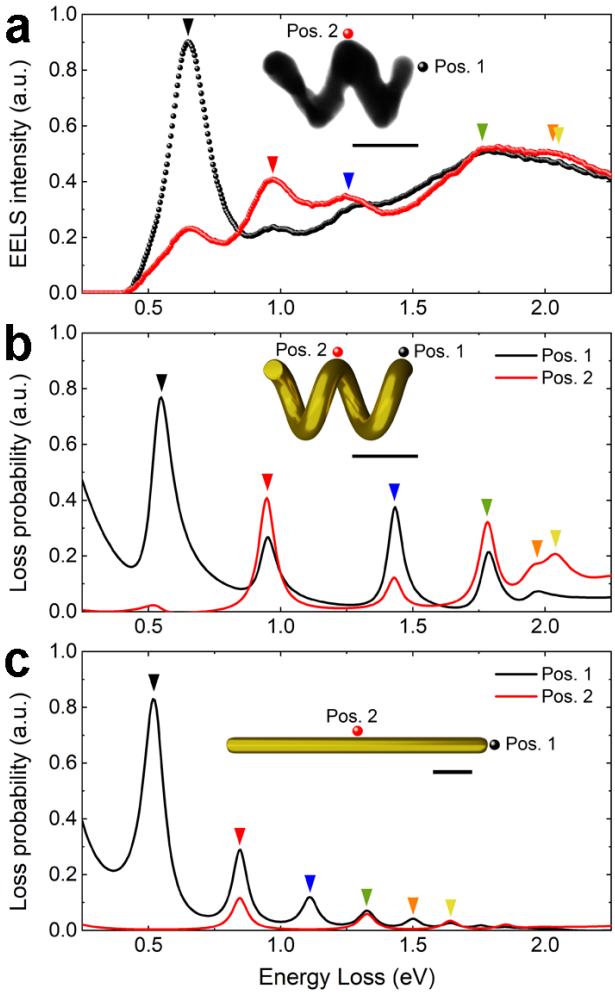

Fig. 3.20: (a) Experimental electron energy-loss spectra of a left-handed nanohelix, being excited at positions 1 at the end of the structure (black curve) and 2 at the center winding (red curve) in an aloof configuration, as marked in the inset graphic. A strong spectral peak at the lowest resonance energy around 0.6 eV is observed at the end of the structure, whereas the second resonance around 0.9 eV is stronger at the center. (b) Simulated electron energy-loss spectra obtained via the BEM. (c) A straight nanorod with identical thickness and center path length as the helix reveals that the observed resonances originate from "antenna modes" of multiple orders. While the spectral peak of the fundamental dipolar mode is located at the same energy around 0.5 eV like the one of the helix, all higher-order modes appear redshifted. The scale bars are 100 nm.

In figures 3.20 a and b, the pronounced spectral peak at the lowest energy around 0.6 eV (black triangles) is mainly present at excitation position 1 with a redshift of only 100 meV in the simulated spectrum. Both datasets show the highest excitation efficiency for the second resonance at around 0.9 eV (red triangles) close to the center winding at position 2. The third resonance at 1.25 eV (blue triangles) is found to be blueshifted at 1.43 eV in the simulation, with a discernible decrease in intensity near the center winding. Both experimental and simulated data show a fourth resonance around 1.8 eV (green triangles), with the experimental data presenting a less distinct peak. A shallow maximum in the experimental spectrum around 2 eV, mainly visible at position 2, is associated with the fifth and sixth resonances, which are close in energy in the simulation (orange and yellow triangles).

In a comparison of a helical nanostructure with a straight nanorod of equivalent strength and length (figure 3.20 c), we observe remarkable similarities in resonance behavior, as both systems exhibit "antenna modes", that have been reported also for silver helices.[223] However, there are also notable differences, such as all higher-order resonances in the simpler straight rod geometry being redshifted at lower energies, due to the lack of interwinding interactions. For the same reason, the selection rule that the lowest-, third- and fifth-order modes are not excitable at the center of a rod (position 2) is weakened and, even more intriguingly, reversed for higher-order resonances, as transverse dipolar charge oscillations arise for the 3D helical geometry. These findings suggest that interwinding interactions play a significant role in determining the excitation behavior of helical nanostructures.

The spectra exhibit weaker resonances at higher energies. However, the spatially resolved EELS probability maps, extracted over a 100 meV range at the depicted resonance energies (figure 3.21 a), showcase the characteristic pattern

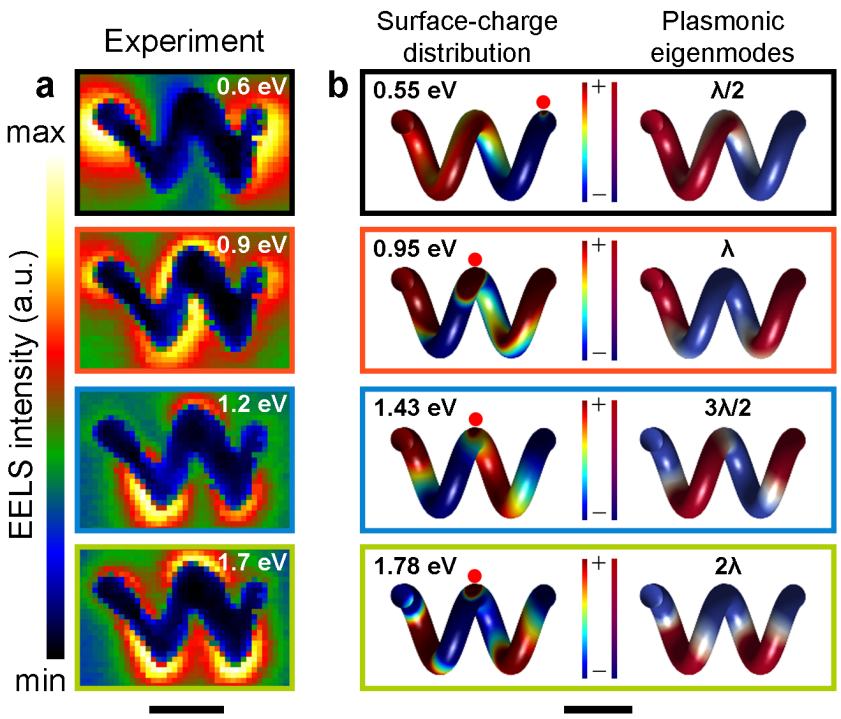

Fig. 3.21: (a) Energy-filtered images at the indicated resonance energies over a width of 0.1 eV, mapping the spatial EELS probability and emphasizing the character of multiple-order plasmonic resonances. (b) Simulated surface-charge distributions and underlying plasmonic eigenmodes computed for the depicted resonance energies. The excitation position of the electron beam is marked with a red dot. The scale bars are 100 nm.

of dipolar and multiple-order LSPRs, a well-known phenomenon supported by previous theoretical studies and experimental observations, for example in gold nanorods.[18,43,224–230] Furthermore, the relation between the lowest (dipolar) resonance energy and the real 3D path length of each investigated helical structure aligns with the values determined for gold nanorods through theoretical and experimental investigations (figure 3.22).

The validity of the hypothesis that charge oscillations occur along the helically twisted rod is substantiated by simulated surface-charge distributions and

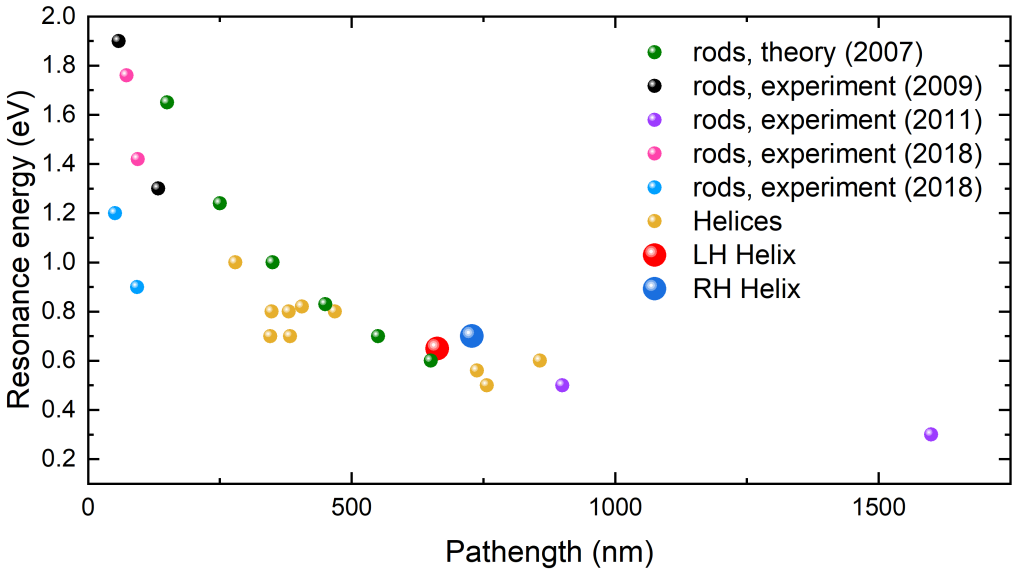

Fig. 3.22: The resonances of the lowest-order dipolar plasmonic modes are compared for gold nanorods and nanohelices. Their experimentally measured or theoretically predicted energies are plotted against the lengths of the rods and path lengths along the helical windings, respectively. [18,225,226,229,230]

plasmonic eigenmodes, computed for the specified resonance energies and excitation positions, as marked in figure 3.21 b. The plasmonic eigenmodes are labeled with the relative path length of the helical structure in comparison to the corresponding wavelength λ at the resonance energy. The simulations reveal a consistent pattern of longitudinal multiple-order LSPRs along the helical windings, with only a localized perturbation observed at the excitation position. This provides strong evidence for the occurrence of charge oscillations along the helically twisted rod. In addition, the 2λ- and higher-order plasmonic eigenmodes result in transverse dipolar LSPRs, oriented along the short axis of the nanohelices. In other words, in addition to the longitudinal dipole-dipole interactions due to Fabry-Pérot-like resonances along the windings, the helical geometry leads to secondary charge oscillations with a dipolar character, as

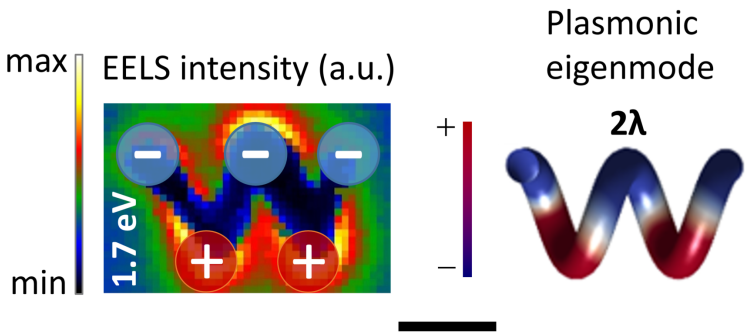

Fig. 3.23: Electron energy-loss intensity distribution filtered at the resonance energy of 1.7 eV of the underlying plasmonic eigenmode 2λ as shown on the right. Although this higher-order longitudinal plasmonic mode follows the helical windings, a secondary charge oscillation forms due to the 3D geometry of the structure. Its characteristic corresponds to a dipole that is oriented along the short axis of the helix. The scale bar is 100 nm.

illustrated in figure 3.23. A similar transverse dipole distribution has been reported for nickel and silver nanohelices.[231]

3.3.3 Angle-resolved CL polarimetry

The optical activity of an ensemble of the gold nanohelices was previously confirmed by CD measurements (figure 3.18 a on page 92). Here, we further explore the properties of the light emitted upon electron impact for individual nanohelices at the nanoscale by CL spectroscopy techniques within an SEM. While raster scanning a focused electron beam over the ROI, multiple signals including SEs for imaging and the emitted CL light are detected and analyzed. The far-field radiation of the nanostructure, excited by the electron beam, is collected by a parabolic mirror, as shown in figure 3.25 a, and directed outside the microscope for further analysis. In the spectroscopic imaging mode, emission spectra are measured for each spatial pixel, with the highest intensity

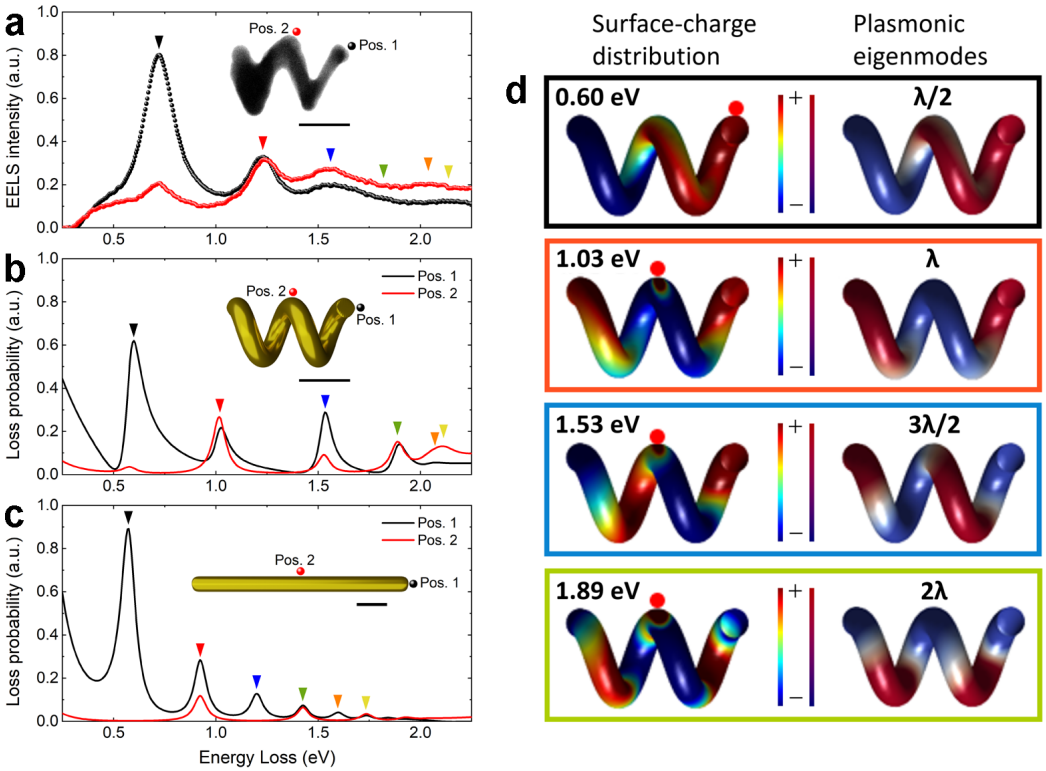

Fig. 3.24: (a) Experimental electron energy-loss spectra of a right-handed nanohelix, being excited at positions 1 at the end of the structure (black curve) and 2 at the center winding (red curve) in an aloof configuration, as marked in the inset graphic. A strong spectral peak at the lowest resonance energy around 0.7 eV is observed at the end of the structure, whereas the second resonance around 1.2 eV and all higher-order resonances are stronger at the center. (b) Simulated electron energy-loss spectra obtained via the BEM. (c) A straight nanorod with identical thickness and center path length as the helix reveals that the observed resonances originate from "antenna modes" of multiple orders. While the spectral peak of the fundamental dipolar mode is located at the same energy around 0.6 eV like the one of the helix, all higher-order modes appear redshifted. (d) Simulated surface-charge distributions and underlying plasmonic eigenmodes computed for the depicted resonance energies. The excitation position of the electron beam is marked with a red dot. The scale bars are 100 nm.

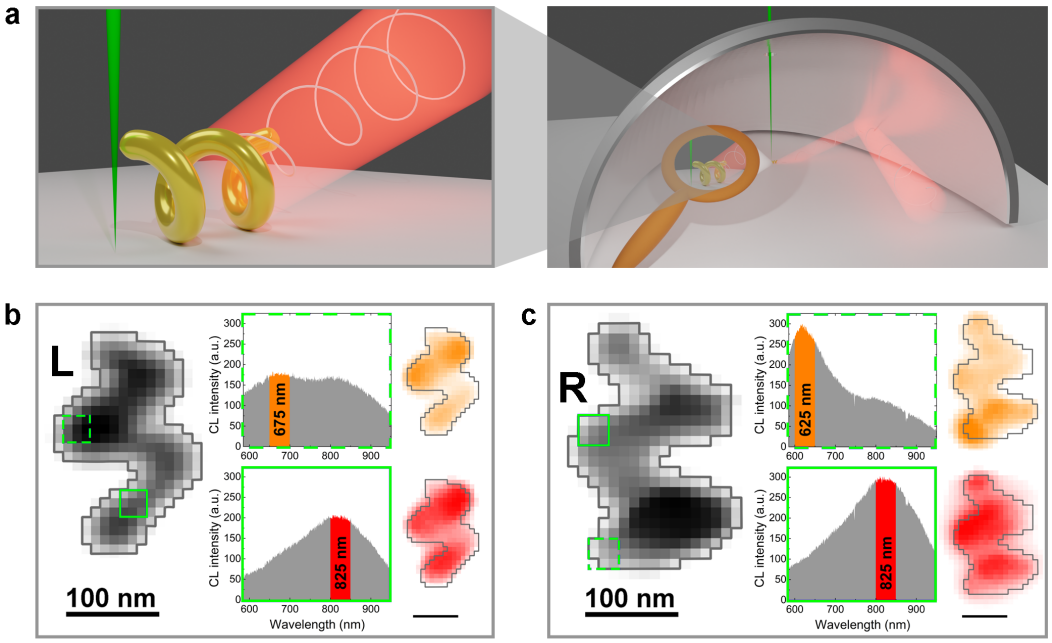

Fig. 3.25: (a) Schematic of the experimental setup. The nanostructure is excited by the electron beam that passes through a hole in the parabolic mirror. The specimen, precisely positioned in the focal point of the parabolic mirror, emits light that is transformed to a parallel beam and directed outside the microscope for in-depth analysis. (b,c) SE images were used to determine the circumference (grey line) of the left- (L) and right-handed (R) structures. CL spectra, extracted at the excitation positions marked with dashed and solid green lines, reveal strongest emission between 600 nm and 700 nm (orange color) and above 800 nm (red color). The corresponding excitation efficiency maps are shown in addition. The scale bars are 100 nm.

recorded for wavelengths between 600 nm and 700 nm and above 800 nm. The spectra shown in figure 3.25 b and c were extracted at the positions that are marked with dashed and solid green lines on the SE images. The correlation between electron beam position and the emission intensity, filtered for these wavelengths, results in a set of spatially resolved excitation efficiency maps, displayed in corresponding colors in arbitrary units. The intensity distribution reveals five key positions, the two ends and the three most extended points along the helical windings. This information is crucial to the subsequent angular and polarimetric measurements, that are beneficially acquired at the positions demonstrating the highest excitation efficiency and spectrally filtered around the peaks of the CL spectra. We note that the higher-order plasmonic modes $5/2\lambda$ and 3λ (orange and yellow triangles in figure **??** on page 95), that correspond to radiation around 600 nm, are expected to be non-radiative in CL experiments.[43] However, due to the 3D shape of the structure, secondary transverse dipolar charge oscillations form and their decay results in the observed radiation, making the otherwise dark modes bright upon the electron excitation at specific positions of the nanohelix.

In contrast to the aforementioned spectroscopic imaging mode, where the far-field radiation is accumulated over the entire accessible angular range, the differentiation of radiation directions in the angle-resolved configuration adds multidimensionality to the measured signal itself. In combination with band-pass and polarizing filters, the emitted light of an excited structure can be characterized in great detail. The chiral nature of the nanostructures under investigation requires particular focus on their circularly polarized components (figure 3.26 a). The normalized differential signal between the LCP (red color) and RCP (blue color) emission defines the normalized Stokes parameter S3 and provides insight into the directional emission properties concerning

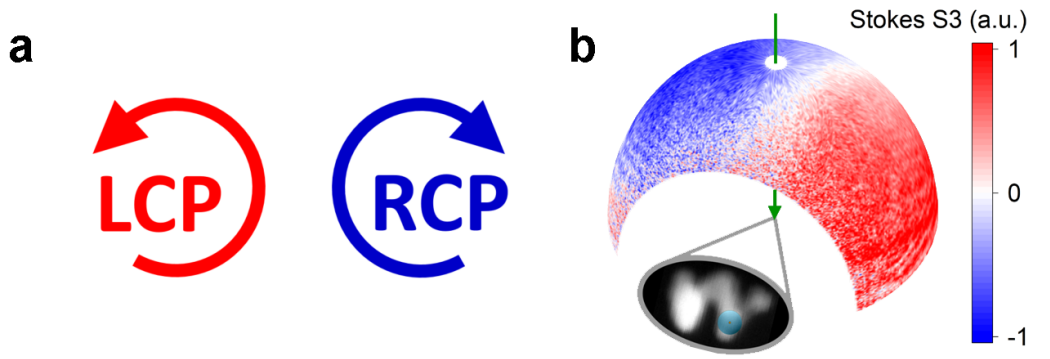

Fig. 3.26: (a) Polarimetric characterization of the emitted light is achieved through filtering for different polarization states, such as LCP (red) or RCP light (blue). (b) 3D plot of an angle-resolved far-field intensity pattern on a fictional hemispheric detection plane. The light is emitted by the nanoscopic sample in its center, being excited by the electron beam at the position marked in the inset graphic. The color code shows the normalized differential signal (Stokes S3) between the emission intensity of LCP (red) and RCP light (blue).

these polarization states (figure 3.26 b). The position of the actual excitation is marked in the inset graphic. A quantitative 2D representation of the hemispherical intensity distribution for both left- and right-handed helices is given by spherical polar plots (figure 3.27 a and b), with the polar angle on the radial axis and the azimuthal angle clockwise along the circumference. The structure is located in the center and oriented as shown in the inset graphics along with the marked excitation position. Analyzing the angle-resolved differential signal between LCP and RCP light intensities reveals two intriguing effects, consistent over all investigated structures. The first being that the strongest effect is observed in the direction of the long axis of the helical structure for polar angles approaching 90° and towards the opposite side of the excitation position at one end of the helix. The second is that the dominating handedness of the CPL emitted in this direction coincides with the handedness of the chiral structure itself. Line-scans following the polar

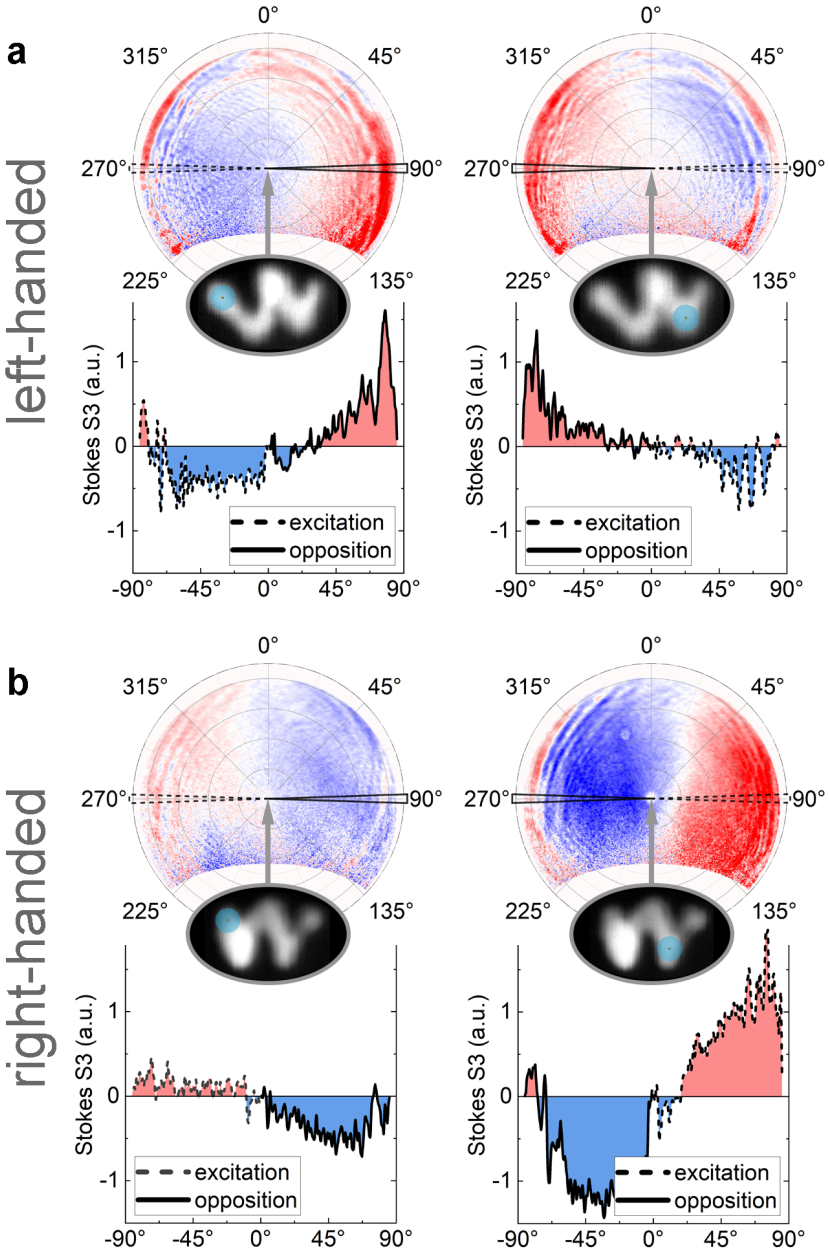

Fig. 3.27: Plots of the same dichroic signal like in figure 3.26 b in a more quantitative 2D representation and for nanohelices with different handedness. (a) When exciting at the ends of a left-handed structure, relatively more LCP light is emitted in the opposite direction, which is the "pointing-direction" of the helix. This effect is visualized through line plots along the long axis of the helices. (b) The same effect, but with reversed circular polarization is observed for a right-handed helix.

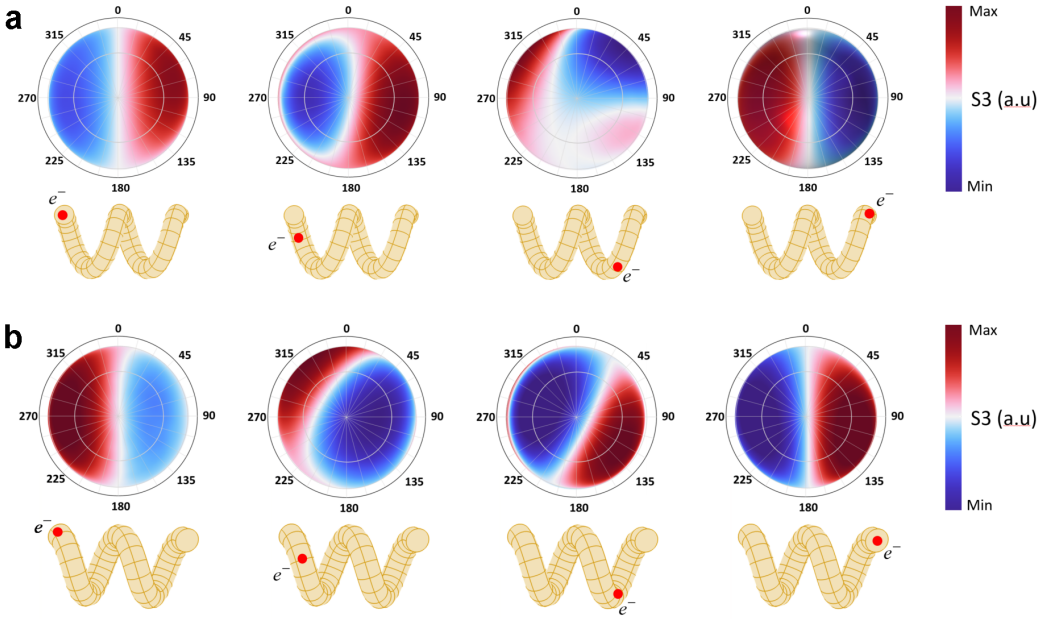

Fig. 3.28: Spherical polar plots of the simulated angle-resolved Stokes parameter S3 for the left-handed (a) and right-handed nanohelix (b), showing whether more LCP or RCP light is emitted in certain directions. The excitation positions by the electron beam are marked on the 3D models below each plot.

angle over the hemisphere in parallel orientation to the long axis emphasize this effect. The differential signal in the excitation direction (dashed line) and in the opposite direction (solid line) is plotted below each graph, with the same behavior observed in the reversed circular polarization for right-handed helices (figure 3.27 b). For excitation positions at the center winding (position 2) no such consistent effect is observed. To validate these experimental findings, numerical calculations were conducted using idealized 3D models, consistent with those used in the EELS analysis in section 3.3.2. Spherical plots that show the computed angle-resolved intensity distribution of the dichroic signal are provided in figure 3.28. The results confirm the experimentally observed opposite effect for left- and right-handed helices and visualize the gradual

transition to the inverted polarization distribution for each structure, when the excitation position is shifted towards the opposing end of the helix. These extreme positions result in the strongest effect with an almost symmetric distribution along the long axis. The slight geometrical differences between left- and right-handed helix do not affect the qualitative outcome of the simulation. In addition, the potential effect of the helical winding direction in relation to the moving electron can be neglected.

According to theoretical predictions, based on a separate discussion of the full and radiative electromagnetic local density of states (EMLDOS) of metallic nanoparticles, at the length scales discussed here, a direct link can be assumed between the resonance energies in EELS and the intense far-field radiation in CL measurements at corresponding wavelengths.[43,44] The emission in the visible spectral range from the investigated helical nanostructures is attributed to plasmonic modes with resonance energies between 1.4 eV and 2 eV. Meanwhile, lower-order modes radiate in the infrared, which cannot be detected by the spectrometer used in this study. Numerical calculations were utilized to predict the emitted far-field radiation from individual left- and right-handed nanohelices also spectroscopically at characteristic excitation positions (figure 3.29). We thoroughly compared emission peak positions in the simulated CL spectra (figures 3.29 d and e) with measured and simulated resonance energies in EELS (figures 3.20 a and b), paying special attention to the spectral shape and excitation efficiency in relation to the excitation position. Our findings indicate that for the left-handed helix, the enhanced emission around various wavelengths, including 900 nm, 730 nm, 640 nm and 610 nm, corresponds to plasmonic resonances at 1.43 eV, 1.78 eV, 1.98 eV and 2.04 eV, respectively, which are marked with triangles in the corresponding colors blue, green, orange and yellow. In particular, the highest-order mode 3λ, marked with a yellow

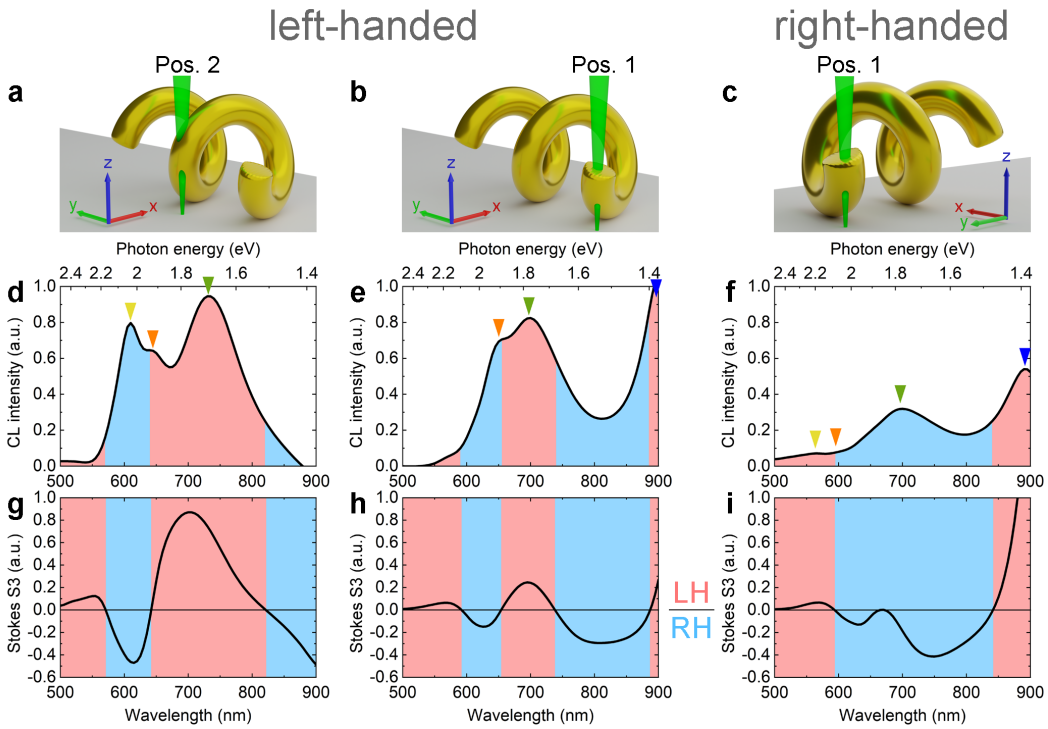

Fig. 3.29: (a,b,c) 3D models of the left-handed and right-handed nanohelix, being excited at different positions by the electron beam (illustrated in green color). (d,e,f) CL spectra in the visible range reveal emission maxima that are related to plasmonic resonance energies (figure 3.20 on page 95) and marked with triangles in corresponding colors. (g,h,i) Ratio between LCP and RCP components of the emitted far-field radiation, integrated over the entire accessible angular range. Positive (red color) and negative (blue color) values indicate whether LCP or RCP emission is dominant for a given wavelength.

triangle, radiates more strongly around 610 nm than the neighboring one $5/2\lambda$ (orange triangle) around 640 nm. However, the former is exclusively excitable at the center winding (position 2). Conversely, the radiation around 900 nm (blue triangle) only occurs when the helix is excited at the end (position 1), which is represented in the simulated energy-loss probability of the corresponding resonance of $3/2\lambda$ at 1.43 eV as well (figure 3.20 b). The most dominant 2λ mode, which most likely corresponds to the one observed in the CL experiment (figure 3.25 b), radiates around 730 nm (green triangle) and is excitable both at the end and center winding of the helix. The spectral features in the experiment do appear slightly redshifted at longer wavelengths. However, these deviations can again be attributed to the simplified geometrical assumptions made in the simulation environment and the used dielectric function. The simulated CL spectra for the right-handed structure, shown exemplarily for excitation position 1 at the end of the helix (figures 3.29 c and f), exhibit similar spectral features. In the collective agreement of measured and simulated EELS and CL spectra, the plasmonic resonances appear blueshifted at higher energies and shorter wavelengths, as compared to the left-handed structure, due to its slightly different geometry.

In addition to the total emission intensity, further information is contained in the intrinsic polarimetric properties of the radiation. Of particular interest for chiral structures is the relation between LCP and RCP light. The simulated dichroic signal is plotted below each intensity curve for the different helices and excitation positions (figures 3.29 g, h and i). In our simulation, we utilized a boundary probe to capture the CL polarimetry spectra. This probe integrated the Poynting vector of the three coordination components of the emitted light across the entire top surface of the hemisphere. The radiation of the aforementioned dominant 2λ mode around 730 nm clearly shows a LCP

characteristic, whereas this tendency switches to RCP light for the radiation close to 600 nm, which is associated with higher-order plasmonic modes $5/2\lambda$ and 3λ. Interestingly, this behavior is in agreement with the results from the initial CD measurements (figure 3.18 a on page 92) and hence resembles this macroscopic property of an ensemble of identical particles. Regarding the right-handed helix, the simulated left-to-right circularity ratio of the emitted light (figure 3.29 i) is qualitatively similar to that of the left-handed helix at a comparable excitation position. Quantitatively, however, the tendency towards RCP light is more pronounced. Cumulatively over the visible spectral range, CPL with a dominant right-handed characteristic is expected for the right-handed helix.

3.3.4 Conclusions

Our study demonstrates the successful preparation and optical characterization of the chiroptical response of both left- and right-handed chiral gold nanohelices. The shape of individual particles and their handedness was confirmed as expected through ET reconstructions. We performed a comprehensive investigation of the plasmonic resonances using a combination of EELS measurements and numerical simulations. Our results show that multiple-order longitudinal LSPRs are related to surface-charge oscillations along the helical windings, while interwinding interactions lead to slightly shifted resonance energies compared to straight rods with similar thickness and (path) length. In addition, higher-order modes induce the formation of secondary transverse dipolar LSPRs oriented along the short axis of the nanohelices. The radiative decay of these modes results in the observed CL emission at corresponding wavelengths. Angle-resolved CL polarimetry measurements of the emitted

far-field radiation revealed that the emission characteristic of CPL is both related to the handedness of the chiral structure and depends on the excitation position. Our simulations of the far-field radiation of excited nanostructures further confirmed that peaks in the CL intensity correspond to plasmonic resonances. Furthermore, both the excitation efficiency of these modes and the circular polarization characteristic of the emitted light strongly depend on the position of the exciting electron beam, the chirality of the structure and other geometrical properties. Studies of chirality for single nanostructures depend not only on the handedness of the structure, but also on the relative orientations of the structure and the excitation and detection beams. Here, the analysis of electron-beam-induced effects are particularly powerful in comparison with purely optical methods, as the exact geometric properties of the structure and the precise orientations can be determined together with the corresponding spectral response. The high precision facilitates the comparison with theory and suggests that electron-beam single-chiral-particle analysis can be a powerful tool to analyze chirality at the smallest of scales. This complex interplay opens up exciting opportunities for tailoring the chiroptical properties of nanostructures, with potential applications in a variety of scientific and technological fields.

Contributions to this project The underlying research article to this section was written by Robin Lingstädt. Left- and right-handed gold nanohelices were fabricated by Hyunah Kwon, who also performed the CD measurements together with Peer Fischer. Robin Lingstädt prepared the samples for further investigations, performed the geometrical characterization, ET, EELS and CL experiments and analyzed the data. The CL experiments were conducted together with Masoud Taleb. Simulations for CL and EELS were performed by Fatemeh Davoodi and Kenan Elibol, respectively. The project was supervised by Peer Fischer, Nahid Talebi and Peter A. van Aken.

4 Conclusions and outlook

In this thesis, phenomena related to plasmonic excitations on the nanoscale are investigated for planar structures, rotational symmetric and true chiral 3D objects. Experimentally, this is achieved through the application of different sample preparation and characterization techniques. While optical measurements via generalized spectroscopic ellipsometry and optical CD revealed the material properties on a macroscopic scale, spatially resolved investigations were performed by scanning-probe instruments, foremost via analytical electron microscopy. The initial excitation process of plasmonic modes by incident fast electrons was spectroscopically analyzed and spatially mapped by energy-loss measurements via EFTEM and STEM-EELS. In a complementary way, far-field radiation that originates from the radiative decay of these excitations was analyzed both spectroscopically and regarding its emission direction and polarization state by angle-resolved CL polarimetry. Besides experimental investigations, numerical simulations based on Maxwell's equations were performed to confirm the experimental results, to give further insight into the underlying physical phenomena and to visualize what is experimentally not accessible.

The conducted research in this thesis focuses on (i) the characterization of plasmonic edge-modes in Bi_2Se_3 nanoplatelets, (ii) their interaction with engineered

defect structures, (iii) the experimental prove of the phase-matching mechanism in plasmonic gold tapers, (iv) the characterization of longitudinal plasmon modes along helical windings, (v) their effect on emitted CL radiation and (vi) its characterization regarding emission direction and circular polarization.

In chapter 1, the potential of plasmonic nanostructures for technological applications was motivated and the fundamental principles of plasmonic excitations introduced. The technical setup of a TEM and its different operation modes for high-resolution imaging were explained and the capabilities of analytical electron microscopy highlighted with special focus on the techniques EELS and CL that were mainly used for the investigations related to this work.

Chapter 2 summarized technical aspects and descriptions related to the sample fabrication and preparation processes for the investigated nanostructures. Experimental procedures and instrumental configurations that were used for the acquisition of multi-dimensional datasets containing spectroscopic, directional or polarimetric signals were described. Mandatory and optional steps for data processing were mentioned and computational methods introduced.

In chapter 3, the scientific results of the three research projects were presented in individual sections. Bi_2Se_3 nanoplatelets were investigated in the first project. The anisotropic permittivity of this hyperbolic material and the support of room-temperature excitons, as confirmed by generalized spectroscopic ellipsometry and CL measurements, leads to the formation of HEEPs. Their propagation along clean particle edges and interaction with artificially created defect structures was experimentally investigated via EFTEM and STEM-EELS in combination with numerical calculations. The temporal evolution of excited modes was visualized on a femtosecond timescale via FDTD simulations.

In the second project, the plasmonic properties of single-crystalline gold tapers were reviewed. Investigations via EELS and CL spectroscopy in combination with FDTD simulations revealed two competing interaction mechanisms with fast electrons, depending on the opening angle. New EELS results, acquired at different acceleration voltages, directly proved the existence of the phase-matching mechanism, which depends on the initial electron velocity. Regarding the application of plasmonic gold tapers as a point light source via the adiabatic nanofocusing mechanism, CL investigations beyond the spectroscopic analysis in the form of angle-resolved measurements would be very interesting to study the directional emission pattern at the apex.

For the third project, true chiral 3D gold nanohelices were fabricated and optically characterized via CD measurements. Their left- and right-handed geometries were confirmed by ET. STEM-EELS investigations in combination with numerical BEM calculations revealed multiple-order plasmonic resonances along the helical windings that are very similar to straight rods of comparable strength and (path) length. Resulting far-field radiation was investigated via CL spectroscopy and angle-resolved polarimetry. The observed directional emission characteristic of CPL showed a strong correlation both to the handedness of the investigated nanohelix and the excitation position. Further experimental and theoretical studies of gold nanohelices with different geometries would certainly contribute to an in-depth understanding of these interesting phenomena. Variations in this regard include the number of windings and the pitch-distance between them or the combination of both chiralities in one single nanostructure.

Analytical electron microscopy has proven to be a highly capable tool for characterizing specimen at the nanoscale, either for technological applications or in the scope of fundamental research. Further developments of this technique have

pushed existing limitations continuously to higher levels, for example through an increased SNR by using direct electron detectors or the implementation of optimized MCRs, that provide an energy-resolution below 10 meV.[79] Low-loss EELS investigations, as presented in this work, will in general benefit from these technical improvements. In addition, the experimental investigation of phonons and their interaction with plasmonic excitations now becomes possible. Ultrafast electron microscopy via pulsed electron-emission in combination with EELS[175,232] and CL[233] enables investigations on the femtosecond timescale. Therefore, this is a quite promising technique to study the dynamics of propagating plasmonic modes. Besides the development of new, but often very complex technologies, also the combination of already existing possibilities can be used, such as tomographic EELS for the investigation of true 3D nanoscopic objects beyond rotational symmetry.[234]

Bibliography

[1] Robin Lingstädt, Nahid Talebi, Surong Guo, Wilfried Sigle, Alfredo Campos, Mathieu Kociak, Martin Esmann, Simon F. Becker, Eiji Okunishi, Masaki Mukai, Christoph Lienau, and Peter A. Van Aken. Probing plasmonic excitation mechanisms and far-field radiation of single-crystalline gold tapers with electrons. *Philosophical Transactions of the Royal Society A: Mathematical, Physical and Engineering Sciences*, 378(2186), 2020. doi: 10.1098/rsta.2019.0599rsta20190599.

[2] Robin Lingstädt, Nahid Talebi, Mario Hentschel, Soudabeh Mashhadi, Bruno Gompf, Marko Burghard, Harald Giessen, and Peter A. van Aken. Interaction of edge exciton polaritons with engineered defects in the hyperbolic material Bi_2Se_3. *Communications Materials*, 2(1):1–11, 2021. doi: 10.1038/s43246-020-00108-9.

[3] Michael Geiger, Robin Lingstädt, Tobias Wollandt, Julia Deuschle, Ute Zschieschang, Florian Letzkus, Joachim N. Burghartz, Peter A. Aken, R. Thomas Weitz, and Hagen Klauk. Subthreshold Swing of 59 mV decade^{-1} in Nanoscale Flexible Ultralow-Voltage Organic Transistors. *Advanced Electronic Materials*, 8(5):2101215, 2022. doi: 10.1002/aelm.202101215.

[4] S. A. Maier, M. L. Brongersma, P. G. Kik, S. Meltzer, A. A. G. Requicha, and H. A. Atwater. Plasmonics-A Route to Nanoscale Optical Devices. *Advanced Materials*, 13(19):1501–1505, 2001. doi: 10.1002/1521-4095(200110)13:19<1501::AID-ADMA1501>3.0.CO;2-Z.

[5] G. Ruthemann. Diskrete Energieverluste schneller Elektronen in Festkörpern. *Die Naturwissenschaften*, 29(42-43):648–648, 1941. doi: 10.1007/BF01485870.

[6] David Pines and David Bohm. A Collective Description of Electron Interactions: II. Collective vs Individual Particle Aspects of the Interactions. *Physical Review*, 85(2):338–353, 1952. doi: 10.1103/PhysRev.85.338.

[7] P. Nozières and D. Pines. Electron Interaction in Solids. Characteristic Energy Loss Spectrum. *Physical Review*, 113(5):1254–1267, 1959. doi: 10.1103/PhysRev.113.1254.

[8] R. H. Ritchie. Plasma Losses by Fast Electrons in Thin Films. *Physical Review*, 106(5):874–881, 1957. doi: 10.1103/PhysRev.106.874.

[9] C. J. Powell and J. B. Swan. Origin of the Characteristic Electron Energy Losses in Magnesium. *Physical Review*, 116(1):81–83, 1959. doi: 10.1103/PhysRev.116.81.

[10] C. J. Powell and J. B. Swan. Origin of the Characteristic Electron Energy Losses in Aluminum. *Physical Review*, 115(4):869–875, 1959. doi: 10.1103/PhysRev.115.869.

[11] R. H. Ritchie and A. Howie. Inelastic scattering probabilities in scanning transmission electron microscopy. *Philosophical Magazine A*, 58(5):753–767, 1988. doi: 10.1080/01418618808209951.

[12] F. Phillipp, R. Höschen, M. Osaki, G. Möbus, and M. Rühle. New high-voltage atomic resolution microscope approaching 1 Å point resolution installed in Stuttgart. *Ultramicroscopy*, 56(1-3):1–10, 1994. doi: 10.1016/0304-3991(94)90141-4.

[13] Jaysen Nelayah, Mathieu Kociak, Odile Stéphan, F. Javier García de Abajo, Marcel Tencé, Luc Henrard, Dario Taverna, Isabel Pastoriza-Santos, Luis M. Liz-Marzán, and Christian Colliex. Mapping surface plasmons on a single metallic nanoparticle. *Nature Physics*, 3(5):348–353, 2007. doi: 10.1038/nphys575.

[14] Michel Bosman, Vicki J. Keast, Masashi Watanabe, Abbas I. Maaroof, and Michael B. Cortie. Mapping surface plasmons at the nanometre scale with an electron beam. *Nanotechnology*, 18(16):165505, 2007. doi: 10.1088/0957-4484/18/16/165505.

[15] Wilfried Sigle, Jaysen Nelayah, Christoph T. Koch, and Peter A. van Aken. Electron energy losses in Ag nanoholes—from localized surface plasmon resonances to rings of fire. *Optics Letters*, 34(14):2150, 2009. doi: 10.1364/OL.34.002150.

[16] F. Javier García de Abajo. Nonlocal Effects in the Plasmons of Strongly Interacting Nanoparticles, Dimers, and Waveguides. *The Journal of Physical Chemistry C*, 112(46):17983–17987, 2008. doi: 10.1021/jp807345h.

[17] Javier Aizpurua and Alberto Rivacoba. Nonlocal effects in the plasmons of nanowires and nanocavities excited by fast electron beams. *Physical Review B*, 78(3):035404, 2008. doi: 10.1103/PhysRevB.78.035404.

[18] Ina Alber, Wilfried Sigle, Sven Müller, Reinhard Neumann, Oliver Picht, Markus Rauber, Peter A. van Aken, and Maria Eugenia Toimil-Molares.

Visualization of Multipolar Longitudinal and Transversal Surface Plasmon Modes in Nanowire Dimers. *ACS Nano*, 5(12):9845–9853, 2011. doi: 10.1021/nn2035044.

[19] Jean-Francois Masson. Portable and field-deployed surface plasmon resonance and plasmonic sensors. *The Analyst*, 145(11):3776–3800, 2020. doi: 10.1039/D0AN00316F.

[20] K. Lance Kelly, Eduardo Coronado, Lin Lin Zhao, and George C. Schatz. The Optical Properties of Metal Nanoparticles: The Influence of Size, Shape, and Dielectric Environment. *The Journal of Physical Chemistry B*, 107(3):668–677, 2003. doi: 10.1021/jp026731y.

[21] Andreas Otto. Excitation of nonradiative surface plasma waves in silver by the method of frustrated total reflection. *Zeitschrift für Physik A Hadrons and nuclei*, 216(4):398–410, 1968. doi: 10.1007/BF01391532.

[22] Erwin Kretschmann. Die Bestimmung optischer Konstanten von Metallen durch Anregung von Oberflächenplasmaschwingungen. *Zeitschrift für Physik A Hadrons and nuclei*, 241(4):313–324, 1971. doi: 10.1007/BF01395428.

[23] Louis De Broglie. Recherches sur la théorie des Quanta. *Physique. Migration - université en cours d'affectation*, HAL Id:(tel-00006807), 1924.

[24] C. J. Davisson and L. H. Germer. Reflection of Electrons by a Crystal of Nickel. *Proceedings of the National Academy of Sciences*, 14(4):317–322, 1928. doi: 10.1073/pnas.14.4.317.

[25] M. Knoll and E. Ruska. Das Elektronenmikroskop. *Zeitschrift für Physik*, 78(5-6):318–339, 1932. doi: 10.1007/BF01342199.

[26] Otto Scherzer. Über einige Fehler von Elektronenlinsen. *Zeitschrift für Physik*, 101(9-10):593–603, 1936. doi: 10.1007/BF01349606.

[27] Otto Scherzer. Sphärische und chromatische Korrektur von Elektronen-Linsen. *Optik*, 2:114–132, 1947.

[28] Harald Rose. Outline of a spherically corrected semiaplanatic medium-voltage transmission electron microscope. *Optik*, 85:19–24, 1990.

[29] Maximilian Haider, Stephan Uhlemann, Eugen Schwan, Harald Rose, Bernd Kabius, and Knut Urban. Electron microscopy image enhanced. *Nature*, 392(6678):768–769, 1998. doi: 10.1038/33823.

[30] Maximilian Haider, Harald Rose, Stephan Uhlemann, Eugen Schwan, Bernd Kabius, and Knut Urban. A spherical-aberration-corrected 200kV transmission electron microscope. *Ultramicroscopy*, 75(1):53–60, 1998. doi: 10.1016/S0304-3991(98)00048-5.

[31] David B. Williams and C. Barry Carter. *Transmission Electron Microscopy - A Textbook for Materials Science*. Springer, 2009. ISBN 978-0-387-76500-6.

[32] Stephen J. Pennycook and Peter D. Nellist. *Scanning Transmission Electron Microscopy: Imaging and Analysis*. Springer New York, New York, NY, 2011. ISBN 978-1-4419-7199-9. doi: 10.1007/978-1-4419-7200-2.

[33] James Hillier and R. F. Baker. Microanalysis by Means of Electrons. *Journal of Applied Physics*, 15(9):663–675, 1944. doi: 10.1063/1.1707491.

[34] B. Schaffer, K. Riegler, G. Kothleitner, W. Grogger, and F. Hofer. Monochromated, spatially resolved electron energy-loss spectroscopic measurements of gold nanoparticles in the plasmon range. *Micron*, 40(2): 269–273, 2009. doi: 10.1016/j.micron.2008.07.004.

[35] B. Rafferty and L. M. Brown. Direct and indirect transitions in the region of the band gap using electron-energy-loss spectroscopy. *Physical Review B*, 58(16):10326–10337, 1998. doi: 10.1103/PhysRevB.58.10326.

[36] M. Stöger-Pollach. Optical properties and bandgaps from low loss EELS: Pitfalls and solutions. *Micron*, 39(8):1092–1110, 2008. doi: 10.1016/j.micron.2008.01.023.

[37] T. Malis, S. C. Cheng, and R. F. Egerton. EELS log-ratio technique for specimen-thickness measurement in the TEM. *Journal of Electron Microscopy Technique*, 8(2):193–200, 1988. doi: 10.1002/jemt.1060080206.

[38] H. Hertz. Ueber einen Einfluss des ultravioletten Lichtes auf die electrische Entladung. *Annalen der Physik und Chemie*, 267(8):983–1000, 1887. doi: 10.1002/andp.18872670827.

[39] A. Einstein. Über einen die Erzeugung und Verwandlung des Lichtes betreffenden heuristischen Gesichtspunkt. *Annalen der Physik*, 322(6): 132–148, 1905. doi: 10.1002/andp.19053220607.

[40] F. J. García de Abajo. Optical excitations in electron microscopy. *Reviews of Modern Physics*, 82(1):209–275, 2010. doi: 10.1103/RevModPhys.82.209.

[41] Nahid Talebi. A directional, ultrafast and integrated few-photon source utilizing the interaction of electron beams and plasmonic nanoantennas.

New Journal of Physics, 16(5):053021, 2014. doi: 10.1088/1367-2630/16/5/053021.

[42] Nahid Talebi. Interaction of electron beams with optical nanostructures and metamaterials: from coherent photon sources towards shaping the wave function. *Journal of Optics*, 19(10):103001, 2017. doi: 10.1088/2040-8986/aa8041.

[43] Arthur Losquin and Mathieu Kociak. Link between Cathodoluminescence and Electron Energy Loss Spectroscopy and the Radiative and Full Electromagnetic Local Density of States. *ACS Photonics*, 2(11):1619–1627, 2015. doi: 10.1021/acsphotonics.5b00416.

[44] Arthur Losquin, Luiz F. Zagonel, Viktor Myroshnychenko, Benito Rodríguez-González, Marcel Tencé, Leonardo Scarabelli, Jens Förstner, Luis M. Liz-Marzán, F. Javier García de Abajo, Odile Stéphan, and Mathieu Kociak. Unveiling Nanometer Scale Extinction and Scattering Phenomena through Combined Electron Energy Loss Spectroscopy and Cathodoluminescence Measurements. *Nano Letters*, 15(2):1229–1237, 2015. doi: 10.1021/nl5043775.

[45] Naohiko Kawasaki, Sophie Meuret, Raphaël Weil, Hugo Lourenço-Martins, Odile Stéphan, and Mathieu Kociak. Extinction and Scattering Properties of High-Order Surface Plasmon Modes in Silver Nanoparticles Probed by Combined Spatially Resolved Electron Energy Loss Spectroscopy and Cathodoluminescence. *ACS Photonics*, 3(9):1654–1661, 2016. doi: 10.1021/acsphotonics.6b00257.

[46] Anna Tararan, Stefano di Sabatino, Matteo Gatti, Takashi Taniguchi, Kenji Watanabe, Lucia Reining, Luiz H. G. Tizei, Mathieu Kociak, and

Alberto Zobelli. Optical gap and optically active intragap defects in cubic BN. *Physical Review B*, 98(9):094106, 2018. doi: 10.1103/PhysRevB.98.094106.

[47] Surong Guo, Nahid Talebi, Alfredo Campos, Mathieu Kociak, and Peter A. van Aken. Radiation of Dynamic Toroidal Moments. *ACS Photonics*, 6 (2):467–474, 2019. doi: 10.1021/acsphotonics.8b01422.

[48] Ernst Jan R. Vesseur, René de Waele, Martin Kuttge, and Albert Polman. Direct Observation of Plasmonic Modes in Au Nanowires Using High-Resolution Cathodoluminescence Spectroscopy. *Nano Letters*, 7(9):2843–2846, 2007. doi: 10.1021/nl071480w.

[49] M. Kociak and L.F. Zagonel. Cathodoluminescence in the scanning transmission electron microscope. *Ultramicroscopy*, 176:112–131, 2017. doi: 10.1016/j.ultramic.2017.03.014.

[50] Ming-Wen Chu, Viktor Myroshnychenko, Cheng Hsuan Chen, Jing-Pei Deng, Chung-Yuan Mou, and F. Javier García de Abajo. Probing Bright and Dark Surface-Plasmon Modes in Individual and Coupled Noble Metal Nanoparticles Using an Electron Beam. *Nano Letters*, 9(1):399–404, 2009. doi: 10.1021/nl803270x.

[51] Nahid Talebi, Wilfried Sigle, Ralf Vogelgesang, Christoph T. Koch, Cristina Fernández-López, Luis M. Liz-Marzán, Burcu Ögüt, Melanie Rohm, and Peter A. van Aken. Breaking the Mode Degeneracy of Surface Plasmon Resonances in a Triangular System. *Langmuir*, 28(24): 8867–8873, 2012. doi: 10.1021/la3001762.

[52] Burcu Ögüt, Nahid Talebi, Ralf Vogelgesang, Wilfried Sigle, and Peter A. van Aken. Toroidal Plasmonic Eigenmodes in Oligomer Nanocavities

for the Visible. *Nano Letters*, 12(10):5239–5244, 2012. doi: 10.1021/nl302418n.

[53] Steven J. Barrow, David Rossouw, Alison M. Funston, Gianluigi A. Botton, and Paul Mulvaney. Mapping Bright and Dark Modes in Gold Nanoparticle Chains using Electron Energy Loss Spectroscopy. *Nano Letters*, 14(7):3799–3808, 2014. doi: 10.1021/nl5009053.

[54] Benjamin J. M. Brenny, Albert Polman, and F. Javier García de Abajo. Femtosecond plasmon and photon wave packets excited by a high-energy electron on a metal or dielectric surface. *Physical Review B*, 94(15): 155412, 2016. doi: 10.1103/PhysRevB.94.155412.

[55] F. J. García de Abajo, A Rivacoba, N Zabala, and N Yamamoto. Boundary effects in Cherenkov radiation. *Physical Review B*, 69(15):155420, 2004. ISSN 1098-0121. doi: 10.1103/PhysRevB.69.155420.

[56] F. J. García de Abajo and M. Kociak. Probing the Photonic Local Density of States with Electron Energy Loss Spectroscopy. *Physical Review Letters*, 100(10):106804, 2008. doi: 10.1103/PhysRevLett.100.106804.

[57] R. W. Schoenlein, W. Z. Lin, J. G. Fujimoto, and G. L. Eesley. Femtosecond studies of nonequilibrium electronic processes in metals. *Physical Review Letters*, 58(16):1680–1683, 1987. doi: 10.1103/PhysRevLett.58.1680.

[58] Xinping Zhang, Cuiying Huang, Meng Wang, Pei Huang, Xinkui He, and Zhiyi Wei. Transient localized surface plasmon induced by femtosecond interband excitation in gold nanoparticles. *Scientific Reports*, 8(1):10499, 2018. doi: 10.1038/s41598-018-28909-6.

[59] Kenan Elibol and Peter A. van Aken. Uncovering the Evolution of Low-Energy Plasmons in Nanopatterned Aluminum Plasmonics on Graphene. *Nano Letters*, 22(14):5825–5831, 2022. doi: 10.1021/acs.nanolett.2c01512.

[60] P. G. Etchegoin, E. C. Le Ru, and M. Meyer. An analytic model for the optical properties of gold. *Journal of Chemical Physics*, 125(16): 2004–2007, 2006. doi: 10.1063/1.2360270.

[61] Desheng Kong, Jason C. Randel, Hailin Peng, Judy J. Cha, Stefan Meister, Keji Lai, Yulin Chen, Zhi Xun Shen, Hari C. Manoharan, and Yi Cui. Topological insulator nanowires and nanoribbons. *Nano Letters*, 10(1): 329–333, 2010. doi: 10.1021/nl903663a.

[62] Desheng Kong, Wenhui Dang, Judy J. Cha, Hui Li, Stefan Meister, Hailin Peng, Zhongfan Liu, and Yi Cui. Few-layer nanoplates of Bi2Se3 and Bi 2Te3 with highly tunable chemical potential. *Nano Letters*, 10(6): 2245–2250, 2010. doi: 10.1021/nl101260j.

[63] P. Gehring, M. Burghard, and K. Kern. Gate-controlled linear magnetoresistance in thin Bi2 Se3 sheets. *Applied Physics Letters*, 100(21):212402, 2012. doi: 10.1063/1.4719196.

[64] Andres Castellanos-Gomez, Michele Buscema, Rianda Molenaar, Vibhor Singh, Laurens Janssen, Herre S J van der Zant, and Gary A. Steele. Deterministic transfer of two-dimensional materials by all-dry viscoelastic stamping. *2D Materials*, 1(1):011002, 2014. doi: 10.1088/2053-1583/1/1/011002.

[65] Slawa Schmidt, Björn Piglosiewicz, Diyar Sadiq, Javid Shirdel, Jae Sung Lee, Parinda Vasa, Namkyoo Park, Dai-Sik Kim, and Christoph Lienau. Adiabatic Nanofocusing on Ultrasmooth Single-Crystalline Gold Tapers

Creates a 10-nm-Sized Light Source with Few-Cycle Time Resolution. *ACS Nano*, 6(7):6040–6048, 2012. doi: 10.1021/nn301121h.

[66] D. Roy, C. M. Williams, and K. Mingard. Single-crystal gold tip for tip-enhanced Raman spectroscopy. *Journal of Vacuum Science & Technology B, Nanotechnology and Microelectronics: Materials, Processing, Measurement, and Phenomena*, 28(3):631–634, 2010. doi: 10.1116/1.3425630.

[67] Debdulal Roy, Jian Wang, and M. E. Welland. Nanoscale imaging of carbon nanotubes using tip enhanced Raman spectroscopy in reflection mode. *Faraday Discussions*, 132:215–225, 2006. doi: 10.1039/b506365e.

[68] Bin Ren, Gennaro Picardi, and Bruno Pettinger. Preparation of gold tips suitable for tip-enhanced Raman spectroscopy and light emission by electrochemical etching. *Review of Scientific Instruments*, 75(4):837–841, 2004. doi: 10.1063/1.1688442.

[69] Surong Guo, Nahid Talebi, Wilfried Sigle, Ralf Vogelgesang, Gunther Richter, Martin Esmann, Simon F. Becker, Christoph Lienau, and Peter A. van Aken. Reflection and Phase Matching in Plasmonic Gold Tapers. *Nano Letters*, 16(10):6137–6144, 2016. doi: 10.1021/acs.nanolett.6b02353.

[70] Surong Guo, Nahid Talebi, Alfredo Campos, Wilfried Sigle, Martin Esmann, Simon F Becker, Christoph Lienau, Mathieu Kociak, and Peter A. van Aken. Far-Field Radiation of Three-Dimensional Plasmonic Gold Tapers near Apexes. *ACS Photonics*, 6(10):2509–2516, 2019. ISSN 2330-4022. doi: 10.1021/acsphotonics.9b00838.

[71] Joachim P. Spatz, Stefan Mössmer, Christoph Hartmann, Martin Möller, Thomas Herzog, Michael Krieger, Hans Gerd Boyen, Paul Ziemann, and

Bernd Kabius. Ordered deposition of inorganic clusters from micellar block copolymer films. *Langmuir*, 16(2):407–415, 2000. doi: 10.1021/la990070n.

[72] Roman Glass, Martin Möller, and Joachim P. Spatz. Block copolymer micelle nanolithography. *Nanotechnology*, 14(10):1153–1160, 2003. doi: 10.1088/0957-4484/14/10/314.

[73] Niels O. Young and Jakym Kowal. Optically Active Fluorite Films. *Nature*, 183(4654):104–105, 1959. doi: 10.1038/183104a0.

[74] D. Vick, L.J. Friedrich, S.K. Dew, M.J. Brett, K. Robbie, M. Seto, and T. Smy. Self-shadowing and surface diffusion effects in obliquely deposited thin films. *Thin Solid Films*, 339(1-2):88–94, 1999. doi: 10.1016/S0040-6090(98)01154-7.

[75] Andrew G. Mark, John G. Gibbs, Tung Chun Lee, and Peer Fischer. Hybrid nanocolloids with programmed three-dimensional shape and material composition. *Nature Materials*, 12(9):802–807, 2013. doi: 10.1038/nmat3685.

[76] John G. Gibbs, Andrew G. Mark, Tung Chun Lee, Sahand Eslami, Debora Schamel, and Peer Fischer. Nanohelices by shadow growth. *Nanoscale*, 6 (16):9457–9466, 2014. doi: 10.1039/c4nr00403e.

[77] Christoph T Koch, Wilfried Sigle, Rainer Höschen, Manfred Rühle, Erik Essers, Gerd Benner, and Marko Matijevic. SESAM: Exploring the Frontiers of Electron Microscopy. *Microscopy and Microanalysis*, 12(6): 506–514, 2006. doi: 10.1017/S1431927606060624.

[78] Erik Essers, Gerd Benner, Thilo Mandler, Stefan Meyer, Dieter Mittmann, Michael Schnell, and Rainer Höschen. Energy resolution of an Omega-type monochromator and imaging properties of the MANDOLINE filter. *Ultramicroscopy*, 110:971–980, 2010. doi: 10.1016/j.ultramic.2010.02.009.

[79] Ondrej L Krivanek, Tracy C Lovejoy, Niklas Dellby, Toshihiro Aoki, R W Carpenter, Peter Rez, Emmanuel Soignard, Jiangtao Zhu, Philip E Batson, Maureen J Lagos, Ray F Egerton, and Peter A Crozier. Vibrational spectroscopy in the electron microscope. *Nature*, 514(7521):209–212, 2014. doi: 10.1038/nature13870.

[80] Toon Coenen, Ernst Jan R. Vesseur, and Albert Polman. Angle-resolved cathodoluminescence spectroscopy. *Applied Physics Letters*, 99(14): 143103, 2011. doi: 10.1063/1.3644985.

[81] Toon Coenen, Ernst Jan R. Vesseur, Albert Polman, and A. Femius Koenderink. Directional Emission from Plasmonic Yagi–Uda Antennas Probed by Angle-Resolved Cathodoluminescence Spectroscopy. *Nano Letters*, 11(9):3779–3784, 2011. doi: 10.1021/nl201839g.

[82] Clara I. Osorio, Toon Coenen, Benjamin J. M. Brenny, Albert Polman, and A. Femius Koenderink. Angle-Resolved Cathodoluminescence Imaging Polarimetry. *ACS Photonics*, 3(1):147–154, 2016. doi: 10.1021/acsphotonics.5b00596.

[83] Delmic. Polarization-Filtered Cathodoluminescence Imaging. *technical note*, sparc spec(V01-01 2021-15-11), 2021.

[84] Dan E. Dudgeon and Russell M. Mersereau. *Multidimensional digital signal processing*. Prentice-Hall, 1984.

[85] G Binnig. Atomic force microscope and method for imaging surfaces with atomic resolution. *US Patent*, 4724318, 1986. URL `www.patentstorm.us/patents/4724318.html`.

[86] G. Binnig, C. F. Quate, and Ch. Gerber. Atomic Force Microscope. *Physical Review Letters*, 56(9):930–933, 1986. doi: 10.1103/PhysRevLett.56.930.

[87] Gerd Binnig and Heinrich Rohrer. Scanning tunneling microscope. *US Patent*, 4343993, 1980.

[88] G. Binnig and H. Rohrer. Scanning tunneling microscopy. *Surface Science*, 126(1-3):236–244, 1983. doi: 10.1016/0039-6028(83)90716-1.

[89] Augustin-Jean Fresnel. Note sur le calcul des teintes que la polarisation développe dans les lames cristallisées. *Annales de chimie et physique*, 17:101–112, 1821.

[90] Wilhelm Haidinger. Ueber den Pleochroismus des Amethysts. *Annalen der Physik und Chemie*, 70:531–544, 1847.

[91] A. Cotton. Recherches sur l'absorption et la dispersion de la lumière par les milieux doués du pouvoir rotatoire. *Journal de Physique Théorique et Appliquée*, 5(1):237–244, 1896. doi: 10.1051/jphystap:018960050023700.

[92] Jean-Baptiste Biot. Mémoire sur les Rotations que Certaines Substances Impriment aux Axes de Polarisation des Rayons Lumineux. *Mém. Acad. Roy.*, 41(2):2, 1817.

[93] Neil Purdie and Kathy A. Swallows. Analytical Applications of Polarimetry, Optical Rotatory Dispersion, and Circular Dichroism. *Analytical chemistry*, 61(2):77A–89A, 1989.

[94] Laurien I. Roest, Sabrya E. van Heijst, Louis Maduro, Juan Rojo, and Sonia Conesa-Boj. Charting the low-loss region in electron energy loss spectroscopy with machine learning. *Ultramicroscopy*, 222(September 2020):113202, 2021. doi: 10.1016/j.ultramic.2021.113202.

[95] Karl Pearson. LIII. On lines and planes of closest fit to systems of points in space. *The London, Edinburgh, and Dublin Philosophical Magazine and Journal of Science*, 2(11):559–572, 1901. doi: 10.1080/14786440109462720.

[96] Stijn Lichtert and Jo Verbeeck. Statistical consequences of applying a PCA noise filter on EELS spectrum images. *Ultramicroscopy*, 125(2013): 35–42, 2013. doi: 10.1016/j.ultramic.2012.10.001.

[97] David Pile. Numerical solution. *Nature Photonics*, 9(1):5–6, 2015. doi: 10.1038/nphoton.2014.305.

[98] Ming-yun Chen, Sen-ming Hsu, and Hung-Chun Chang. A finite-difference frequency-domain method for full-vectroial mode solutions of anisotropic optical waveguides with arbitrary permittivity tensor. *Optics Express*, 17 (8):5965, 2009. doi: 10.1364/OE.17.005965.

[99] Shaista Babar and J. H. Weaver. Optical constants of Cu, Ag, and Au revisited. *Applied Optics*, 54(3):477, 2015. doi: 10.1364/AO.54.000477.

[100] Ulrich Hohenester. Simulating electron energy loss spectroscopy with the MNPBEM toolbox. *Computer Physics Communications*, 185(3): 1177–1187, 2014. doi: 10.1016/j.cpc.2013.12.010.

[101] Meng Zhao, Michel Bosman, Mohammad Danesh, Minggang Zeng, Peng Song, Yudi Darma, Andrivo Rusydi, Hsin Lin, Cheng-Wei Qiu,

and Kian Ping Loh. Visible Surface Plasmon Modes in Single Bi_2Te_3 Nanoplate. *Nano Letters*, 15(12):8331–8335, 2015. doi: 10.1021/acs.nanolett.5b03966.

[102] Yury Deshko, Lia Krusin-Elbaum, Vinod Menon, Alexander Khanikaev, and Jacob Trevino. Surface plasmon polaritons in topological insulator nano-films and superlattices. *Optics Express*, 24(7):7398, 2016. doi: 10.1364/OE.24.007398.

[103] Nahid Talebi, Cigdem Ozsoy-Keskinbora, Hadj M. Benia, Klaus Kern, Christoph T. Koch, and Peter A. van Aken. Wedge Dyakonov Waves and Dyakonov Plasmons in Topological Insulator Bi_2Se_3 Probed by Electron Beams. *ACS Nano*, 10(7):6988–6994, 2016. doi: 10.1021/acsnano.6b02968.

[104] E. V. Calman, M. M. Fogler, L. V. Butov, S. Hu, A. Mishchenko, and A. K. Geim. Indirect excitons in van der Waals heterostructures at room temperature. *Nature Communications*, 9(1):1895, 2018. doi: 10.1038/s41467-018-04293-7.

[105] D. S. Chemla and D. A. B. Miller. Room-temperature excitonic nonlinear-optical effects in semiconductor quantum-well structures. *Journal of the Optical Society of America B*, 2(7):1155, 1985. doi: 10.1364/JOSAB.2.001155.

[106] A. K. Geim and I. V. Grigorieva. Van der Waals heterostructures. *Nature*, 499(7459):419–425, 2013. doi: 10.1038/nature12385.

[107] D. N. Basov, M. M. Fogler, and F. J. García de Abajo. Polaritons in van der Waals materials. *Science*, 354(6309):aag1992–1–aag1992–8, 2016. doi: 10.1126/science.aag1992.

[108] Tony Low, Andrey Chaves, Joshua D. Caldwell, Anshuman Kumar, Nicholas X. Fang, Phaedon Avouris, Tony F Heinz, Francisco Guinea, Luis Martin-Moreno, and Frank Koppens. Polaritons in layered two-dimensional materials. *Nature Materials*, 16(2):182–194, 2017. doi: 10.1038/nmat4792.

[109] Vincenzo Ardizzone, Luisa De Marco, Milena De Giorgi, Lorenzo Dominici, Dario Ballarini, and Daniele Sanvitto. Emerging 2D materials for room-temperature polaritonics. *Nanophotonics*, 8(9):1547–1558, 2019. doi: 10.1515/nanoph-2019-0114.

[110] Iann C. Gerber, Emmanuel Courtade, Shivangi Shree, Cedric Robert, Takashi Taniguchi, Kenji Watanabe, Andrea Balocchi, Pierre Renucci, Delphine Lagarde, Xavier Marie, and Bernhard Urbaszek. Interlayer excitons in bilayer MoS_2 with strong oscillator strength up to room temperature. *Physical Review B*, 99(3):035443, 2019. doi: 10.1103/PhysRevB.99.035443.

[111] K.L. Shlager and J.B. Schneider. A selective survey of the finite-difference time-domain literature. *IEEE Antennas and Propagation Magazine*, 37 (4):39–57, 1995. doi: 10.1109/74.414731.

[112] Osamu Takayama and Andrei V. Lavrinenko. Optics with hyperbolic materials. *Journal of the Optical Society of America B*, 36(8):F38, 2019. doi: 10.1364/JOSAB.36.000F38.

[113] Zubin Jacob and Evgenii E. Narimanov. Optical hyperspace for plasmons: Dyakonov states in metamaterials. *Applied Physics Letters*, 93(22):221109, 2008. doi: 10.1063/1.3037208.

[114] Jie Yao, Zhaowei Liu, Yongmin Liu, Yuan Wang, Cheng Sun, Guy Bartal, Angelica M. Stacy, and Xiang Zhang. Optical negative refraction in bulk metamaterials of nanowires. *Science*, 321(5891):930, 2008. doi: 10.1126/science.1157566.

[115] Zubin Jacob, Leonid V. Alekseyev, and Evgenii Narimanov. Optical Hyperlens: Far-field imaging beyond the diffraction limit. *Optics Express*, 14(18):8247, 2006. doi: 10.1364/OE.14.008247.

[116] Zhaowei Liu, Hyesog Lee, Yi Xiong, Cheng Sun, and Xiang Zhang. Far-Field Optical Hyperlens Magnifying Sub-Diffraction-Limited Objects. *Science*, 315(5819):1686–1686, 2007. doi: 10.1126/science.1137368.

[117] Igor I. Smolyaninov, Yu-Ju Hung, and Christopher C. Davis. Magnifying Superlens in the Visible Frequency Range. *Science*, 315(5819):1699–1701, 2007. doi: 10.1126/science.1138746.

[118] Peining Li, Martin Lewin, Andrey V. Kretinin, Joshua D. Caldwell, Kostya S. Novoselov, Takashi Taniguchi, Kenji Watanabe, Fabian Gaussmann, and Thomas Taubner. Hyperbolic phonon-polaritons in boron nitride for near-field optical imaging and focusing. *Nature Communications*, 6(7507):1–9, 2015. doi: 10.1038/ncomms8507.

[119] R. K. Fisher. Resonance Cones in the Field Pattern of a Radio Frequency Probe in a Warm Anisotropic Plasma. *Physics of Fluids*, 14(4):857, 1971. doi: 10.1063/1.1693521.

[120] Alexander Poddubny, Ivan Iorsh, Pavel Belov, and Yuri Kivshar. Hyperbolic metamaterials. *Nature Photonics*, 7(12):948–957, 2013. doi: 10.1038/nphoton.2013.243.

[121] Vladimir P. Drachev, Viktor A. Podolskiy, and Alexander V. Kildishev. Hyperbolic metamaterials: new physics behind a classical problem. *Optics Express*, 21(12):15048, 2013. doi: 10.1364/OE.21.015048.

[122] Maryam Mahmoodi, Seyed Hassan Tavassoli, Osamu Takayama, Johneph Sukham, Radu Malureanu, and Andrei V. Lavrinenko. Existence Conditions of High-k Modes in Finite Hyperbolic Metamaterials. *Laser & Photonics Reviews*, 13(3):1800253, 2019. doi: 10.1002/lpor.201800253.

[123] Jon A. Schuller, Rashid Zia, Thomas Taubner, and Mark L. Brongersma. Dielectric Metamaterials Based on Electric and Magnetic Resonances of Silicon Carbide Particles. *Physical Review Letters*, 99(10):107401, 2007. doi: 10.1103/PhysRevLett.99.107401.

[124] Jingbo Sun, Ji Zhou, Bo Li, and Feiyu Kang. Indefinite permittivity and negative refraction in natural material: Graphite. *Applied Physics Letters*, 98(10):101901, 2011. doi: 10.1063/1.3562033.

[125] M. N. Gjerding, R. Petersen, T. G. Pedersen, N. A. Mortensen, and K. S. Thygesen. Layered van der Waals crystals with hyperbolic light dispersion. *Nature Communications*, 8(1):320, 2017. doi: 10.1038/s41467-017-00412-y.

[126] Leonid V. Alekseyev, Viktor A. Podolskiy, and Evgenii E. Narimanov. Homogeneous Hyperbolic Systems for Terahertz and Far-Infrared Frequencies. *Advances in OptoElectronics*, 2012:1–6, 2012. doi: 10.1155/2012/267564.

[127] Joshua D. Caldwell, Andrey V. Kretinin, Yiguo Chen, Vincenzo Giannini, Michael M. Fogler, Yan Francescato, Chase T. Ellis, Joseph G. Tischler, Colin R. Woods, Alexander J. Giles, Minghui Hong, Kenji Watanabe,

Takashi Taniguchi, Stefan A. Maier, and Kostya S. Novoselov. Sub-diffractional volume-confined polaritons in the natural hyperbolic material hexagonal boron nitride. *Nature Communications*, 5(1):5221, 2014. doi: 10.1038/ncomms6221.

[128] S. Dai, Z. Fei, Q. Ma, A. S. Rodin, M. Wagner, A. S. McLeod, M. K. Liu, W. Gannett, W. Regan, K. Watanabe, T. Taniguchi, M. Thiemens, G. Dominguez, A. H. Castro Neto, A. Zettl, F. Keilmann, P. Jarillo-Herrero, M. M. Fogler, and D. N. Basov. Tunable Phonon Polaritons in Atomically Thin van der Waals Crystals of Boron Nitride. *Science*, 343 (6175):1125–1129, 2014. doi: 10.1126/science.1246833.

[129] Jhih-Sheng Wu, D. N. Basov, and M. M. Fogler. Topological insulators are tunable waveguides for hyperbolic polaritons. *Physical Review B*, 92 (20):205430, 2015. doi: 10.1103/PhysRevB.92.205430.

[130] Moritz Esslinger, Ralf Vogelgesang, Nahid Talebi, Worawut Khunsin, Pascal Gehring, Stefano de Zuani, Bruno Gompf, and Klaus Kern. Tetradymites as Natural Hyperbolic Materials for the Near-Infrared to Visible. *ACS Photonics*, 1(12):1285–1289, 2014. doi: 10.1021/ph500296e.

[131] Tobias Stauber. Plasmonics in Dirac systems: from graphene to topological insulators. *Journal of Physics: Condensed Matter*, 26(12):123201, 2014. doi: 10.1088/0953-8984/26/12/123201.

[132] Haijun Zhang, Chao-Xing Liu, Xiao-Liang Qi, Xi Dai, Zhong Fang, and Shou-Cheng Zhang. Topological insulators in Bi_2Se_3, Bi_2Te_3 and Sb_2Te_3 with a single Dirac cone on the surface. *Nature Physics*, 5(6):438–442, 2009. doi: 10.1038/nphys1270.

[133] Andrea Splendiani, Liang Sun, Yuanbo Zhang, Tianshu Li, Jonghwan Kim, Chi-Yung Chim, Giulia Galli, and Feng Wang. Emerging Photoluminescence in Monolayer MoS_2. *Nano Letters*, 10(4):1271–1275, 2010. doi: 10.1021/nl903868w.

[134] J. Lecante, Y. Ballu, and D. M. Newns. Electron-Surface-Plasmon Scattering Using a Parabolic Nontouching Trajectory. *Physical Review Letters*, 38(1):36–40, 1977. doi: 10.1103/PhysRevLett.38.36.

[135] D. F. P. Pile, T. Ogawa, D. K. Gramotnev, T. Okamoto, M. Haraguchi, M. Fukui, and S. Matsuo. Theoretical and experimental investigation of strongly localized plasmons on triangular metal wedges for subwavelength waveguiding. *Applied Physics Letters*, 87(6):061106, 2005. doi: 10.1063/1.1991990.

[136] P. Li, I. Dolado, F. J. Alfaro-Mozaz, A. Yu Nikitin, F. Casanova, L. E. Hueso, S. Vélez, and R. Hillenbrand. Optical Nanoimaging of Hyperbolic Surface Polaritons at the Edges of van der Waals Materials. *Nano Letters*, 17(1):228–235, 2017. doi: 10.1021/acs.nanolett.6b03920.

[137] J. B. Pendry, A. Aubry, D. R. Smith, and S. A. Maier. Transformation Optics and Subwavelength Control of Light. *Science*, 337(6094):549–552, 2012. doi: 10.1126/science.1220600.

[138] Nanfang Yu and Federico Capasso. Flat optics with designer metasurfaces. *Nature Materials*, 13(2):139–150, 2014. doi: 10.1038/nmat3839.

[139] J. S. Gomez-Diaz and Andrea Alù. Flatland Optics with Hyperbolic Metasurfaces. *ACS Photonics*, 3(12):2211–2224, 2016. doi: 10.1021/acsphotonics.6b00645.

[140] M. I. D'yakonov. New type of electromagnetic wave propagating at an interface. *Sov. Phys. JETP*, 67(4):714–716, 1988.

[141] Alexander A. Govyadinov, Andrea Konečná, Andrey Chuvilin, Saül Vélez, Irene Dolado, Alexey Y. Nikitin, Sergei Lopatin, Fèlix Casanova, Luis E. Hueso, Javier Aizpurua, and Rainer Hillenbrand. Probing low-energy hyperbolic polaritons in van der Waals crystals with an electron microscope. *Nature Communications*, 8(1):95, 2017. doi: 10.1038/s41467-017-00056-y.

[142] A. J. Babadjanyan, N. L. Margaryan, and Kh V. Nerkararyan. Superfocusing of surface polaritons in the conical structure. *Journal of Applied Physics*, 87(8):3785–3788, 2000. doi: 10.1063/1.372414.

[143] Mark I. Stockman. Nanofocusing of Optical Energy in Tapered Plasmonic Waveguides. *Physical Review Letters*, 93(13):137404, 2004. doi: 10.1103/PhysRevLett.93.137404.

[144] Surbhi Lal, Stephan Link, and Naomi J. Halas. Nano-optics from sensing to waveguiding. *Nature Photonics*, 1(11):641–648, 2007. doi: 10.1038/nphoton.2007.223.

[145] Lukas Novotny and Niek van Hulst. Antennas for light. *Nature Photonics*, 5(2):83–90, 2011. doi: 10.1038/nphoton.2010.237.

[146] Dmitri K. Gramotnev and Sergey I. Bozhevolnyi. Nanofocusing of electromagnetic radiation. *Nature Photonics*, 8(1):13–22, 2014. doi: 10.1038/nphoton.2013.232.

[147] J.-C. Weeber, J. R. Krenn, A. Dereux, B. Lamprecht, Y. Lacroute, and J. P. Goudonnet. Near-field observation of surface plasmon polariton

propagation on thin metal stripes. *Physical Review B*, 64(4):045411, 2001. doi: 10.1103/PhysRevB.64.045411.

[148] D. S. Kim, S. C. Hohng, V. Malyarchuk, Y. C. Yoon, Y. H. Ahn, K. J. Yee, J. W. Park, J. Kim, Q. H. Park, and C. Lienau. Microscopic Origin of Surface-Plasmon Radiation in Plasmonic Band-Gap Nanostructures. *Physical Review Letters*, 91(14):143901, 2003. doi: 10.1103/PhysRevLett.91.143901.

[149] William L. Barnes. Surface plasmon–polariton length scales: a route to sub-wavelength optics. *Journal of Optics A: Pure and Applied Optics*, 8 (4):S87–S93, 2006. doi: 10.1088/1464-4258/8/4/S06.

[150] Sergey I. Bozhevolnyi, Valentyn S. Volkov, Eloïse Devaux, Jean-Yves Laluet, and Thomas W. Ebbesen. Channel plasmon subwavelength waveguide components including interferometers and ring resonators. *Nature*, 440(7083):508–511, 2006. doi: 10.1038/nature04594.

[151] Yusheng Bian, Zheng Zheng, Ya Liu, Jiansheng Liu, Jinsong Zhu, and Tao Zhou. Hybrid wedge plasmon polariton waveguide with good fabrication-error-tolerance for ultra-deep-subwavelength mode confinement. *Optics Express*, 19(23):22417, 2011. doi: 10.1364/OE.19.022417.

[152] Lin Gu, Wilfried Sigle, Christoph T. Koch, Burcu Ögüt, Peter A. van Aken, Nahid Talebi, Ralf Vogelgesang, Jianlin Mu, Xiaogang Wen, and Jian Mao. Resonant wedge-plasmon modes in single-crystalline gold nanoplatelets. *Physical Review B*, 83(19):195433, 2011. doi: 10.1103/PhysRevB.83.195433.

[153] Ewold Verhagen, Albert Polman, and L. (Kobus) Kuipers. Nanofocusing in laterally tapered plasmonic waveguides. *Optics Express*, 16(1):45, 2008. doi: 10.1364/OE.16.000045.

[154] C. Ropers, C. C. Neacsu, T. Elsaesser, M. Albrecht, M. B. Raschke, and C. Lienau. Grating-Coupling of Surface Plasmons onto Metallic Tips: A Nanoconfined Light Source. *Nano Letters*, 7(9):2784–2788, 2007. doi: 10.1021/nl071340m.

[155] Catalin C. Neacsu, Samuel Berweger, Robert L. Olmon, Laxmikant V. Saraf, Claus Ropers, and Markus B. Raschke. Near-Field Localization in Plasmonic Superfocusing: A Nanoemitter on a Tip. *Nano Letters*, 10(2): 592–596, 2010. doi: 10.1021/nl903574a.

[156] Diyar Sadiq, Javid Shirdel, Jae Sung Lee, Elena Selishcheva, Namkyoo Park, and Christoph Lienau. Adiabatic Nanofocusing Scattering-Type Optical Nanoscopy of Individual Gold Nanoparticles. *Nano Letters*, 11 (4):1609–1613, 2011. doi: 10.1021/nl1045457.

[157] Samuel Berweger, Joanna M. Atkin, Robert L. Olmon, and Markus B. Raschke. Light on the Tip of a Needle: Plasmonic Nanofocusing for Spectroscopy on the Nanoscale. *The Journal of Physical Chemistry Letters*, 3(7):945–952, 2012. doi: 10.1021/jz2016268.

[158] Nathan C. Lindquist, Jincy Jose, Sudhir Cherukulappurath, Xiaoshu Chen, Timothy W. Johnson, and Sang-Hyun Oh. Tip-based plasmonics: squeezing light with metallic nanoprobes. *Laser & Photonics Reviews*, 7 (4):453–477, 2013. doi: 10.1002/lpor.201209044.

[159] Petra Groß, Martin Esmann, Simon F. Becker, Jan Vogelsang, Nahid Talebi, and Christoph Lienau. Plasmonic nanofocusing – grey holes for

light. *Advances in Physics: X*, 1(2):297–330, 2016. doi: 10.1080/23746149.2016.1177469.

[160] Takayuki Umakoshi, Yuika Saito, and Prabhat Verma. Highly efficient plasmonic tip design for plasmon nanofocusing in near-field optical microscopy. *Nanoscale*, 8(10):5634–5640, 2016. doi: 10.1039/C5NR08548A.

[161] Zhi-Yuan Li. Mesoscopic and Microscopic Strategies for Engineering Plasmon-Enhanced Raman Scattering. *Advanced Optical Materials*, 6 (16):1701097, 2018. doi: 10.1002/adom.201701097.

[162] Xuezhi Ma, Yangzhi Zhu, Ning Yu, Sanggon Kim, Qiushi Liu, Leonard Apontti, Da Xu, Ruoxue Yan, and Ming Liu. Toward High-Contrast Atomic Force Microscopy-Tip-Enhanced Raman Spectroscopy Imaging: Nanoantenna-Mediated Remote-Excitation on Sharp-Tip Silver Nanowire Probes. *Nano Letters*, 19(1):100–107, 2019. doi: 10.1021/acs.nanolett.8b03399.

[163] Martin Esmann, Simon Fabian Becker, Julia Witt, Jinxin Zhan, Abbas Chimeh, Anke Korte, Jinhui Zhong, Ralf Vogelgesang, Gunther Wittstock, and Christoph Lienau. Vectorial near-field coupling. *Nature Nanotechnology*, 14(7):698–704, 2019. doi: 10.1038/s41565-019-0441-y.

[164] C. Ropers, D. R. Solli, C. P. Schulz, C. Lienau, and T. Elsaesser. Localized Multiphoton Emission of Femtosecond Electron Pulses from Metal Nanotips. *Physical Review Letters*, 98(4):043907, 2007. doi: 10.1103/PhysRevLett.98.043907.

[165] Melanie Müller, Alexander Paarmann, and Ralph Ernstorfer. Femtosecond electrons probing currents and atomic structure in nanomaterials. *Nature Communications*, 5(1):5292, 2014. doi: 10.1038/ncomms6292.

[166] Jan Vogelsang, Jörg Robin, Benedek J. Nagy, Péter Dombi, Daniel Rosenkranz, Manuela Schiek, Petra Groß, and Christoph Lienau. Ultrafast Electron Emission from a Sharp Metal Nanotaper Driven by Adiabatic Nanofocusing of Surface Plasmons. *Nano Letters*, 15(7):4685–4691, 2015. doi: 10.1021/acs.nanolett.5b01513.

[167] Benjamin Schröder, Thorsten Weber, Sergey V. Yalunin, Thomas Kiel, Christian Matyssek, Murat Sivis, Sascha Schäfer, Felix von Cube, Stephan Irsen, Kurt Busch, Claus Ropers, and Stefan Linden. Real-space imaging of nanotip plasmons using electron energy loss spectroscopy. *Physical Review B*, 92(8):085411, 2015. doi: 10.1103/PhysRevB.92.085411.

[168] Melanie Müller, Vasily Kravtsov, Alexander Paarmann, Markus B. Raschke, and Ralph Ernstorfer. Nanofocused Plasmon-Driven Sub-10 fs Electron Point Source. *ACS Photonics*, 3(4):611–619, 2016. doi: 10.1021/acsphotonics.5b00710.

[169] Sha Li and R. R. Jones. High-energy electron emission from metallic nano-tips driven by intense single-cycle terahertz pulses. *Nature Communications*, 7(1):13405, 2016. doi: 10.1038/ncomms13405.

[170] Jan Vogelsang, Nahid Talebi, Germann Hergert, Andreas Wöste, Petra Groß, Achim Hartschuh, and Christoph Lienau. Plasmonic-Nanofocusing-Based Electron Holography. *ACS Photonics*, 5(9):3584–3593, 2018. doi: 10.1021/acsphotonics.8b00418.

[171] Jan Vogelsang, Germann Hergert, Dong Wang, Petra Groß, and Christoph Lienau. Observing charge separation in nanoantennas via ultrafast point-projection electron microscopy. *Light: Science & Applications*, 7(1):55, 2018. doi: 10.1038/s41377-018-0054-5.

[172] Michael Krüger, Christoph Lemell, Georg Wachter, Joachim Burgdörfer, and Peter Hommelhoff. Attosecond physics phenomena at nanometric tips. *Journal of Physics B: Atomic, Molecular and Optical Physics*, 51 (17):172001, 2018. doi: 10.1088/1361-6455/aac6ac.

[173] Nora Bach, Till Domröse, Armin Feist, Thomas Rittmann, Stefanie Strauch, Claus Ropers, and Sascha Schäfer. Coulomb interactions in high-coherence femtosecond electron pulses from tip emitters. *Structural Dynamics*, 6(1):014301, 2019. doi: 10.1063/1.5066093.

[174] Martin Esmann, Simon F. Becker, Bernard B da Cunha, Jens H. Brauer, Ralf Vogelgesang, Petra Groß, and Christoph Lienau. k-space imaging of the eigenmodes of sharp gold tapers for scanning near-field optical microscopy. *Beilstein Journal of Nanotechnology*, 4(1):603–610, 2013. doi: 10.3762/bjnano.4.67.

[175] Armin Feist, Katharina E. Echternkamp, Jakob Schauss, Sergey V. Yalunin, Sascha Schäfer, and Claus Ropers. Quantum coherent optical phase modulation in an ultrafast transmission electron microscope. *Nature*, 521(7551):200–203, 2015. doi: 10.1038/nature14463.

[176] Nahid Talebi, Wilfried Sigle, Ralf Vogelgesang, Martin Esmann, Simon F. Becker, Christoph Lienau, and Peter A. van Aken. Excitation of Mesoscopic Plasmonic Tapers by Relativistic Electrons: Phase Matching versus Eigenmode Resonances. *ACS Nano*, 9(7):7641–7648, 2015. doi: 10.1021/acsnano.5b03024.

[177] Sergey V. Yalunin, Benjamin Schröder, and Claus Ropers. Theory of electron energy loss near plasmonic wires, nanorods, and cones. *Physical Review B*, 93(11):115408, 2016. doi: 10.1103/PhysRevB.93.115408.

[178] Fanfan Lu, Wending Zhang, Ligang Huang, Shuhai Liang, Dong Mao, Feng Gao, Ting Mei, and Jianlin Zhao. Mode evolution and nanofocusing of grating-coupled surface plasmon polaritons on metallic tip. *Opto-Electronic Advances*, 1(6):18001001–18001007, 2018. doi: 10.29026/oea.2018.180010.

[179] Mark I. Stockman, Katrin Kneipp, Sergey I. Bozhevolnyi, Soham Saha, Aveek Dutta, Justus Ndukaife, Nathaniel Kinsey, Harsha Reddy, Urcan Guler, Vladimir M. Shalaev, Alexandra Boltasseva, Behrad Gholipour, Harish N. S. Krishnamoorthy, Kevin F. MacDonald, Cesare Soci, Nikolay I. Zheludev, Vassili Savinov, Ranjan Singh, Petra Groß, Christoph Lienau, Michal Vadai, Michelle L. Solomon, David R. Barton, Mark Lawrence, Jennifer A. Dionne, Svetlana V. Boriskina, Ruben Esteban, Javier Aizpurua, Xiang Zhang, Sui Yang, Danqing Wang, Weijia Wang, Teri W. Odom, Nicolò Accanto, Pablo M. de Roque, Ion M. Hancu, Lukasz Piatkowski, Niek F. van Hulst, and Matthias F. Kling. Roadmap on plasmonics. *Journal of Optics*, 20(4):043001, 2018. doi: 10.1088/2040-8986/aaa114.

[180] Michael W. Vogel. Optimization of plasmon nano-focusing in tapered metal rods. *Journal of Nanophotonics*, 2(1):021852, 2008. doi: 10.1117/1.3046689.

[181] Sebastian Thomas, Georg Wachter, Christoph Lemell, Joachim Burgdörfer, and Peter Hommelhoff. Large optical field enhancement for nanotips with large opening angles. *New Journal of Physics*, 17(6):063010, 2015. doi: 10.1088/1367-2630/17/6/063010.

[182] S. Grésillon, L. Aigouy, A. C. Boccara, J. C. Rivoal, X. Quelin, C. Desmarest, P. Gadenne, V. A. Shubin, A. K. Sarychev, and V. M. Shalaev.

Experimental observation of localized optical excitations in random metal-dielectric films. *Physical Review Letters*, 82(22):4520–4523, 1999. doi: 10.1103/PhysRevLett.82.4520.

[183] P. G. Etchegoin, E. C. Le Ru, and M. Meyer. Erratum: "An analytic model for the optical properties of gold" [J. Chem. Phys. 125, 164705 (2006)]. *The Journal of Chemical Physics*, 127(18):189901, 2007. doi: 10.1063/1.2802403.

[184] Florian Huth, Andrey Chuvilin, Martin Schnell, Iban Amenabar, Roman Krutokhvostov, Sergei Lopatin, and Rainer Hillenbrand. Resonant antenna probes for tip-enhanced infrared near-field microscopy. *Nano Letters*, 13(3):1065–1072, 2013. doi: 10.1021/nl304289g.

[185] Mikhail A. Lyalinov. Electromagnetic scattering by a circular impedance cone: diffraction coefficients and surface waves. *IMA Journal of Applied Mathematics*, 79(3):393–430, 2014. doi: 10.1093/imamat/hxs072.

[186] Kazuyoshi Kurihara, Akira Otomo, Atsushi Syouji, Junichi Takahara, Koji Suzuki, and Shiyoshi Yokoyama. Superfocusing modes of surface plasmon polaritons in conical geometry based on the quasi-separation of variables approach. *Journal of Physics A: Mathematical and Theoretical*, 40(41):12479–12503, 2007. doi: 10.1088/1751-8113/40/41/015.

[187] S. T. Chui, Xinzhong Chen, Mengkun Liu, Zhifang Lin, and Jian Zi. Scattering of electromagnetic waves from a cone with conformal mapping: Application to scanning near-field optical microscope. *Physical Review B*, 97(8):081406, 2018. doi: 10.1103/PhysRevB.97.081406.

[188] J. C. Ashley and L. C. Emerson. Dispersion relations for non-radiative surface plasmons on cylinders. *Surface Science*, 41(2):615–618, 1974. doi: 10.1016/0039-6028(74)90080-6.

[189] C. A. Pfeiffer, E. N. Economou, and K. L. Ngai. Surface polaritons in a circularly cylindrical interface: Surface plasmons. *Physical Review B*, 10 (8):3038–3051, 1974. doi: 10.1103/PhysRevB.10.3038.

[190] L. Novotny and C. Hafner. Light propagation in a cylindrical waveguide with a complex, metallic, dielectric function. *Physical Review E*, 50(5): 4094–4106, 1994. doi: 10.1103/PhysRevE.50.4094.

[191] B. Prade and J. Y. Vinet. Guided Optical Waves in Fibers With Negative Dielectric Constant. *Journal of Lightwave Technology*, 12(1):6–18, 1994. doi: 10.1109/50.265728.

[192] Nader A. Issa and Reinhard Guckenberger. Optical nanofocusing on tapered metallic waveguides. *Plasmonics*, 2(1):31–37, 2007. doi: 10.1007/s11468-006-9022-7.

[193] Nahid Talebi, Wilfried Sigle, Ralf Vogelgesang, and Peter van Aken. Numerical simulations of interference effects in photon-assisted electron energy-loss spectroscopy. *New Journal of Physics*, 15(5):053013, 2013. doi: 10.1088/1367-2630/15/5/053013.

[194] Min Seok Jang and Harry Atwater. Plasmonic rainbow trapping structures for light localization and spectrum splitting. *Physical Review Letters*, 107 (20):1–5, 2011. doi: 10.1103/PhysRevLett.107.207401.

[195] Sánchez J. Erik, Lukas Novotny, and X. Sunney Xie. Near-field fluorescence microscopy based on two-photon excitation with metal tips. *Physical*

Review Letters, 82(20):4014–4017, 1999. doi: 10.1103/PhysRevLett.82.4014.

[196] Björn Piglosiewicz, Slawa Schmidt, Doo Jae Park, Jan Vogelsang, Petra Groß, Cristian Manzoni, Paolo Farinello, Giulio Cerullo, and Christoph Lienau. Carrier-envelope phase effects on the strong-field photoemission of electrons from metallic nanostructures. *Nature Photonics*, 8(1):37–42, 2014. doi: 10.1038/nphoton.2013.288.

[197] Axel G. Griesbeck and Uwe J. Meierhenrich. Asymmetric Photochemistry and Photochirogenesis. *Angewandte Chemie International Edition*, 41 (17):3147–3154, 2002. doi: 10.1002/1521-3773(20020902)41:17<3147::AID-ANIE3147>3.0.CO;2-V.

[198] Uwe Meierhenrich. *Amino Acids and the Asymmetry of Life Advances in Astrobiology and Biogeophysics*. Springer Berlin Heidelberg, 2008.

[199] Ventsislav K. Valev, Jeremy J. Baumberg, Concita Sibilia, and Thierry Verbiest. Chirality and Chiroptical Effects in Plasmonic Nanostructures: Fundamentals, Recent Progress, and Outlook. *Advanced Materials*, 25 (18):2517–2534, 2013. doi: 10.1002/adma.201205178.

[200] Martin Schäferling, Daniel Dregely, Mario Hentschel, and Harald Giessen. Tailoring Enhanced Optical Chirality: Design Principles for Chiral Plasmonic Nanostructures. *Physical Review X*, 2(3):031010, 2012. doi: 10.1103/PhysRevX.2.031010.

[201] Mario Hentschel, Martin Schäferling, Xiaoyang Duan, Harald Giessen, and Na Liu. Chiral plasmonics. *Science Advances*, 3(5):1–13, 2017. doi: 10.1126/sciadv.1602735.

[202] Bettina Frank, Xinghui Yin, Martin Schäferling, Jun Zhao, Sven M. Hein, Paul V. Braun, and Harald Giessen. Large-Area 3D Chiral Plasmonic Structures. *ACS Nano*, 7(7):6321–6329, 2013. doi: 10.1021/nn402370x.

[203] Mengjia Wang, Zhijin Huang, Roland Salut, Miguel Angel Suarez, Huihui Lu, Nicolas Martin, and Thierry Grosjean. Plasmonic Helical Nanoantenna As a Converter between Longitudinal Fields and Circularly Polarized Waves. *Nano Letters*, 21(8):3410–3417, 2021. doi: 10.1021/acs.nanolett.0c04948.

[204] Anton Kuzyk, Robert Schreiber, Zhiyuan Fan, Günther Pardatscher, Eva-Maria Roller, Alexander Högele, Friedrich C. Simmel, Alexander O. Govorov, and Tim Liedl. DNA-based self-assembly of chiral plasmonic nanostructures with tailored optical response. *Nature*, 483(7389):311–314, 2012. doi: 10.1038/nature10889.

[205] Hye-Eun Lee, Hyo-Yong Ahn, Jungho Mun, Yoon Young Lee, Minkyung Kim, Nam Heon Cho, Kiseok Chang, Wook Sung Kim, Junsuk Rho, and Ki Tae Nam. Amino-acid- and peptide-directed synthesis of chiral plasmonic gold nanoparticles. *Nature*, 556(7701):360–365, 2018. doi: 10.1038/s41586-018-0034-1.

[206] Nicholas A. Kotov, Luis M. Liz-Marzán, and Qiangbin Wang. Chiral nanomaterials: evolving rapidly from concepts to applications. *Materials Advances*, 3(9):3677–3679, 2022. doi: 10.1039/D2MA90034C.

[207] Wei Ma, Liguang Xu, André F. de Moura, Xiaoling Wu, Hua Kuang, Chuanlai Xu, and Nicholas A. Kotov. Chiral Inorganic Nanostructures. *Chemical Reviews*, 117(12):8041–8093, 2017. doi: 10.1021/acs.chemrev.6b00755.

[208] Kyle W. Smith, Stephan Link, and Wei-Shun Chang. Optical characterization of chiral plasmonic nanostructures. *Journal of Photochemistry and Photobiology C: Photochemistry Reviews*, 32:40–57, 2017. doi: 10.1016/j.jphotochemrev.2017.05.004.

[209] Justyna K. Gansel, Michael Thiel, Michael S. Rill, Manuel Decker, Klaus Bade, Volker Saile, Georg Von Freymann, Stefan Linden, and Martin Wegener. Gold helix photonic metamaterial as broadband circular polarizer. *Science*, 325(5947):1513–1515, 2009. doi: 10.1126/science.1177031.

[210] Justyna K. Gansel, Michael Latzel, Andreas Frölich, Johannes Kaschke, Michael Thiel, and Martin Wegener. Tapered gold-helix metamaterials as improved circular polarizers. *Applied Physics Letters*, 100(10), 2012. doi: 10.1063/1.3693181.

[211] Johannes Sachs, Jan Philipp Günther, Andrew G. Mark, and Peer Fischer. Chiroptical spectroscopy of a freely diffusing single nanoparticle. *Nature Communications*, 11(1):1–7, 2020. doi: 10.1038/s41467-020-18166-5.

[212] Eitam Vinegrad, Daniel Vestler, Assaf Ben-Moshe, A. Ronny Barnea, Gil Markovich, and Ori Cheshnovsky. Circular Dichroism of Single Particles. *ACS Photonics*, 5(6):2151–2159, 2018. doi: 10.1021/acsphotonics.8b00016.

[213] R. F. Egerton. Electron energy-loss spectroscopy in the TEM. *Reports on Progress in Physics*, 72(1):016502, 2009. doi: 10.1088/0034-4885/72/1/016502.

[214] A. Asenjo-Garcia and F. J. García de Abajo. Dichroism in the Interaction between Vortex Electron Beams, Plasmons, and Molecules. *Physical*

Review Letters, 113(6):066102, 2014. doi: 10.1103/PhysRevLett.113.066102.

[215] Tyler R. Harvey, Jan Wilke Henke, Ofer Kfir, Hugo Lourenço-Martins, Armin Feist, F. Javier García De Abajo, and Claus Ropers. Probing Chirality with Inelastic Electron-Light Scattering. *Nano Letters*, 20(6): 4377–4383, 2020. doi: 10.1021/acs.nanolett.0c01130.

[216] Taeko Matsukata, F. Javier García de Abajo, and Takumi Sannomiya. Chiral Light Emission from a Sphere Revealed by Nanoscale Relative-Phase Mapping. *ACS Nano*, 15(2):2219–2228, 2021. doi: 10.1021/acsnano.0c05624.

[217] Pratik Chaturvedi, Keng H. Hsu, Anil Kumar, Kin Hung Fung, James C. Mabon, and Nicholas X. Fang. Imaging of Plasmonic Modes of Silver Nanoparticles Using High-Resolution Cathodoluminescence Spectroscopy. *ACS Nano*, 3(10):2965–2974, 2009. doi: 10.1021/nn900571z.

[218] Yurui Fang, Ruggero Verre, Lei Shao, Peter Nordlander, and Mikael Käll. Hot Electron Generation and Cathodoluminescence Nanoscopy of Chiral Split Ring Resonators. *Nano Letters*, 16(8):5183–5190, 2016. doi: 10.1021/acs.nanolett.6b02154.

[219] Tianyang Han, Shuai Zu, Ziwei Li, Meiling Jiang, Xing Zhu, and Zheyu Fang. Reveal and Control of Chiral Cathodoluminescence at Subnanoscale. *Nano Letters*, 18(1):567–572, 2018. doi: 10.1021/acs.nanolett.7b04705.

[220] Zhiyuan Fan and Alexander O. Govorov. Chiral Nanocrystals: Plasmonic Spectra and Circular Dichroism. *Nano Letters*, 12(6):3283–3289, 2012. doi: 10.1021/nl3013715.

[221] Z.-Y. Zhang and Y.-P. Zhao. Optical properties of helical and multiring Ag nanostructures: The effect of pitch height. *Journal of Applied Physics*, 104(1):013517, 2008. doi: 10.1063/1.2953190.

[222] Kenan Elibol and Peter A. van Aken. Hybrid Graphene-Supported Aluminum Plasmonics. *ACS Nano*, 16(8):11931–11943, 2022. doi: 10.1021/acsnano.2c01730.

[223] Katja Höflich, Thorsten Feichtner, Enno Hansjürgen, Caspar Haverkamp, Heiko Kollmann, Christoph Lienau, and Martin Silies. Resonant behavior of a single plasmonic helix. *Optica*, 6(9):1098, 2019. doi: 10.1364/OPTICA.6.001098.

[224] S. Link and M. A. El-Sayed. Simulation of the Optical Absorption Spectra of Gold Nanorods as a Function of Their Aspect Ratio and the Effect of the Medium Dielectric Constant. *The Journal of Physical Chemistry B*, 109(20):10531–10532, 2005. doi: 10.1021/jp058091f.

[225] Garnett W. Bryant, F. Javier García de Abajo, and Javier Aizpurua. Mapping the Plasmon Resonances of Metallic Nanoantennas. *Nano Letters*, 8(2):631–636, 2008. doi: 10.1021/nl073042v.

[226] Moussa N'Gom, Shuzhou Li, George Schatz, Rolf Erni, Ashish Agarwal, Nicholas Kotov, and Theodore B. Norris. Electron-beam mapping of plasmon resonances in electromagnetically interacting gold nanorods. *Physical Review B*, 80(11):113411, 2009. doi: 10.1103/PhysRevB.80.113411.

[227] Abrin L Schmucker, Nadine Harris, Matthew J Banholzer, Martin G Blaber, Kyle D Osberg, George C Schatz, and Chad A Mirkin. Correlating Nanorod Structure with Experimentally Measured and Theoretically

Predicted Surface Plasmon Resonance. *ACS Nano*, 4(9):5453–5463, 2010. doi: 10.1021/nn101493t.

[228] Vincenzo Amendola, Roberto Pilot, Marco Frasconi, Onofrio M. Maragò, and Maria Antonia Iatì. Surface plasmon resonance in gold nanoparticles: a review. *Journal of Physics: Condensed Matter*, 29(20):203002, 2017. doi: 10.1088/1361-648X/aa60f3.

[229] Yi Yu Cai, Jun G. Liu, Lawrence J. Tauzin, Da Huang, Eric Sung, Hui Zhang, Anneli Joplin, Wei Shun Chang, Peter Nordlander, and Stephan Link. Photoluminescence of Gold Nanorods: Purcell Effect Enhanced Emission from Hot Carriers. *ACS Nano*, 12(2):976–985, 2018. doi: 10.1021/acsnano.7b07402.

[230] Mathias Kobylko, Pierre-Eugène Coulon, Abdallah Slablab, Alexandre Fafin, Julien Cardin, Christian Dufour, Arthur Losquin, Mathieu Kociak, Isabelle Monnet, Dominique Mailly, Xavier Lafosse, Christian Ulysse, Enric Garcia-Caurel, and Giancarlo Rizza. Localized Plasmonic Resonances of Prolate Nanoparticles in a Symmetric Environment: Experimental Verification of the Accuracy of Numerical and Analytical Models. *Physical Review Applied*, 9(6):064038, 2018. doi: 10.1103/PhysRevApplied.9.064038.

[231] José M. Caridad, David McCloskey, Francesco Rossella, Vittorio Bellani, John F. Donegan, and Vojislav Krstić. Effective Wavelength Scaling of and Damping in Plasmonic Helical Antennae. *ACS Photonics*, 2(6): 675–679, 2015. doi: 10.1021/acsphotonics.5b00076.

[232] Aycan Yurtsever, Renske M. van der Veen, and Ahmed H. Zewail. Subparticle Ultrafast Spectrum Imaging in 4D Electron Microscopy. *Science*, 335(6064):59–64, 2012. doi: 10.1126/science.1213504.

[233] M. Merano, S. Sonderegger, A. Crottini, S. Collin, P. Renucci, E. Pelucchi, A. Malko, M. H. Baier, E. Kapon, B. Deveaud, and J.-D. Ganière. Probing carrier dynamics in nanostructures by picosecond cathodoluminescence. *Nature*, 438(7067):479–482, 2005. doi: 10.1038/nature04298.

[234] Georg Haberfehlner, Franz-Philipp Schmidt, Gernot Schaffernak, Anton Hörl, Andreas Trügler, Andreas Hohenau, Ferdinand Hofer, Joachim R. Krenn, Ulrich Hohenester, and Gerald Kothleitner. 3D Imaging of Gap Plasmons in Vertically Coupled Nanoparticles by EELS Tomography. *Nano Letters*, 17(11):6773–6777, 2017. doi: 10.1021/acs.nanolett.7b02979.